

Investigating the Water-Titanium Dioxide Interface using Sum Frequency Generation Spectroscopy



JOHANNES GUTENBERG
UNIVERSITÄT MAINZ

Simon Johannes Schlegel

geb. Schmitt

Max-Planck-Institut für Polymerforschung

Dissertation zur Erlangung des Grades eines

„**Doctor rerum naturalium (Dr. rer. nat.)**“

des Fachbereiches 09 - Chemie, Pharmazie, Geographie und
Geowissenschaften der

Johannes Gutenberg-Universität Mainz

Mainz, Februar 2020

1. Gutachter:
2. Gutachter:

Statutory Declaration

I hereby declare that I wrote this dissertation submitted without any unauthorized external assistance and used only sources acknowledged in the work. All textual passages which are appropriated verbatim or paraphrased from published and unpublished texts as well as all information obtained from oral sources are duly indicated and listed in accordance with bibliographical rules. In carrying out this research, I complied with the rules of standard scientific practice as formulated in the statutes of the Johannes Gutenberg-University Mainz to insure standard scientific practice.

Simon Schlegel

Für Heiner.

„Es gibt eine grundlegende und sehr wertvolle Aussage in der Wissenschaft. Sie ist ein Zeichen von Weisheit und lautet: ‚Ich weiß es nicht!‘.“

- *Lieutenant Commander Data*

Abstract

In order to fight global warming, clean and cheap alternatives to fossil fuels are needed. A promising candidate is hydrogen, which can be obtained by photocatalytic splitting of water utilizing sunlight and titanium dioxide as photocatalyst. To make this process profitable, its fundamentals need to be understood. The research presented in this work aims at a better understanding of the structure of the water-TiO₂-interface, using the surface sensitive Sum-Frequency-Generation (SFG) spectroscopy technique.

The first experimental part of this work demonstrates the potency of SFG. It is used as a complementary technique to learn more about the behaviour of the surfactant CTAB on the water-air-interface in the presence of high amounts of dissolved NaCl.

One part of this work was the deposition of TiO₂-thin films on CaF₂-windows using the magnetron-RF-sputter technique. The target was to produce samples for measurements at the TiO₂-D₂O-interface. The main problems of this task are presented and it is shown why no reproducible results could be obtained.

The first main part of this thesis describes SFG experiments on the TiO₂-D₂O-interface using solutions of pD 3, 5, 7, 9 and 11. The SFG-signal shows three peaks for all pD values. The high-frequency peak originates from weakly hydrogen-bonded interfacial Ti-OD groups that are pointing away from the TiO₂. The low-frequency peak is caused by D₂O molecules pointing towards the semiconductor, forming strong donating hydrogen-bonds with the aforementioned Ti-OD groups. The central-frequency peak originates from D₂O molecules in the second water layer. When the solution pD is below 5 (point of zero charge (pzc) of TiO₂), the water molecules point away from the TiO₂ due to a positive charge caused by protonation of the surface. At pD 5, the over all intensity of the SFG-spectra decreases, indicating that the orientation of the water molecules is random. With rising pD value, the intensity increases, caused by deprotonation of the surface, which results in a negative charge. At higher pD, the water molecules in the second layer are oriented with their deuterium atoms pointing towards the semiconductors surface. Additional measurements at pD 2 showed a coupling effect between the low and the central frequency peaks. This is not the case for pD 11.

In the second main part of this work, femtosecond time-resolved SFG-experiments are presented, conducted on the TiO₂-D₂O-interface with solutions of pD 3, 7 and 11. Using pump frequencies of 2550 and 2400 cm^{-1} , it was found that with increasing pD-value the lifetime of the excited state decreases, probably caused by the stronger hydrogen-bonding network for high pD-values. It is also shown that for the 2550 cm^{-1} pump the coupling from the direct to the cross peak is dominated by a down-hill energy transfer, whereas the coupling for the 2400 cm^{-1} pump includes an instantaneous frequency shift of the cross peak. Additionally, experiments using isotopically diluted solutions of pD 3, 7 and 11 showed, that for all three pD-values the relaxation time strongly increases, due to the suppression of coupling effects in the hydrogen-bonding network. For pD 11 this finding stands in contrast to results of the static SFG-experiments conducted before. This hints to an unknown coupling mechanism between the water molecules and the semiconductor.

Abstract

Zur Bekämpfung des Klimawandels sind saubere sowie günstige Alternativen zu fossilen Brennstoffen notwendig. Ein vielversprechender Kandidat ist Wasserstoff, welcher durch photokatalytische Spaltung aus Wasser mittels Sonnenlicht und Titandioxid als Photokatalysator gewonnen werden kann. Um diesen Prozess rentabel nutzbar machen zu können ist vertieftes Wissen über den Mechanismus unabdingbar. Diese Arbeit zielt darauf ab ein besseres Verständnis der Struktur der Wasser-TiO₂-Grenzfläche, unter Verwendung der grenzflächensensitiven Summenfrequenzspektroskopie (SFG), zu erreichen. Der erste Experimententeil zeigt das Potenzial von SFG auf. Die Methode wird ergänzend zur Untersuchung des Verhaltens des Tensids CTAB an der Wasser-Luft-Grenzfläche im Beisein hoher Konzentrationen an NaCl verwendet.

Ein weiterer Teil dieser Arbeit ist die Deposition von TiO₂-Dünnschichten auf CaF₂-Fenstern unter Verwendung der Magnetron-RF-Sputter-Technik. Ziel war die Herstellung von Proben für die Untersuchung der TiO₂-D₂O-Grenzfläche. Dabei wird hier auf die Probleme der verwendeten Methode eingegangen und aufgezeigt, weshalb keine reproduzierbaren Ergebnisse erhalten wurden.

Den ersten Hauptteil dieser Arbeit stellen SFG-Messungen der TiO₂-D₂O-Grenzfläche mit Lösungen von pD 3, 5, 7, 9 und 11 dar. Das SFG-Spektrum zeigt für alle pD-Werte drei Signale. Das hochfrequente Signal wird durch schwach wasserstoffverbrückte, der Grenzfläche abgewandte Ti-OD-Gruppen generiert. Das niederfrequente Signal rührt von D₂O-Molekülen, welche der Grenzfläche zugewandt sind und starke donierende Wasserstoffbrücken mit den erwähnten Ti-OD-Gruppen bilden. Das zentrale Signal kommt von D₂O-Molekülen der zweiten Wasserschicht. Liegt der pD unter 5 (Ladungsnullpunkt von TiO₂), zeigen die Moleküle wegen der positiv geladenen, protonierten Oberfläche vom TiO₂ weg. Bei pD 5 sinkt die Intensität des SFG-Spektrums, was auf eine chaotischere Orientierung des Wassers deutet. Mit steigendem pD steigt die Intensität. Bei höheren pD-Werten wird das TiO₂ deprotoniert, was zu einer negativen Ladung führt. Dabei orientiert sich das Wasser der zweiten Schicht mit den Deuteriumatomen in Richtung Halbleiter. Ebenso konnte gezeigt werden, dass für pD 2 Kupplungseffekte zwischen dem niederfrequenten und dem zentralen Signal auftreten. Für pD 11 ist dies nicht der Fall. Im zweiten Hauptteil dieser Arbeit werden zeitaufgelöste SFG-Experimente, durchgeführt an der TiO₂-D₂O-Grenzfläche mit Lösungen von pD 3, 7 und 11, präsentiert. Verwendet wurden Pumpfrequenzen von 2550 und 2400 cm^{-1} , wobei eine sinkende Lebensdauer des angeregten Zustands mit steigendem pD-Wert beobachtet wurde. Dies ist vermutlich ein Resultat des stärkeren Wasserstoffbrückennetzwerks bei hohen pD-Werten. Ebenso wird gezeigt, dass beim 2550 cm^{-1} Pumpimpuls die Kopplung zwischen direktem und Kreuzsignal von einem bergab Energietransfer dominiert wird, wohingegen beim 2400 cm^{-1} Pumpimpuls eine instantane Frequenzverschiebung im Kreuzsignal beobachtet wird. Zusätzliche Isotopenverdünnungsexperimente bei pD 3, 7 und 11 zeigten eine Zunahme der Relaxationszeit für alle pD-Werte durch die Unterdrückung von Kupplungseffekten im Wasserstoffbrückennetzwerk. Für pD 11 steht dies im Gegensatz zu Ergebnissen aus den zuvor durchgeführten statischen SFG-Experimenten. Dieser Umstand weist auf einen bisher unbekanntem Kupplungsmechanismus zwischen Wasser und dem Halbleiter hin.

Contents

1	Introduction	1
1.1	Titanium Dioxide	2
1.1.1	General Properties	2
1.1.2	Crystal and Surface Structures	3
1.1.3	Surface Chemistry	5
1.2	Photocatalytic Splitting of Water	7
1.3	Water and Heavy Water	9
1.4	Hydrogen-Bonding	10
1.5	Outline	11
2	Sum-Frequency-Generation Spectroscopy	13
2.1	General Concept	13
2.2	Theory	15
2.2.1	The non-linear Light-Matter-Interaction	15
2.2.2	The E-Fields Polarisation	17
2.2.3	The Generated SF-Response	20
2.2.4	How the Signal Depends on the IR-Wavelength: The Lorentzian-Model	21
2.3	Time-Resolved Pump-Probe-SFG-Spectroscopy	22
2.4	The SFG-Setup	25
3	Influence of Salt on the CMC and Dynamics of CTAB-Solutions	27
3.1	Definition and Properties of Surfactants	27
3.2	Surface Tension and Dynamics of CTAB Solutions and the Influence of Salt	30
3.3	SFG on the Water-CTAB-NaCl System	34
4	Deposition of TiO₂ Thin Films using RF-Magnetron-Sputtering	43
4.1	The Sputtering Process	43
4.2	Sputtering Results	46
4.3	Discussion of Possible Sources of Error	50
5	pD-Dependent Water Structure at the Water-Titanium Dioxide Interface	51
5.1	Introduction	51
5.2	Experimental Section	53
5.2.1	Sample	53
5.2.2	SFG Experiments	54

5.3	Results and Discussion	56
6	Dynamics of the D₂O-TiO₂-Interface	67
6.1	Introduction	67
6.2	Time-Resolved SFG-Spectra of the TiO ₂ -D ₂ O-Interface	72
6.2.1	Pump-Frequency of 2550 cm ⁻¹	72
6.2.2	Pump-Frequency of 2400 cm ⁻¹	81
6.3	Time Resolved SFG-spectra of the TiO ₂ -D ₂ O-Interface using Isotopically Diluted D ₂ O-Solutions	85
6.4	Conclusion	89
7	Conclusion and Outlook	93
7.1	CTAB at the Water-Air-Interface	93
7.2	Sputter Deposition of TiO ₂ on CaF ₂	95
7.3	pD-Dependent Water Structure at the D ₂ O-TiO ₂ -Interface	96
7.4	pD-Dependent Dynamics at the TiO ₂ -D ₂ O-Interface	98
	List of Figures	102
	List of Tables	103
	Bibliography	105
	Appendix	115
	Acknowledgements	119

1 Introduction

In the near future earth's reserves of coal, oil and gas will either be depleted or their usage will be banned due to its effect on the global climate. Therefore mankind will need clean and preferably cheap alternatives to hold up its standard of living. Furthermore, it is desirable to decentralize the production of energy, enabling remote areas to be more independent, especially in areas with less infrastructure.

One possibility to achieve these goals is to convert sunlight into chemical energy. Nature makes use of this idea since billions of years in form of photosynthesis. Although this process is studied extensively, our capability of reproducing it in an applicable manner is highly limited due to its complexity. In 1972 however, Honda and Fujishima observed the evolution of oxygen and hydrogen when water is in contact with titanium dioxide and illuminated with UV-light [1]. The photocatalytic splitting of the highly abundant water molecule has drawn much attention of scientists around the world ever since its discovery and has been investigated extensively. Much of the performed research aims to improve the process' efficiency, be it by alternating the semiconductor material, its surface morphology or the conditions under which a future device is to be employed. Due to the lack of deeper understanding about the underlying mechanism of the reaction however, most researchers make use of a trail-and-error approach, which consumes high amounts of time and resources.

In order to learn more about the fundamental nature of the photocatalytic splitting of water, it is necessary to study the molecule's interaction with the semiconductor. To do so, a method is needed that fulfills two requirements. First, it needs to have molecular specificity for the water molecules. A technique that could satisfy this requirement is infrared (IR) spectroscopy, being sensitive for the hydrogen-bonding network of water molecules. The drawback of standard IR-spectroscopy techniques is that they probe all the water molecules present in the sample. The site where the reaction takes place, however, is the interface of water and titanium dioxide, which is very small compared to the bulk material in the system. Therefore the second requirement is the specificity only for the few layers of water closest to the semiconductor's surface.

The aim of this work is to provide deeper insights into the fundamental behaviour of water molecules in contact with titanium dioxide. To do so, interface-specific Sum-Frequency-Generation (SFG) Spectroscopy data of the OH-stretch vibration of heavy water (D_2O) molecules directly in contact with thin layers of titanium dioxide (TiO_2) will be presented. It will be demonstrated how the interaction of D_2O and TiO_2 changes depending on the protonation state of the semiconductor and how it causes the heavy water molecules to change their orientation. Additionally, data will be presented that provide insight into the time scales of the energy dissipation of heavy water molecules in contact with titanium dioxide.

In this chapter, important concepts for this thesis will be presented. Titanium dioxide is considered to be a key material in the future of energy production due to its unique capabilities. Therefore the general properties, bulk and surface structure and surface chemistry are portrayed. After that, the photocatalytic splitting mechanism will be discussed, since it is the basic driving force for this work to get insights into its fundamental mechanism. This will be followed by the properties of water itself and the nature of the hydrogen-bonding network that gives water its unique characteristics.

1.1 Titanium Dioxide

1.1.1 General Properties

Titanium dioxide is an inorganic, semiconductive material, consisting of one titanium atom and two oxygen atoms per stoichiometric unit (TiO_2) and a molar mass of $79.87 \frac{\text{g}}{\text{mol}}$. It is used worldwide as white pigment in paint and as UV-light absorber in sunscreen. It's global production lies between 4 and 5 million tons per year and is mainly achieved by the sulfate process [2]. In this process, the mineral ilmenite is dissolved in concentrated sulfuric acid and reacts to iron sulfate and titanyl sulfate.



The iron sulfate is precipitated from the solution. Afterwards, the titanyl sulfate in solution is precipitated, washed and annealed at 800-950 °C to form TiO_2 .

Titanium dioxide is cheap and chemically inert, meaning it can only be dissolved in hot sulfuric and hydrofluoric acid and hot bases [3]. It is considered to be nontoxic, though in recent years several studies have shown, that micro- and nanoparticles might have carcinogenic effects on the lungs. These seem not to be connected to the chemical properties but to the shape of the particles, which is comparable to the effect of asbestos [4].

TiO_2 exists in nature mainly in three polymorphic modifications: rutile, anatase and brookite. In 2015 a fourth, high pressure modification was found (riesit) [5]. Rutile is the most abundant and most stable modification of TiO_2 . Between 600 and 800 °C anatase and brookite convert irreversibly into rutile [3]. The three modifications differ much in their properties such as crystal structure, density ($4.24 \frac{\text{g}}{\text{mL}}$ for rutile, $3.83 \frac{\text{g}}{\text{mL}}$ for anatase [6]), bandgap and refractive index [7]. The bandgap of anatase is the highest with 3.23 eV, that for rutile with 3.02 eV the lowest, while both result in the absorption of light with wavelengths in the UV range [8]. All three are birefringent, meaning that for the same crystal phase and surface termination the refractive indices for perpendicularly polarized light beams (n_o and n_e for ordinary and extraordinary) differ, leading to different refraction-angles of the two polarisations. Additionally the material is very dispersive, so the refractive index is strongly dependent on the wavelength of the incoming light [9]. Apart from its capabilities as a semiconductor the most interesting property of TiO_2 is its ability for photocatalysis, which will be explained in section 1.2. Although for this work

measurements were performed on amorphous titanium dioxide thin films for technical reasons, the next sections will focus on the manifold properties of crystalline titanium dioxide, such as bulk and surface structures and the surface chemistry. Of course, the properties of amorphous semiconductors can differ strongly from their crystalline phases. However, many studies focus on the latter systems due to the high degree of control over surface structure. Many of the different properties of various crystalline phases might be found in amorphous TiO_2 altogether.

1.1.2 Crystal and Surface Structures

Figure 1.1 shows the crystal structures of Rutile and Anatase schematically.

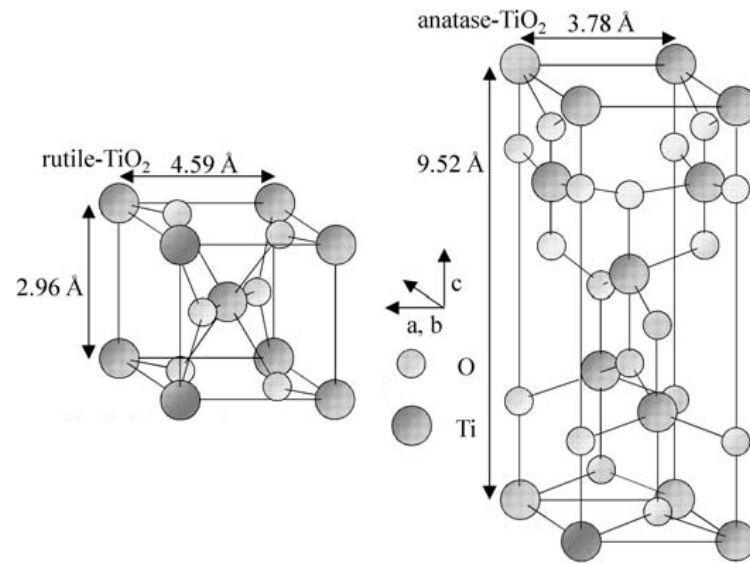


Figure 1.1: Schematic unit cells of Rutile (left) and Anatase (right). Picture modified from [10]

Rutile (left) is the eponymous for the rutile-structure, that can be found in many ionic AB_2 -crystals, such as metal oxides (MO_2) and difluorides (MF_2). This structure can be seen as the arrangement of oxygen anions (O^{2-}) in a distorted hexagonal close-packed system, with Ti^{4+} cations filling half of the octahedral voids. The titanium ions themselves are ordered in a body centered, tetragonal unit cell. In this way, TiO_2 is build up of long chains of TiO_6 -octahedrons, in which every unit shares two opposite edges with two neighbouring octahedrons. The six octahedron corners connect the chains to a three dimensional network. Every Ti^{4+} -ion is octahedrally surrounded by six O^{2-} -, and every oxygen-ion by three Ti-ions in a trigonal-planar fashion [11].

The structure of anatase and brookite (not shown) is based on a distorted cubic close-packed structure of O^{2-} -ions. Here, half the octahedral voids are filled with Ti^{4+} -ions in such a way, that every TiO_6 -octahedron shares three (brookite) or four (anatase) edges

with neighbouring octahedrons [11].

Figure 1.2 shows the arrangement of the TiO_6 -octahedrons for rutile (left) and anatase (right) schematically.

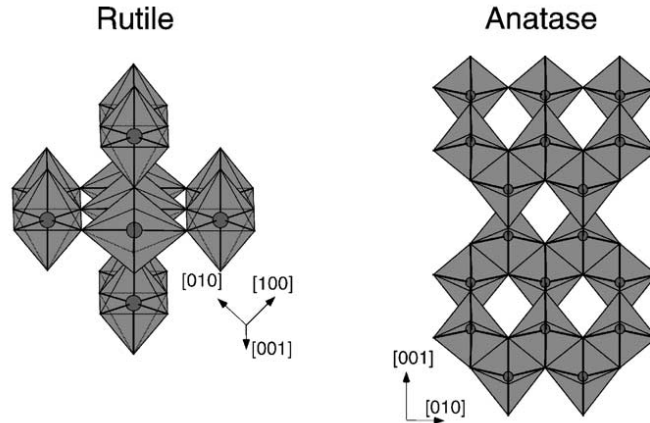


Figure 1.2: Schematic display of the long-range order of rutile and anatase. Picture modified from [6]

The surface structure of crystalline materials is determined by the bulk crystal structure, as shown before, and the direction of its interruption. The directionality of single crystals leads to many different facets, that all differ in the order of the crystal terminating atoms. Here the focus will be on the exemplary rutile (110) plane. The termination is shown in figure 1.3.

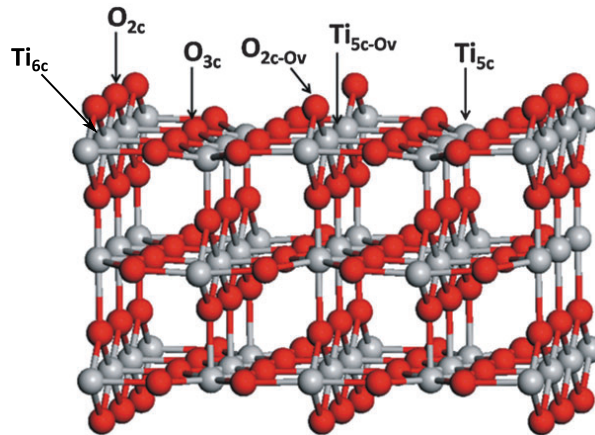


Figure 1.3: The (110) terminated plane of rutile. Picture modified from [12].

The rutile (110) surface consists of four main elements, as depicted in figure 1.3. The sixfold coordinated titanium (Ti_{6c}) and the threefold coordinated oxygen ions (O_{3c}) are the *saturated* interfacial species. Though these atoms are at the surface, they possess

the same bonds as if they were located somewhere inside the crystal. However, since the O_{3c} is exposed to the neighbouring phase, be it, air, vacuum, water, etc., it can serve as adsorption or reaction site [13]. The twofold coordinated, bridging oxygen ions (O_{2c} , sometimes O_b) are the outer most border of the surface and are exposed towards the neighbouring phase in isolated rows. As explained before, in rutile every oxygen atom is in contact with three Ti-ions. Therefore the O_{2c} ions at the surface are under coordinated, with one dangling bond stretching into free space. The same is true for the fivefold coordinated titanium ions (Ti_{5c}), which are slightly below the O_{3c} , but also possess a dangling bond and are exposed [6]. These two under-coordinated species are very probable sites for adsorption and dissociation of molecules and for reactions, as will be explained later.

Additional to these logically occurring species at the rutile (110) surface, different defect sites can play a role. Figure 1.3 shows the two, fivefold coordinated oxygen vacancy titanium ions (Ti_{5c-Ov}), which are in the same line as the Ti_{6c} . Here, a bridging oxygen ion is missing. The neighbouring oxygen ions with the twofold coordinated oxygen vacancy (O_{2c-Ov}) are coordinated to the Ti_{5c-Ov} . These, and many more possible defect sites are important for all kinds of surface reactions and are under considerable investigation [12].

1.1.3 Surface Chemistry

As most semiconducting materials, TiO_2 has a very rich surface chemistry, that stretches from simple adsorption and dissociation of atoms and molecules [14], to highly complex photocatalytic decompositions of less simple substances [15]. In fact, TiO_2 surfaces rarely are as clean as could be concluded from figure 1.3, but attract molecules and are altered by them. Especially water is generally present at the semiconductors surface due to its abundance in air and its high reactivity on the terminated crystal. This can lead to the presence of hydrogen atoms at the surface, even under UHV and high temperature, as is shown in figure 1.4.

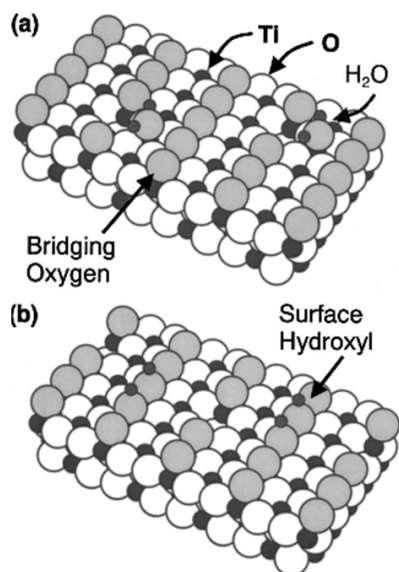
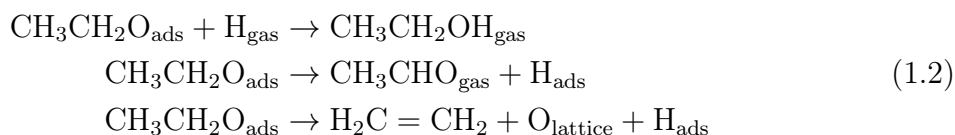


Figure 1.4: Schematic dissociation of water molecules at a defective rutile (110) surface. **a)** Adsorption of water molecules at a $Ti_{5c}-O_v$. **b)** Filled oxygen vacancy with two resulting hydroxyl groups. Picture modified from [16]

The details of the chemistry are determined by the specific surface termination. For example, on the rutile (110) surface, experiments have shown, that water adsorbs molecularly and only dissociates at defect sites [17], while it can react with the perfect (100) surface [18].

The surface chemistry of lower alcohols on titanium dioxide is mainly determined by the organic hydroxyl group [19]. For the rutile (110) surface, it was found that methanol adsorbs as a full monolayer up to 150 K. At higher temperatures, dimers are formed, covering 2/3 of the surface, which then dissociate back into the monomers at around 250 K, and subsequently desorb from the surface at 350 K [20]. At other surface terminations, the molecule adsorbs dissociatively. One reason for the differences is, that there are various types of vacancies possible [21].

Ethanol was discovered to have a rather interesting surface chemistry for the rutile (001) surface. It partly dissociates to the ethoxy group, resulting in a layer mixed with molecularly adsorbed ethanol, at 200 K. Ramping the temperature up to 300 K leads to the desorption of the molecular ethanol, only leaving the ethoxy groups. At higher temperatures these groups partly recombine to ethanol, and partly decompose to acetaldehyde or ethylene, according to [6, 22]:



As explained before, the surface chemistry of alcohols on TiO_2 is dominated by the interaction of the hydroxyl groups in the molecules, since the free Ti-ions are easily accessible for the free electron pairs of the alcohol oxygen. Therefore it is relatively surprising that pyridine does not attach to TiO_2 with its nitrogen forming a Lewis-Acid-Base-Pair, as could be expected, but rather flatly physisorbs with the whole ring in contact with the semiconductor. The same adsorption behaviour could be shown for benzene [23].

However, all the described surface interactions and reactions were reported for UHV conditions. In contact with macroscopic amounts of water, the surface chemistry changes dramatically. The surface is mainly hydroxylated due to the dissociative behaviour of water, as has been described before. At this point, titanium dioxide is an amphoteric material, meaning that it can be protonated or deprotonated depending on the solution pH-value. The point of zero charge for TiO_2 lies between pH 5 and 6 [24]. Now not only the interaction of the molecules and the semiconductor themselves play a role, but also the newly introduced charges alter the behaviour of substances in contact and in close proximity to the TiO_2 . Also the fact, that the solvent molecules disturb the interaction between the dissolved molecules and the titanium dioxide has to be taken into account. As mentioned before, the positive and negative charges arise from the protonation and deprotonation of the TiO_2 , respectively. The reactions most probably take place at different sites on the semiconductor surface. The protons might be bound to bridging oxygen atoms, as well as to hydroxyl groups present, forming a chemisorbed water species. The deprotonation most probably takes place at interfacial hydroxyl groups, leaving negative Ti-O^- groups [25]. More details will be given in chapter 5.

A deep understanding of the complex surface chemistry of TiO_2 under dark conditions is a crucial basis for studying the more complex field of photocatalysis that the semiconductor is capable of. Especially the photocatalytic splitting of water into oxygen and hydrogen, first shown by Honda and Fujishima in 1972 [1] has attracted much attention. This process will be explained in more detail in section 1.2.

1.2 Photocatalytic Splitting of Water

The desire to use sunlight and convert it into energy is understandable, since it is one of the cleanest energy sources possible, available almost everywhere. Life on earth uses this process since its very early stages in form of photosynthesis, where the photon energy is converted into chemical energy, by building glucose out of CO_2 and water. This "up-hill" reaction leads to a product containing higher energy than the reactants. In the case of the photocatalytic decomposition of organic molecules into CO_2 and H_2O , it is called a "down-hill" process [26]. Since hydrogen is an energy carrier, the photocatalytic splitting of water is an "up-hill" process as well, that stores the lights energy in the simple H_2 -bond [27].

In general, when a semiconductor is illuminated with light that has at least the energy of the materials band gap, a photon can be absorbed, generating an electron-hole-pair. The electrons, e^- , and holes, h^+ , generated can now migrate to the surface [28]. If the

semiconductor is in contact with water, at the interface the holes can oxidize water into oxygen (O_2) and the electrons can reduce protons into hydrogen (H_2) [1]. For this process to work the bandgap of the semiconductor has to be greater than 1.23 eV , which corresponds to light with a wavelength lower than 1008 nm [29]. Figure 1.5 shows this process schematically.

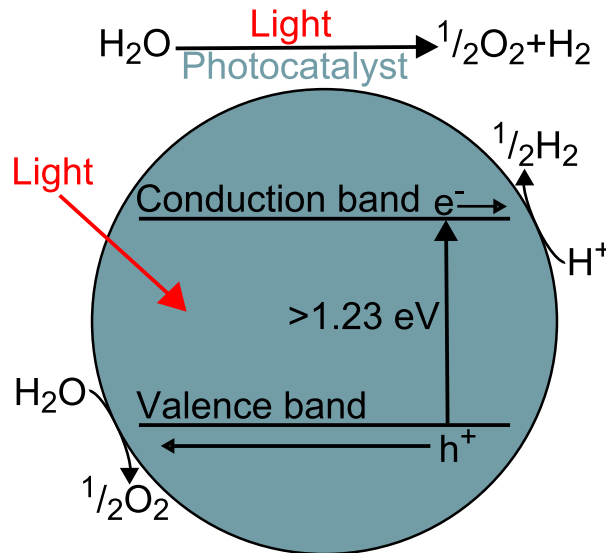


Figure 1.5: Schematics of the photocatalytic splitting of water.

For a hydrogen molecule to be formed, two electrons are needed, as are four holes for an oxygen molecule. The reaction equations for the hydrogen evolution reaction (HER) and the oxygen evolution reaction (OER) are as follows [27]:



In general for a photocatalytic reaction to work, the bandgap of a semiconductor must be at least of the same energy as for the overall electrochemical reaction required. But also the single steps are of relevance in such a way, that the potential of the conduction band must be more negative than the potential needed for the reduction step, whereas the potential of the valence band must be more positive than the required potential to oxidize a target molecule [30,31]. Also the need of high overpotentials, for example for the HER and the OER in the splitting of water, have to be considered. Therefore, the semiconductor must be chosen with care for the desired photocatalytic reaction.

In addition to these thermodynamic requirements, the photocatalytic splitting of water is controlled by kinetic limitations. For example the migration of electrons and holes towards the surfaces is dependent on the material, defect sites and doping state of the light absorbing material. If this migration is suppressed, or the charge carriers get trapped at defect sites, the recombination of electrons and holes is enhanced and therefore the

photon efficiency is reduced [32, 33].

Since the discovery of the photocatalytic splitting of water on TiO_2 , the material has been studied intensively and is generally considered to be a good model system for the process, as well as a good base material for future devices. Pure titanium dioxide has a bandgap that corresponds to the energy of light in the UV-range. This means, that most of the sunlight reaching the earth's surface cannot be used for the photocatalytic splitting of water, since its maximum lies in the visible range. Therefore, much research has been aiming at reducing the bandgap, for example by doping the material with other ions. However, this doping can influence the processes of charge carrier migration and potential, as mentioned before. Another problem is the high overpotential of the HER, which makes it necessary to excite the photocatalyst with more energy than actually needed for the water splitting process. Similar to the high bandgap of TiO_2 , this leads to a reduced spectral window of the sun's light available for the conversion of water into hydrogen and oxygen. Different approaches to overcome this obstacle have been tried, for example the loading of TiO_2 nanoparticles with islands of platinum, which has a very low overpotential and is therefore often used for the reduction of protons to H_2 [34]. In order to learn more about the fundamental mechanism of the photocatalytic splitting of water at TiO_2 , a deeper understanding of the water molecule and its properties is crucial. This will be discussed in the next section.

1.3 Water and Heavy Water

Water covers over 70 % of earth's surface, making it one of the most abundant molecules on our planet. It is the only molecule on earth existing naturally in the three physical states solid, liquid and gaseous. Water molecules build up a huge network of hydrogen-bonds causing the substance to have unique properties such as its high heat capacity, its extraordinary solvation capabilities and its density anomaly [35].

Figure 1.6 shows a free molecule of water, consisting of one oxygen atom and two hydrogen atoms. The angle H-O-H angle is 104.5° and the bond length between oxygen and hydrogen is 95.8 pm . The molar mass of water is $18.02 \frac{\text{g}}{\text{mol}}$.

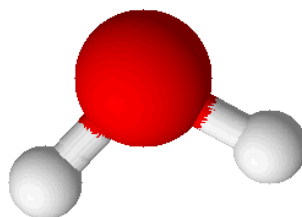


Figure 1.6: A free water molecule consisting of one oxygen and two hydrogen atoms.

Since oxygen is more electronegative than hydrogen, it is partially negatively charged, whereas the two hydrogen atoms are partially positively charged. This causes the water molecules to have a permanent dipole and therefore to be polar and to form hydrogen-bonds with each other.

Water can undergo an autoprotolytic reaction, which means one molecule can fully give

one proton to another water molecule, leaving a hydroxide anion and a hydronium cation, although the true nature of the latter is not known to the last detail. The reaction is facilitated by the strong hydrogen-bonding between the molecules and causes the pH of pure water to be 7 [3].

Heavy water consists of one oxygen atom and two deuterium atoms, which is a stable isotope of hydrogen. The additional neutrons cause the heavy water not only to have a molar mass of $20.03 \frac{g}{mol}$, but also higher melting and boiling points, as well as a higher density. Its reaction kinetics is usually slower than that of H_2O , which especially is important in biological reaction pathways. Spectroscopically the heavier deuterium atom causes the OH- and the OD-stretch vibrations to be apart about 1000 cm^{-1} (ca. $3000\text{-}3700 \text{ cm}^{-1}$ vs ca. $2000\text{-}2700 \text{ cm}^{-1}$, respectively).

As explained before, most of water's unique properties are the result of the strong hydrogen-bonding interaction between the molecules and neighbouring substances and between the molecules themselves. Therefore, section 1.4 will discuss the nature of the hydrogen-bond in more detail.

1.4 Hydrogen-Bonding

Without the formation of hydrogen-bonds, life as we know would not be possible. For example, it is the cause for the density anomaly of water. When water freezes, its molecules need more space than in the liquid case, due to the formation of a highly ordered hydrogen-bonding network. But also for the structure of our DNA and our proteins hydrogen-bonding plays an essential role.

In a hydrogen-bond the partially positively charged hydrogen (**H**) atom of one molecule (donor), covalently attached to the atom **B**, is associated with one free electron pair of the partially negatively charged **A**-atom of another molecule (acceptor) [36]. **A** is usually a strongly electronegative atom such as oxygen, nitrogen or fluorine, but other, more exotic examples are known. The underlying driving force can be explained by either the electrostatic interaction between the positive and negative partial charges of the donating and the accepting groups, or by the formation of a molecular orbital out of three atomic orbitals. In the latter theory, one (mostly sp^3 -) orbital of the **B** atom on the donor molecule, the $1s$ orbital of the hydrogen atom and one occupied orbital of the **A** atom on the acceptor molecule, combine. Together they form three molecular orbitals: one binding MO, one almost nonbinding MO and one anti-bonding MO [37]. Figure 1.7 shows this schematically.

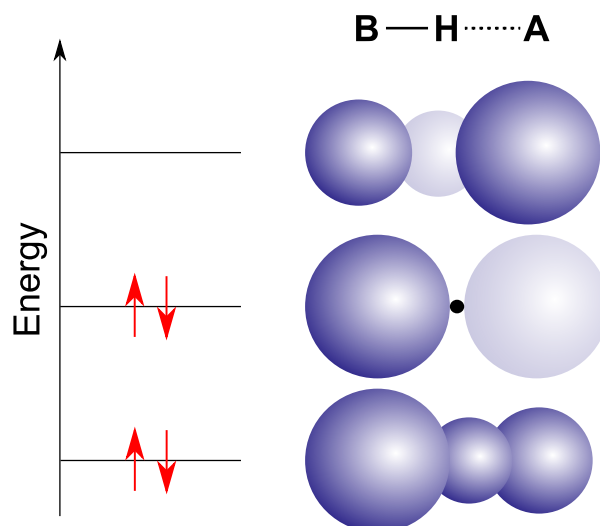


Figure 1.7: Schematic representation of the molecular orbitals formed in a hydrogen-bond. The contribution of the atomic orbital to the MO is represented by the size of the sphere. If the H-bond is bonding or not, depends on the energetic position of the “non-bonding” molecular orbital relative to the atomic orbitals.

Hydrogen-bonds are usually linear, so that the **A-H-B**-angle is between 160 and 200°. Their energy lies in the range of $20 \frac{kJ}{mol}$. In water, this interaction weakens the covalent bond between the oxygen and the hydrogen atom of the donating water molecule. In an IR spectrum this is visible by a lower frequency of the OH-stretch vibration. The hydrogen-bonding interaction is not only possible between two water molecules, but can also occur between water and another molecule that could function as a hydrogen-bond donor or acceptor.

1.5 Outline

This chapter gave a brief overview on the properties of titanium dioxide and water and the fundamentals of the photocatalytic splitting of water at the surface of the semiconductor. This knowledge is the basis for the main focus of this thesis, namely the structure and dynamic behaviour of water at the D₂O-TiO₂ interface.

The next chapter will serve as a brief introduction into the basics of sum frequency generation spectroscopy, the main tool used here for the investigation of the interface of interest. After that, in chapter 3 it will be demonstrated how powerful SFG is as a supplement for other surface specific techniques and how it can be used to learn more about the behaviour of surfactant molecules on the water-air interface for saline solutions. Chapter 4 is a report on the deposition of titanium dioxide thin films using the sputtering technique and will demonstrate the difficulties in obtaining reproducible and stable results. It will serve as the first chapter of the main work of this thesis. This in turn is introduced by chapter 5, providing deeper insights into the nature of the water structure at the D₂O-TiO₂-interface and how this structure changes with varying the semiconductors surface charge. A molecular picture of the interaction between water and the photocatalyst will

be given in the end. Subsequently, chapter 6 will show how pump-probe-SFG can give insights into the dynamics and the energy dissipation pathways of water at the TiO_2 surface. A conclusion and an outlook will be provided in chapter 7, which closes the main part and this thesis.

2 Sum-Frequency-Generation Spectroscopy

As has been explained in chapter 1, the photocatalytic splitting of water with titanium dioxide occurs solely at the interface between the liquid and the semiconductor. Compared to the huge amount of bulk H₂O and TiO₂ present in this system, this region is extremely small and therefore very difficult to access with conventional spectroscopic techniques, that are overwhelmed by the bulk signals of the materials. For this reason, a method that selectively measures the interfacial region is needed. Additionally, it is desirable to distinguish the interaction of different water molecules with different sites on the titanium dioxide surface, without disturbing signals from the semiconductor.

Sum-Frequency-Generation-Vibrational-Spectroscopy (SFG-VS, or SFG) is the ideal tool for studying interfaces, since it fulfills both criteria: specificity for the interfacial region and the OH-stretch vibration of the water molecules in this small volume. In this chapter the general concept of SFG-spectroscopy will be discussed, followed by a (superficial) mathematical derivation of the underlying theory. After that, the concept of time-resolved SFG-spectroscopy and finally a detailed description of the setup mainly used in this work will be presented.

2.1 General Concept

In this technique an infrared (IR) and a visible (VIS) laser beam are overlapped in space and time on the sample of interest. If in resonance, the IR beam can excite molecular vibrations in the system, for example OH-stretch vibrations in water. The visible beam upconverts the excited molecules into a virtual state. Subsequently, the molecules emit photons which have the sum of the frequencies of the incoming beams, which can be expressed as

$$\omega_{\text{SFG}} = \omega_{\text{VIS}} + \omega_{\text{IR}} \quad (2.1)$$

where ω_{VIS} , ω_{IR} and ω_{SFG} are the frequencies of the visible, the infrared and the resulting SFG-beams, respectively. Figure 2.1 describes the SFG-process schematically.

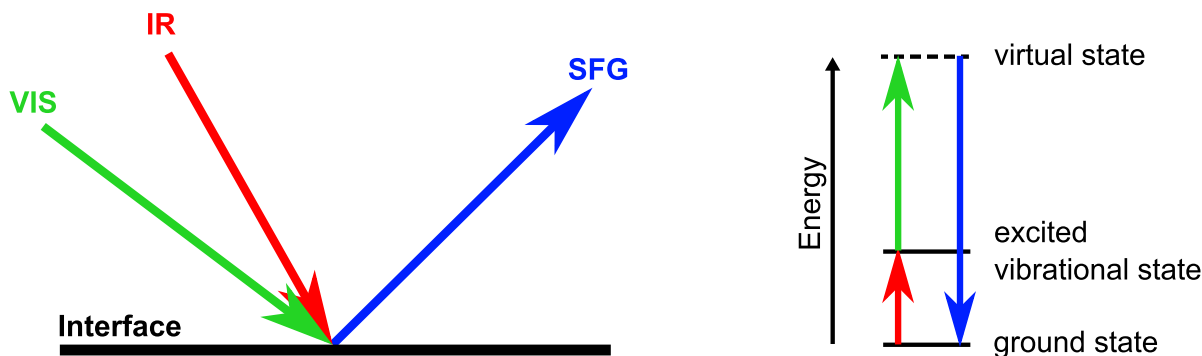


Figure 2.1: *Left: The incoming infrared (IR) and visible (VIS) laser beams generate a SFG-response at the interface between two materials. Right: Schematic energy diagram of the SFG-process. The IR excites a molecular vibration at the interface. The visible beam upconverts the excited molecules into a virtual state. A photon with the sum of the two incoming frequencies is emitted.*

Applying femtosecond-laser-systems, usually a broad band IR and a narrow band VIS beam are used for the SFG-process. Due to its extremely short time, the IR pulses frequency is fraught with a high uncertainty (time-energy-uncertainty relation). Apart from a high time resolution for dynamic processes, the advantage of such femtosecond-systems is the ability to obtain a whole spectrum in one shot, without the necessity of tuning the frequency. In order to get frequency resolution needed to identify different molecular species, however, the visible laser beam is narrowed to a few wavenumbers, resulting in a pulse longer in time. Figure 2.2 sketches this difference.

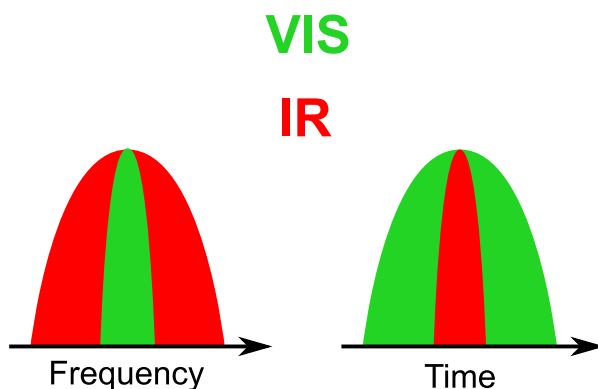


Figure 2.2: *Schematic display of the broadband IR and narrow band VIS in frequency (left) and time (right) domain.*

For the SFG-process to work, the molecules have to fulfill two conditions. Firstly, they have to be infrared-active. For this, the dipole moment of the molecule must be able to change during the IR induced vibration. Secondly, the molecules have to be Raman-active [38]. The schematic diagram of the SFG-process in figure 2.1 shows, that after the IR excitation the upconversion and following emission of the SF-photon happen in an anti-Stokes scattering manner. For this to happen, upon interaction with the VIS laser beam the molecules' electron cloud must be able to change its polarisability.

These two conditions can not be fulfilled by centrosymmetric molecules, such as CO_2 . Due to the non-linear and collective nature underlying the SFG-process, it is also forbidden in centrosymmetric media of non-centrosymmetric molecules, such as bulk water, where in the vicinity of every molecule a molecule with the opposite direction can be found. If the centrosymmetry is broken, however, the process is allowed. For water, the interface is usually non-centrosymmetric, since the water molecules do not have a neighbour oriented in opposite direction. This makes SFG intrinsically surface-specific. Additionally this means the more molecules are oriented, the higher the SFG-signal gets. The details of the SFG-theory will be discussed in section 2.2.

2.2 Theory

The following derivation of the background on SFG-spectroscopy is based on the review article of Lambert, Davies and Neivandt from 2005 [39]. Bold letters show the vectorial nature of the respective factor.

2.2.1 The non-linear Light-Matter-Interaction

When light travels through a medium, its electric field induces a dipole by influencing the electrons of the materials, according to

$$\boldsymbol{\mu} = \boldsymbol{\mu}_0 + \alpha \mathbf{E} \quad (2.2)$$

with μ_0 being the materials permanent dipole and α the electrons polarizability, which, in simple words, is the flexibility of the molecules' electron cloud. In order to apply this concept from single molecules to the entirety of a material, the bulk polarizability \mathbf{P} can be defined, by summing up the molecular electric dipoles, omitting $\boldsymbol{\mu}_0$:

$$\mathbf{P} = \epsilon_0 \chi^{(1)} \mathbf{E} \quad (2.3)$$

Here $\chi^{(1)}$ is the first order, or linear, susceptibility of the material, which is the averaged α over all the molecules in the system. ϵ_0 is the vacuum permittivity.

The equations derived above only hold true when the electric field of the incident light is weak. If the field strength reaches that of the molecular electric field acting on the electron, higher order terms cannot be neglected [40]. This is the case when pulsed laser systems are used. The dipole from equation 2.2 can then be expressed by a series expansion

$$\boldsymbol{\mu} = \boldsymbol{\mu}_0 + \alpha \mathbf{E} + \beta \mathbf{E}^2 + \gamma \mathbf{E}^3 + \dots \quad (2.4)$$

with β and γ being the first- and the second order hyperpolarizability. Accordingly the polarization P will change to

$$\mathbf{P} = \epsilon_0 (\chi^{(1)} \mathbf{E} + \chi^{(2)} \mathbf{E}^2 + \chi^{(3)} \mathbf{E}^3 + \dots) \quad (2.5)$$

with $\chi^{(2)}$ and $\chi^{(3)}$ being the second- and the third-order non-linear susceptibilities. By now using the frequency dependent expression of the electric field

$$\mathbf{E} = \mathbf{E}_1 \cdot \cos(\omega t) \quad (2.6)$$

the induced polarization can (after some rearrangement) be connected to the frequency of the incoming light by:

$$\mathbf{P} = \epsilon_0 \left(\chi^{(1)} \mathbf{E}_1 \cos(\omega t) + \frac{\chi^{(2)}}{2} \mathbf{E}_1^2 (1 + \cos(2\omega t)) + \frac{\chi^{(3)}}{4} \mathbf{E}_1^3 (3 \cdot \cos(\omega t) + \cos(3\omega t)) + \dots \right) \quad (2.7)$$

The first term shows that, when the incoming light reaches the material, it induces a polarisation which oscillates at the same frequency as the light. As a result the molecules will emit light of the same energy, which will show the materials linear optical properties such as diffraction. The other two terms, on the other hand, show that the molecules additionally emit light of twice (second harmonic generation) and even three times (third harmonic generation) the frequency of the incoming light. If now two electric fields of different frequency are assumed, for example by using two laser beams, the field can be written as:

$$\mathbf{E} = \mathbf{E}_1 \cos(\omega_1 t) + \mathbf{E}_2 \cos(\omega_2 t) \quad (2.8)$$

For SFG, only the second order polarization $\mathbf{P}^{(2)}$ of the material is of interest. Therefore, by combining the quadratic part of equation 2.7 with equation 2.8, the complete second order response can be derived.

$$\mathbf{P}^{(2)} = \frac{1}{2} \epsilon_0 \left(\underbrace{(\mathbf{E}_1^2 + \mathbf{E}_2^2)}_{\text{DC-Fields}} + \underbrace{(\mathbf{E}_1^2 \cos(2\omega_1 t) + \mathbf{E}_2^2 \cos(2\omega_2 t))}_{\text{SHG for both frequencies}} + \underbrace{2\mathbf{E}_1 \mathbf{E}_2 \cos((\omega_1 - \omega_2) t)}_{\text{DFG}} + \underbrace{2\mathbf{E}_1 \mathbf{E}_2 \cos((\omega_1 + \omega_2) t)}_{\text{SFG}} \right) \quad (2.9)$$

Accordingly, the second order non-linear response results in a frequency independent DC-field and a second harmonic (SHG) response for both the incoming frequencies. Additionally, a signal with the difference of the two frequencies (DFG) and the desired sum frequency response (SFG) are included. As a simplification for the relation between

the sum frequency component and the second-order polarization, the time dependence of the electric field can be omitted. Considering the use of a visible (VIS) and an infrared (IR) beam for SFG measurements, the following relation between the sum frequency component of the second order polarization and the incoming E fields can be derived:

$$\mathbf{P}^{(2)} = \epsilon_0 \chi^{(2)} \mathbf{E}_{\text{VIS}} \mathbf{E}_{\text{IR}} \quad (2.10)$$

Here, \mathbf{E}_{VIS} and \mathbf{E}_{IR} are the general local fields present at the surface. In the next section, the influence of polarization of the incoming beams on the polarization of the local fields will be discussed in more detail.

2.2.2 The E-Fields Polarisation

The s- (senkrecht) and p-polarized (parallel) components (with respect to the plane of incidence) of the incoming E-fields can be described separately when considering light acting on a planar surface, since their behaviour differs. Equations 2.11 show the separation of the components of the E-fields at the surface with respect to the x , y and z directions, with Θ_I being the angle of incidence of the incoming beam to the surface normal.

$$\begin{aligned} E_x^I &= E_p^I \cos(\Theta_I) \\ E_y^I &= E_s^I \\ E_z^I &= E_p^I \sin(\Theta_I) \end{aligned} \quad (2.11)$$

It can be seen that the s -polarized part of the surface E-field only reaches into the y -direction at the surface, whereas the p -polarized component stretches into the x - and the z -direction. Figure 2.3 shows this finding schematically.

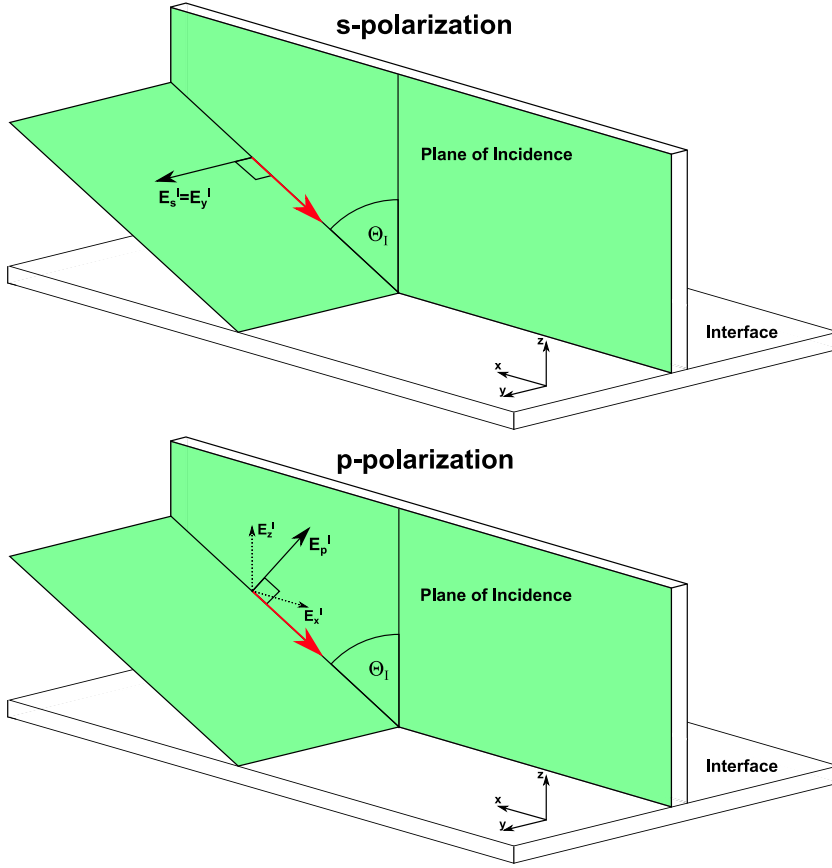


Figure 2.3: *s*- (top) and *p*-polarized (bottom) light falling on a plane surface. The *s*-polarized electric field exclusively has components in the *y*-direction, whereas the *p*-polarized *E*-field stretches in the *x*- and the *z*-direction, as was depicted in equation 2.11.

This model considers the lights *E*-fields traveling through space. However, when light falls on a surface, it undergoes reflection and transmission. The magnitude of reflection (r) and transmission (t) can be derived from the Fresnel-factors for *s*- and *p*-polarized light separately, as:

$$\begin{aligned}
 r_s &= \left(\frac{E_s^R}{E_s^I} \right) = \frac{n_I \cos(\Theta_I) - n_T \cos(\Theta_T)}{n_I \cos(\Theta_I) + n_T \cos(\Theta_T)} \\
 r_p &= \left(\frac{E_p^R}{E_p^I} \right) = \frac{n_T \cos(\Theta_I) - n_I \cos(\Theta_T)}{n_I \cos(\Theta_T) + n_T \cos(\Theta_I)}
 \end{aligned} \tag{2.12}$$

$$\begin{aligned}
 t_s &= \left(\frac{E_s^T}{E_s^I} \right) = \frac{2n_I \cos(\Theta_I)}{n_I \cos(\Theta_I) + n_T \cos(\Theta_T)} \\
 t_p &= \left(\frac{E_p^T}{E_p^I} \right) = \frac{2n_I \cos(\Theta_I)}{n_I \cos(\Theta_T) + n_T \cos(\Theta_I)}
 \end{aligned} \tag{2.13}$$

Here Θ_I and Θ_T are the angles of the incident and transmitted light, respectively. n_I and n_T are the refractive indices of the respective materials that the incoming and transmitted beams travel through.

The magnitudes of the xyz -components of the interfacial electric fields now can be derived using equations 2.11 and 2.12, by considering that the E-field present is the sum of the incident and the reflected beams:

$$E_x = E_x^I + E_x^R = E_x^I + r_p E_x^I = -E_p^I \cos(\Theta_I) (1 - r_p) = K_x E_p^I \quad (2.14)$$

$$E_y = E_y^I + E_y^R = E_y^I + r_s E_y^I = E_s^I + r_s E_s^I = E_s^I (1 + r_s) = K_y E_s^I \quad (2.15)$$

$$E_z = E_z^I + E_z^R = E_z^I + r_p E_z^I = E_p^I \sin(\Theta_I) (1 + r_p) = K_z E_p^I \quad (2.16)$$

Here $K_{x/y/z}$ are the so called K-factors, that simplify the generalization of the equations. Using this knowledge and equation 2.10, the components of the direction dependent non-linear bulk polarisation can be derived. As can be seen in equation 2.10, $\chi^{(2)}$ is a third-rank tensor connecting three vectors, namely $\mathbf{P}^{(2)}$ with \mathbf{E}_{VIS} and \mathbf{E}_{IR} of the incoming beams. As such, considering the field components in xyz -direction for the two E-fields, it has 27 different components. Therefore equation 2.10 can be rewritten as:

$$\mathbf{P}_{\text{SF}}^{(2)} = \sum_i^{x,y,z} \mathbf{P}_{i,\text{SF}}^{(2)} = \epsilon_0 \sum_i^{x,y,z} \sum_j^{x,y,z} \sum_k^{x,y,z} \chi_{ijk}^{(2)} \mathbf{E}_{j,\text{VIS}} \mathbf{E}_{k,\text{IR}} \quad (2.17)$$

or, by making use of the K-factors,

$$\mathbf{P}_{i,\text{SF}}^{(2)} = \epsilon_0 \chi_{ijk}^{(2)} K_j E_{p/s,\text{VIS}}^I K_k E_{p/s,\text{IR}}^I \quad (2.18)$$

From equation 2.17, it gets clear that there are 3^3 possible possibilities to combine $\chi_{ijk}^{(2)}$ with x , y and z (for example $\chi_{xxz}^{(2)}$). However, on a surface with an isotropic structure (x and y direction are equivalent, z is the surface normal), not all combinations contribute to the SFG-signal.

Considering a centrosymmetric medium, all directions are equivalent, resulting in the same value for $\chi_{ijk}^{(2)}$ for opposing directions. Therefore:

$$\chi_{ijk}^{(2)} = \chi_{-i-j-k}^{(2)} \quad (2.19)$$

However, due to the fact that $\chi_{ijk}^{(2)}$ is a third rank tensor, as mentioned before, the reversion of the coordinates must result in the reversion of the physical phenomenon, according to

$$\chi_{ijk}^{(2)} = -\chi_{-i-j-k}^{(2)} \quad (2.20)$$

The only solution to both equations at the same time is $\chi_{ijk}^{(2)} = 0$. For this reason, SFG is forbidden in centrosymmetric media. This, however, does not apply for interfaces between two materials, since $\chi^{(2)}$ for z and $-z$ are not equivalent. Therefore, in order to identify the non-zero tensor elements of $\chi_{ijk}^{(2)}$, two rules must apply: first, at least one contribution in the z direction must be present. Second, the number of x or y must be 0 or 2. Considering these two rules, only 7 non-zero tensor elements are left. Also considering the fact, that x and y are equivalent, only four different elements can be identified.

$$\chi_{zxx}^{(2)} = (\chi_{zyy}^{(2)}); \chi_{xzx}^{(2)} = (\chi_{yzy}^{(2)}); \chi_{xxz}^{(2)} = (\chi_{yyz}^{(2)}); \chi_{zzz}^{(2)} \quad (2.21)$$

2.2.3 The Generated SF-Response

Now the connection of the incoming, polarised electric fields with the induced macroscopic, non-linear polarisation at the interface has been made. This polarisation on the other hand induces a surface bound sum frequency electric field, which leads to the emission of the SF light, that is detected in the SFG experiment. As a reminder, from equation 2.9 it is known that the frequency of SFG light is the sum of the two incoming beams, as has already been shown in equation 2.1.

The angles (Θ_{VIS} and Θ_{IR}) and the frequency of the incoming beams also determine the angle of the outgoing SFG response (Θ_{SF}), due to the conservation of momentum. This relation is called the phase matching condition.

$$n_{\text{SF}}k_{\text{SF}}\sin(\Theta_{\text{SFG}}) = n_{\text{VIS}}k_{\text{VIS}}\sin(\Theta_{\text{VIS}}) + n_{\text{IR}}k_{\text{IR}}\sin(\Theta_{\text{IR}}) \quad (2.22)$$

Here k_i is equal to $\frac{\omega_i}{c}$, where c is the speed of light.

The surface polarization and the emitted E-field are connected by the non-linear SF Fresnel-factors, according to:

$$\mathbf{E}_{i,\text{SF}} = L_i \mathbf{P}_{i,\text{SF}}^{(2)} \quad (2.23)$$

where L_i is the SF Fresnel-factor in the i direction ($=x$ -, y -, or z -direction) [41, 42].

As has been explained before, $\mathbf{E}_{i,\text{SF}}$ is the emitted E-field, produced by the induced polarisation of the surface $\mathbf{P}_{i,\text{SF}}$. The intensity of the emitted light is the sum of the squared magnitudes of the SF E-field.

$$\begin{aligned}
I_{p,\text{SF}} &\propto |\mathbf{E}_{x,\text{SF}}|^2 + |\mathbf{E}_{z,\text{SF}}|^2 \\
&\propto \left| L_x \mathbf{P}_{x,\text{SF}}^{(2)} \right|^2 + \left| L_z \mathbf{P}_{z,\text{SF}}^{(2)} \right|^2 \\
&\propto \left| L_x \sum_j^{x,y,z} \sum_k^{x,y,z} \epsilon_0 \chi_{xjk}^{(2)} K_j E_{p,\text{VIS}}^I K_k E_{p,\text{IR}}^I \right|^2 \\
&\quad + \left| L_z \sum_j^{x,y,z} \sum_k^{x,y,z} \epsilon_0 \chi_{zjk}^{(2)} K_j E_{p,\text{VIS}}^I K_k E_{p,\text{IR}}^I \right|^2
\end{aligned} \tag{2.24}$$

$$\begin{aligned}
I_{s,\text{SF}} &\propto |\mathbf{E}_{y,\text{SF}}^I|^2 \\
&\propto \left| L_y \mathbf{P}_{y,\text{SF}}^{(2)} \right|^2 \\
&\propto \left| L_y \sum_j^{x,y,z} \sum_k^{x,y,z} \epsilon_0 \chi_{yjk}^{(2)} K_j E_{p,\text{VIS}}^I K_k E_{p,\text{IR}}^I \right|^2
\end{aligned} \tag{2.25}$$

2.2.4 How the Signal Depends on the IR-Wavelength: The Lorentzian-Model

In all derivations above, the only wavelength-dependent factor is the second-order non-linear susceptibility $\chi_{ijk}^{(2)}$, which describes the influence of the lights E-field on the macroscopic non-linear polarisation. When the infrared wavelength is in resonance with a molecular vibration in the studied system, $\chi_{ijk}^{(2)}$ is strongly enhanced, which makes it possible to obtain information about the interfacial chemical composition and structure. The connection between the frequency and the non-linear susceptibility can be given by a Lorentzian model, which can also be used to fit and analyse the data obtained in a SFG-experiment.

However, also other processes than resonances can contribute to the SF-signal. The origin of these contributions is not fully understood, though they are often considered to be electronic responses. These additional signals are usually frequency independent and therefore are called non-resonant signals. Considering the aforementioned frequency dependence and the non-resonant signal, the non-linear susceptibility can be written as:

$$\chi^{(2)} \approx \chi_{\text{NR}}^{(2)} + \chi_j^{(2)} = A_0 e^{i\varphi} + \sum_{j=1}^N \frac{A_j}{\omega_j - \omega_{\text{IR}} + i\Gamma_j} \tag{2.26}$$

$\chi_{\text{NR}}^{(2)}$ is the non-resonant signal, which can be also described by an amplitude A_0 and phase φ . $\chi_j^{(2)}$ is the j th resonance, described by the frequency ω_j , the spectral width Γ_j and the amplitude A_j . The latter one can be positive or negative, which contains information of the absolute orientation of the resonating molecules studied. However, since in general an SFG-spectrum is obtained by measuring the intensity of the electric field emitted, which

is its absolute square as seen in equations 2.24 and 2.25, this orientation information is lost in conventional SFG described so far.

In order to obtain the absolute orientation of the molecules, an extended SFG-technique has to be deployed, called phase-resolved SFG-spectroscopy. In this experiment, first a non-resonant signal is generated at a local oscillator (LO) by the incoming VIS and IR beams. The reflection of the two incoming beams is then combined with the generated LO-SFG on the sample itself. The VIS and IR beams generate the normal SFG signal from the sample, which then interferes with the LO-signal. By first fast-Fourier- and then inverse-fast-Fourier-transforming the interference pattern, the imaginary part of $\chi^{(2)}$, $\text{Im}[\chi^{(2)}]$, can be obtained, which gives the phase-information of the sample molecules (for details see [43]).

2.3 Time-Resolved Pump-Probe-SFG-Spectroscopy

Static SFG-experiments, as have been described so far, are the ideal tool to study the structure and interaction of water molecules at the interface to other materials. However, this only applies for equilibrated systems, or systems with an equilibration time in the range of seconds to minutes. As a result nothing can be learned about molecular dynamics or energy dissipation between molecules, since these phenomena happen on the range of femto- to picoseconds. However, they play an important role in the fundamentals of chemical reactions, such as in the photocatalytic splitting of water at the TiO_2 -interface, since they might influence reaction kinetics and energetics.

In order to learn more about the dynamic behaviour of water, the sum frequency generation experiment can be modified by adding a second IR beam (IR_{Pump}). This usually narrow band beam is in resonance with a sub-ensemble of water molecules in the broad hydrogen-bonded OH-stretch vibration. When these molecules are excited, they do not contribute to the SFG (probe) signal, the ground state gets partially depleted. The result is a decrease in signal intensity. However, when the time between the pump-perturbation and the probe pulses is long enough, the excited molecules will have dissipated their energy and will be available for the probe SFG. Upon varying this time delay step by step, information about the flow of energy can be obtained. Figure 2.4 shows the underlying process schematically.

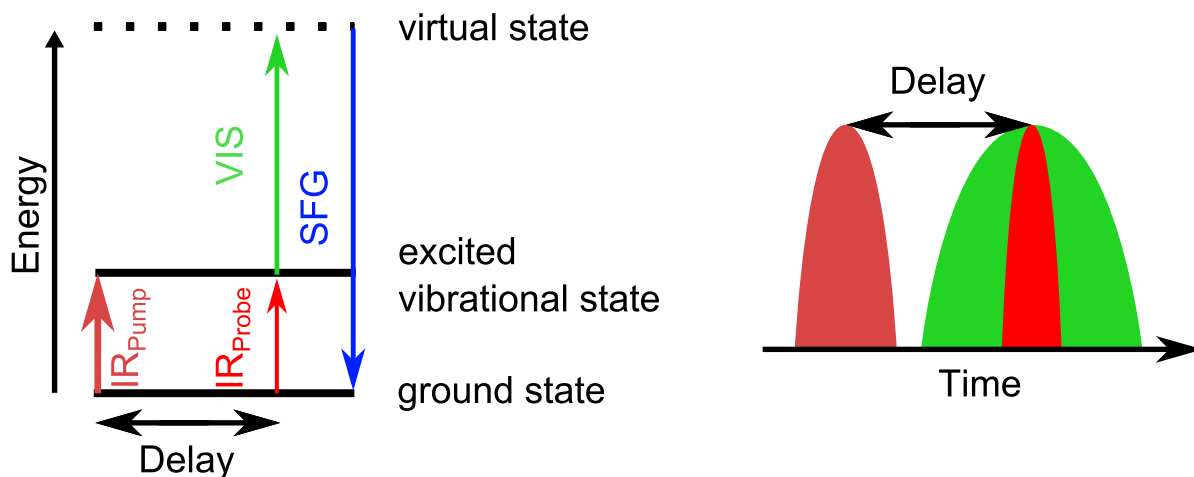


Figure 2.4: *Left: Energy diagram of a pump-probe-SFG experiment. Due to the depletion of the ground state, caused by the pump-pulse, the SFG-signal intensity is reduced (arrow thickness). Right: Pulse length and time delay of the pump and the probe beams.*

In pump-probe SFG measurements the perturbation of the water system from its equilibrium is observed. In order to see the influence of the pump IR beam on the water molecules compared to the uninfluenced system, pumped and unpumped spectra are recorded in an alternating manner for each time step (for technical details see section 2.4). By dividing the unpumped by the pumped spectrum for each time step measured and plotting the result against the delay time between the pump- and the probe-pulses, a time trace is obtained. In the case of water, in order to extract the time constants from these time traces, a four level model for the molecular relaxation pathway and kinetics is assumed [44, 45]. Figure 2.5 shows this model schematically.

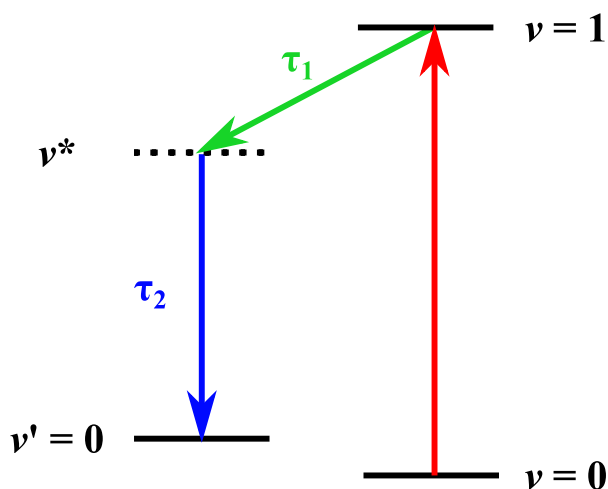


Figure 2.5: *Schematic representation of the four level model used to interpret pump-probe SFG data. The IR_{Pump} excites molecules from the ground state ($v = 0$) into the first excited state ($v = 1$). After the time τ_1 they relax into an intermediate state (v^*) and from there into a heated ground state ($v' = 0$), with the decay time τ_2 .*

In this model, The IR-pump-pulse vibrationally excites the water molecules from their ground state ($v = 0$) into the first excited state ($v = 1$). From this state, the molecules relax into the intermediate state v^* , with the delay time τ_1 . After the decay time τ_2 , the molecules further relax into a heated ground state ($v' = 0$), that differs from $v = 0$ due to the increased heat energy, dumped into the system by the pump-pulse.

The intermediate state v^* has been found in femtosecond infrared pump-probe measurements of concentrated alkali-halide solutions of isotopically diluted water [46]. This state is necessary to explain the delayed rise of the thermal difference spectrum with respect to the vibrational relaxation of the excited OD stretch vibration. However, spectrally this state is identical to the OD-stretch vibration and is considered to be dark in IR-pump-IR-probe [47].

From this four level scheme, the lifetime of the excited vibrational state, and therefore the time that the molecules need to dissipate the vibrational energy, can be extracted. For that, the change in the states' populations have to be calculated by solving the following differential equations:

$$\begin{aligned}
\frac{\partial N_0}{\partial t} &= -\sigma_0 I(t)[N_0 - N_1] \\
\frac{\partial N_1}{\partial t} &= \sigma_0 I(t)[N_0 - N_1] - \frac{N_1}{\tau_1} \\
\frac{\partial N_{v^*}}{\partial t} &= \frac{N_1}{\tau_1} - \frac{N_{v^*}}{\tau_2} \\
\frac{\partial N_{v'}}{\partial t} &= \frac{N_{v^*}}{\tau_2}
\end{aligned} \tag{2.27}$$

Here N_0 , N_1 and N_{v^*} are the population of the ground state, the excited state and the intermediate state, respectively. $N_{v'}$ is the heated ground state, which is a result of the energy originating from the pump-pulse that is dissipated into the water bath. The relaxation (or better: cooling) into the non-heated ground state exceeds the experimental time by far, therefore a stable v' can be assumed. The absorption cross section of water for the IR_{Pump} pulse is described by σ_0 , whereas t is the time. Finally, $I(t)$ describes the instrument response function. This term is defined by the Gaussian approximation of the pump pulse time profile (FWHM ≈ 200 fs).

The time traces are extracted from SFG spectra, therefore it is necessary to connect the differential expressions from equation 2.27 to the SFG response in the system, or better, to the change in SFG-signal upon ground state depletion by the IR_{Pump} .

$$\Delta I_{\text{SFG}}^N(t) \propto \frac{\chi_0 ((N_0(t) - N_1(t)) + \chi_{v^*} N_{v^*}(t) + \chi_{v'} N_{v'}(t))^2}{\chi_0 (N_0(t \ll 0))^2} \tag{2.28}$$

Under the assumption, that $\chi_0 = \chi_{v^*}$ [47], equation 2.28 can be written as:

$$\Delta I_{\text{SFG}}^N(t) = \frac{(N_0(t) - N_1(t) + N_{v^*}(t) + O_{v'} N_{v'}(t))^2}{(N_0(t \ll 0))^2} \tag{2.29}$$

The laser light is generated by a Ti-sapphire laser (Libra system, Coherent) with a pulse duration of about 50 *fs*, a repetition rate of 1 *kHz* and an output energy of about 5 *W*. The light has a wavelength of 800 *nm*. The pulse is split in two by a beam splitter (BS1 = beam splitter1) directly after the laser. The transmitted light (light green, 0.97 *W*) is narrowed down by an Etalon to a bandwidth of about 15 *cm⁻¹*, reducing the energy to about 42 *mW*. This narrow band beam is used as the VIS for the SFG process. A delay stage matches the path length to the paths of the other beams, to enable overlap in time. The reflected part of the initial laser light is split again into two beams (BS2). A third beam splitter (BS3) reflects about 2.1 *W* into an automated optical parametric amplifier (TOPAS Prime, Light Conversion)(TOPAS1) with a subsequent NDFG-stage to generate a broad band infrared pulse (IR, red), that is used in the SFG process. Various filters (F) block leakages of other, undesired frequencies, resulting in an IR-energy of about 10-20 *mW*, depending on the IR-frequency.

Through a series of half-wave-plates ($\lambda/2$) and polarisers (P), the desired polarisation for the VIS and the IR beams are selected. Afterward, they are overlapped in space and time on the sample using lenses of 12 *cm* (VIS) and 7.5 *cm* (IR) focal length. The reflections of VIS and IR are blocked and only the SFG beam (blue) is sent to the camera.

On the detection path the SFG signal passes a collimating lens (L_{coll}) of 12 *cm* focal length, to collimate the light. Afterward a cylindrical lens narrows the beam vertically to a horizontal, thin line ($L_{\text{cyl/h}}$, $f = 25$ *cm*). Again with a half-wave-plate and a polariser the desired polarisation can be selected, just before a second cylindrical lens narrows the beam horizontally ($L_{\text{cyl/v}}$; $f = 5$ *cm*) to a point on the slit in the spectrometer. The spectrometer (Shamrock 303i, Andor) disperses the light and sends it frequency resolved to a CCD-chip (EMCCD, Andor) of 400 times 1600 pixels, that detects the signal.

For the pump-probe measurements, the 800 *nm* light passing through BS3 (0.45 *W*) is sent into a second TOPAS, without subsequent NDFG-stage (TOPAS2). Here the light is converted into a signal and an idler beam. The latter (yellow) with a wavelength of about 2010 *nm* is frequency doubled by a β -barium borate (BBO) crystal. The result of about 1005 *nm* (brown) is combined (BC = beam combiner) with a part of the 800 *nm* beam, reflected by BS 2 (dark green, 1.3 *W*) in a lithium niobate (LiNbO₃) crystal, to generate the narrow band IR_{pump} (pink) with a power of about 20 *mW*.

The pump-IR beam is sent to an automated delay stage, in order to vary the delay time between the SFG beams and the pump excitation. After that, a chopper blocks every second pulse, resulting in a repetition rate of 500 *Hz* for the pump laser. In this way, every second SFG signal generated at the sample is pumped. The pump IR beam is focused on the sample using a lens with a focal length of 7.5 *cm*.

In the detection path the pumped and unpumped signals are separated using a vibrating mirror (VM), that is synchronised with the laser and the chopper, vibrating with 500 *Hz*, in order to spatially separate the pumped and the unpumped SFG signals on the CCD chip. In case of static SFG-measurements this vibrating mirror is turned off, so that it acts as a normal mirror.

In chapter 3 a series of experiments will be presented to demonstrate the capabilities of static Sum-Frequency-Generation-Spectroscopy on a system of water, sodium chloride and a surfactant.

3 Influence of Salt on the CMC and Dynamics of CTAB-Solutions

In this chapter the capabilities of static SFG-Spectroscopy will be demonstrated on a system consisting of water, sodium chloride and the surfactant cetyltrimethylammonium bromide (CTAB). First, a short introduction to surfactants and their interesting properties will be given. After that, it will be shown how SFG can serve as a complementary method for interpreting data obtained by surface tension measurements and how this technique can help understanding the mechanism and driving force of the surface activity of surfactants on water surfaces. Additionally the influence of salt on the critical micellar concentration (CMC) of surfactants will be discussed.

3.1 Definition and Properties of Surfactants

Surfactants (surface active agents) play a major role in our daily life. We encounter them in soaps and cosmetic products, in food, where they are known as emulsifiers and in pharmaceutical processes and products. But also for industrial applications surfactants play an important role, for example in the synthesis of polymeric nanoparticles [49], the coating of fibers and as foaming agents in chemical and technical processes. More special applications lie in agriculture and fire fighting, where they are added in small amounts to improve the wetting capabilities of pesticides and water, as well as in fire extinguishers. In general surfactants consist of two major parts: a hydrophobic tail and a hydrophilic head group [50]. The hydrophobic tail typically consists of alkyl chains and is able to interact with nonpolar substances such as organic liquids, polymers, etc. The hydrophilic head group contains polar or ionic functional groups such as $-\text{OH}$, $-\text{COOH}$, $-\text{NH}_3$, etc., and can dissolve in water. Since the two parts are bound in one single molecule, there are limited possibilities to minimize the free energy of both parts at the same time. One possibility is to build micelles in bulk water or oil. Considering surfactants in water, they would form spheres in such a way, that the head groups are pointing towards the water, whereas the hydrophobic alkyl chains are packed on the inside of the spheres, where they avoid the polar outside. If this sphere is filled with a nonpolar liquid such as oil, it is called an emulsion. In the case of water droplets in bulk oil, the term inverse-emulsion is used.

Another possibility for the hydrophobic tail of a surfactant molecule to escape water is the migration to the surface, where the alkyl chain can stick out into the air. Also the interaction with other hydrophobic interfaces is possible, for example in a plastic container, or the formation of a double layer. Figure 3.1 shows the aforementioned

behaviour of surfactants.

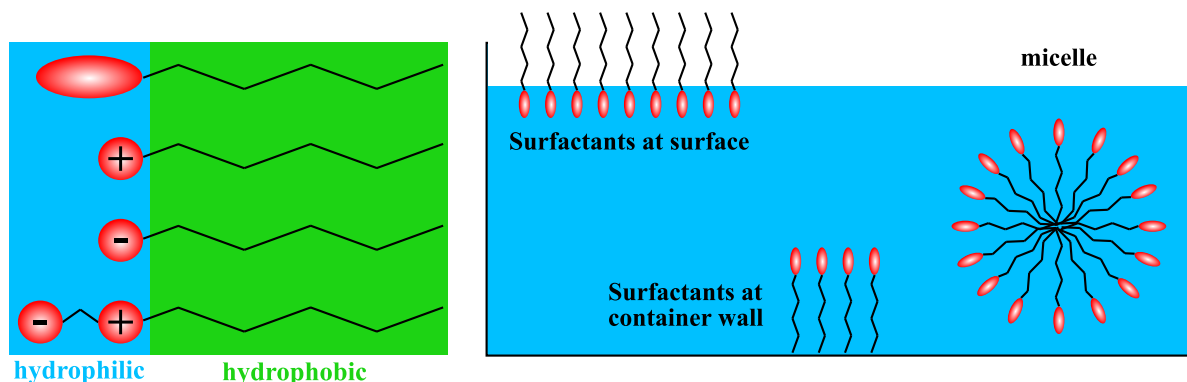


Figure 3.1: *Left: The general structure of surfactant molecules is the same with the hydrophilic head group and the hydrophobic tail. Depending on the functional group on the head group, the molecules can be grouped in neutral, positive, negative and zwitterionic surfactants (from top to bottom). Right: The surfactant molecules achieve minimal energy by shielding their hydrophobic tails from the water. This can be achieved by moving towards the surface, interact with the (hydrophobic) container wall or by building micelles (from left to right).*

At the water air interface, water has a surface tension of $72 \frac{mN}{m}$. The origin for this high surface tension lies in the hydrogen-bonding network between the molecules. In bulk, every water molecule is surrounded by other molecules with which it forms hydrogen-bonds. Therefore the force that acts on the molecules is the same in every direction. At the interface with air, the hydrogen-bonding network is broken, so that the upper most molecules only form hydrogen-bonds towards the bulk. This results in a directionality of the forces towards the bulk phase. Therefore, in order to create or expand a surface work has to be done, related to the free energy change of the surface [51].

When surfactants come to the water-air interface they interrupt the lateral hydrogen-bonding network and give the water molecules underneath a partner for interaction, where they could not find one before. This results in a drop of the surface tension, which means that increasing the surface area requires less energy. With the addition of more and more surfactant molecules the surface will eventually be fully covered, so that adding even more does not change the surface tension any more. The equilibrium state is reached.

To measure and visualise this effect, surface tension measurements can be conducted using tensiometers of different kinds. One possible technique is the Du Noüy ring method, where a wire ring is brought in contact with the surface and slowly pulled back, while measuring the force needed to pull [52]. The way to present the data is to plot the measured surface tension against the surfactant concentration on a logarithmic scale. Figure 3.2 shows this curve exemplary.

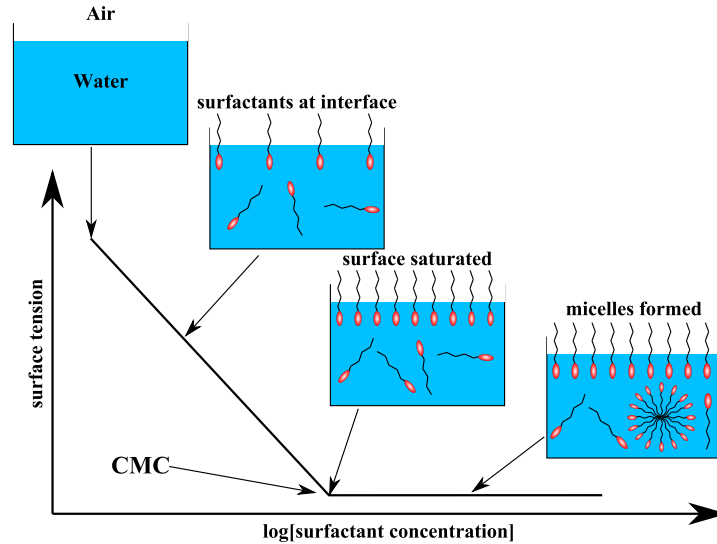


Figure 3.2: Typical shape of a surface tension versus surfactant concentration plot.

From these plots three major pieces of information can be obtained. First, the equilibrium surface tension which is the value at high surfactant concentrations when the surface is saturated with molecules. It is a measure of how strongly the interfacial water structure is disturbed by the additives. Second the critical micelle concentration (CMC), which is the concentration above which the surface tension is constant. At this point the surface is fully covered and the bulk is saturated with monomeric surfactant molecules. In order to reduce their energy the additives will form micelles. Third, the surface excess concentration can be obtained from the slope of the decreasing surface tension. The change of surface tension in dependence of concentration change is defined by the Gibbs-equation as [53]:

$$\partial\gamma = -nRT \cdot \Gamma \cdot \partial\ln(C) \quad (3.1)$$

Where γ is the surface tension, T the absolute temperature, R the universal gas constant, C is the surfactant concentration, and Γ is the surface excess concentration, with the unit $\frac{\text{mol}}{\text{m}^2}$, which is considered to be the concentration of surfactant molecules at the surface. n is a factor depending on the dissociation state of the surfactant.

In the next section the influence of CTAB on the surface tension will be presented, and how the presence of electrolytes changes this behaviour. Additionally, the dynamics of the surfactant adsorbing on the water surface will be presented.

3.2 Surface Tension and Dynamics of CTAB Solutions and the Influence of Salt

All measurements in this section were conducted, analysed and interpreted mainly by Mohsin Qazi from University of Amsterdam and taken from reference [54].

Figure 3.3 shows the structure of CTAB.

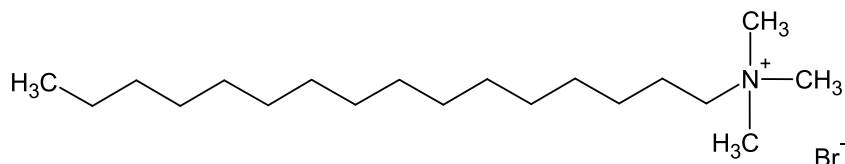


Figure 3.3: Structure of cetyltrimethylammonium bromide (CTAB)

CTAB is a typical cationic surfactant with a simple, 16 carbon alkyl chain serving as hydrophobic tail. The hydrophilic head group consists of a quaternary ammonium cation. The counter ion is bromide. It is used in polyepoxide coatings, for stabilization of nanoparticles or in several biochemical applications. The molar mass is $364.45 \frac{g}{mol}$ and it dissolves in water up to $3.1 \frac{g}{L}$ [55]. The CMC in pure water lies between 0.8 and 1.1 mM [56–58].

In this chapter, the unit m for concentrations is molality ($\frac{mol}{kg}$) for amount of substance in a specific amount of mass of the solvent. Accordingly mm is defined as *millimolal*. The effect of CTAB on the surface tension of water is shown in figure 3.4 for solutions with various salt concentrations between 0 and 5.5 m NaCl .

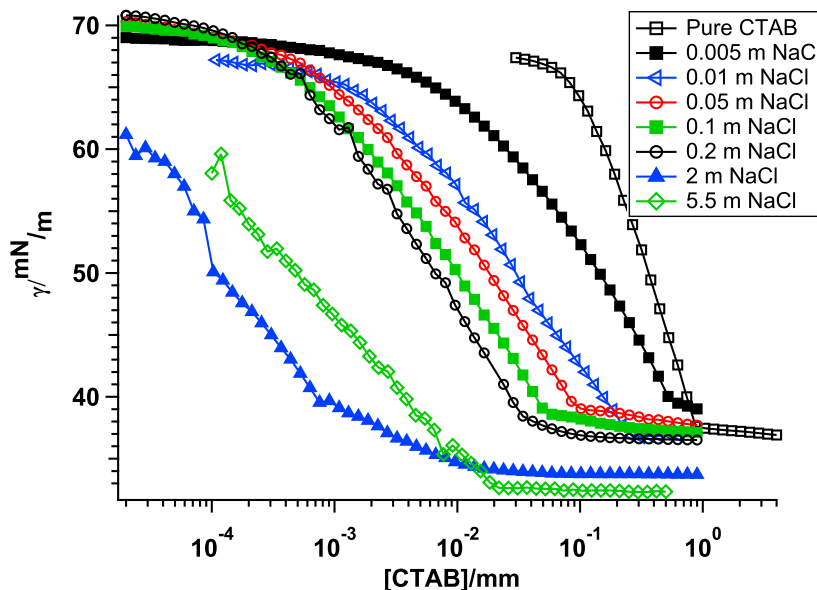


Figure 3.4: Surface tension of the water-CTAB-air interface for various salt concentrations. With rising electrolyte content the CMC and the equilibrium surface tension decreases. Also the surface excess concentration gradually gets smaller (slope).

As can clearly be seen from figure 3.4, the CMC decreases dramatically upon the addition of NaCl compared to the pure CTAB-water system, namely from $9 \cdot 10^{-4} \text{ m}$ (black empty squares) to $2 \cdot 10^{-5} \text{ m}$ (green empty rhombi). Interestingly the decrease stops at a sodium chloride concentration of 0.2 m (empty black circles) and stays constant for higher concentrations.

Additionally, the equilibrium surface tension decreases with increasing salt concentration (by about $\Delta\gamma_{\text{CMC}} \approx 5 \frac{\text{mN}}{\text{m}}$ at 5.5 m NaCl), as does the surface excess concentration (slope of each curve), although the trend is less pronounced for intermediate concentrations. These findings are in good agreement with the previous results of other groups [59, 60]. The decrease of the CMC upon increasing sodium chloride concentration shows, that the addition of electrolytes facilitates the aggregation of the surfactant molecules into micelles, due to the screening of their heads' electrostatic repulsion. This leads to a solution with less monomers. The fact that the drop of the CMC stops at 0.2 m NaCl seems to hint to the maximum screening capability of the salt towards the surfactant. The decrease in equilibrium surface tension at and above the CMC hints to a denser packing of surfactant molecules at the water-air-interface. If this true altogether will be discussed in the next section.

As stated before, interestingly the surface excess concentration also decreases with increasing salt concentration. Without further consideration, this could lead to the conclusion that the addition of salt even partly reduces the packing density of the charged surfactant molecules at the water-air interface. This is counter intuitive, since the screening of the charge present in the molecules' head group, if anything, should facilitate their packing at the interface. The answer to this dilemma lies in the Gibbs equation (3.1), in the change of the factor n , which depends on the surfactants dissociation state. If this factor changes from 2 for a fully separated ion pair to 1 for an ion-condensed state, the surface excess concentration will be more or less the same for CTAB solutions with and without salt [54]. More details will be given below.

So far, only equilibrated systems of CTAB solutions with varying salt concentrations have been discussed. However, for many applications also the dynamic behaviour of surfactants is important, such as inkjet printing, atmospheric cloud formation or the wetting behaviour of pesticides in agriculture, since these processes happen on the order of milliseconds [61–63]. In order to learn more about the dynamics of the surface covering mechanism of surfactants it is necessary to measure the surface tension in a time dependent manner on a freshly formed surface. Depending on the timescale of the equilibration different methods can be used for these dynamic surface tension (DST) measurements. For short timescales in the range of tens of milliseconds a bubble pressure tensiometer can be used. For longer time scales in the range of several seconds to minutes the pendant drop method is a good choice.

In this way several systems have been studied, namely pure water-surfactant solutions of different concentrations, solutions with fixed salt and variable CTAB concentrations and solutions with fixed surfactant and various NaCl concentrations.

Figure 3.5 shows the time dependence of the surface tension for freshly formed surfaces with varying surfactant concentration without additional electrolyte, measured using the bubble pressure tensiometer.

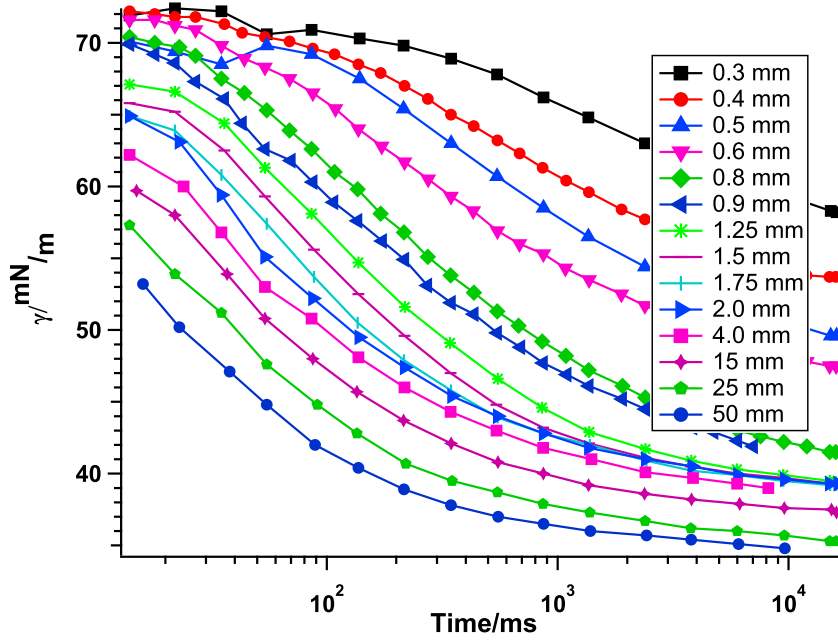


Figure 3.5: DST measurements for various CTAB concentrations.

Figure 3.5 clearly shows that upon increasing the CTAB concentration from 0.3 *mm* (black squares) to 50 *mm* (blue disks) the time needed for equilibrating the surface tension decreases, thus the dynamics get faster. Upon further analysis of the data, it can be concluded that the surface covering mechanism of CTAB at the air water interface is a diffusion controlled process. For further details see [54].

The same trend could be shown for changing CTAB concentrations but with a fixed NaCl concentration of 5.5 *m* (see figure 3.6). However, the dynamics itself is slowed down from the range of tens of *ms* to tens of *s*.

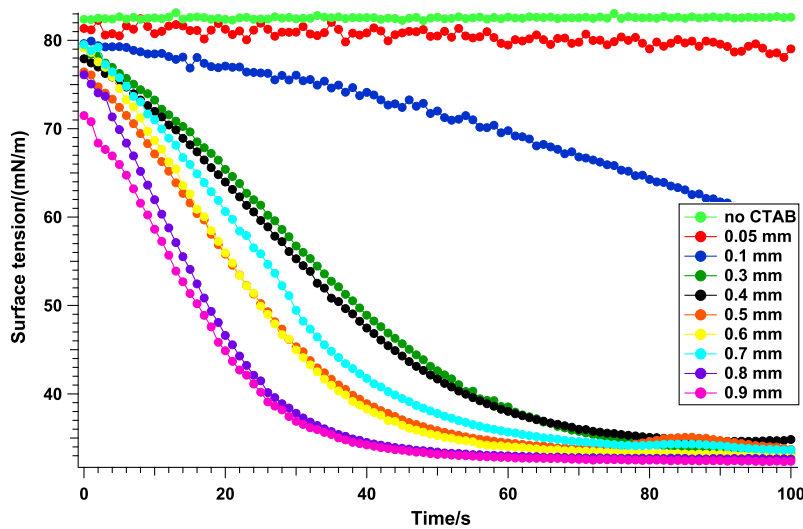


Figure 3.6: Dynamic surface tension for various CTAB concentration with 5.5 *m* NaCl.

As mentioned before, the trend of an accelerated equilibration of surface coverage with increasing CTAB concentration can be observed, similar to the trend of pure CTAB solutions. However, the overall equilibration time is a lot larger for the CTAB solution with electrolyte than for pure CTAB solutions. This hints to the fact, that coverage of the surface is a process governed by the diffusion of monomers towards the surface. If salt is present and the surfactants head groups charge is screened, micelles are formed easier in the solution, due to the reduced repulsion between the molecules. Therefore less monomers are available for covering the surface, which results in a slower decrease of the surface tension. For further details see [54].

To show that the deceleration of the surfactants dynamics with increasing NaCl concentration follows a trend, a third set of measurements has been conducted, in which the CTAB concentration was fixed at 0.3 mmol and the amount of salt was varied. The results are shown in figure 3.7.

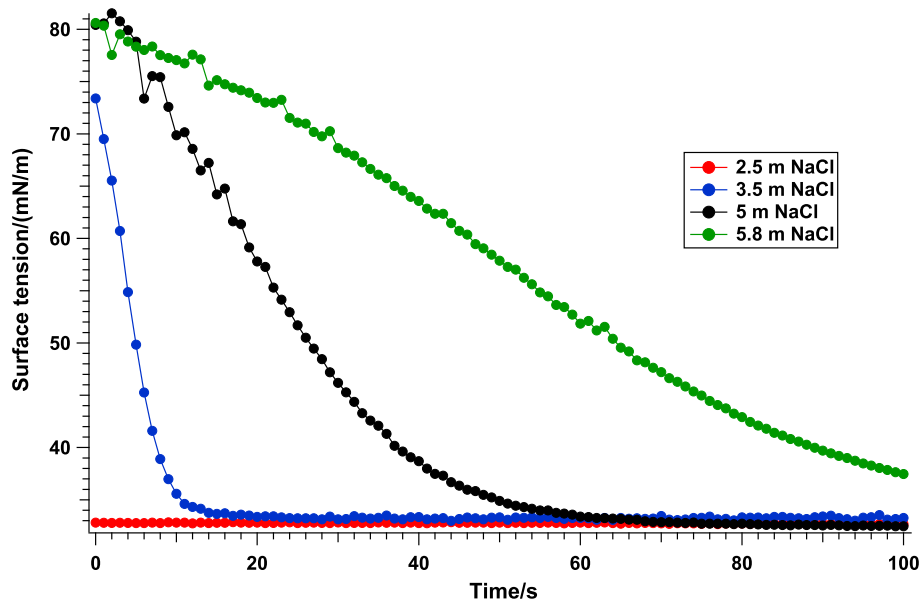


Figure 3.7: *Dynamic surface tension for various salt concentrations with 0.3 mmolal CTAB*

Figure 3.7 clearly shows a trend towards slower dynamics upon increasing salt concentration. It is important to note, that the amounts of NaCl used in this measurement are close to the maximum of solubility of the electrolyte. As mentioned before, this massive amount of ions could influence the dissociation (more precise: the ion pairing) equilibrium of CTAB towards the associated species according to:



It is also possible and very likely, that Br^- is substituted with Cl^- in equation 3.2, since high amounts of NaCl were used.

In order to get further insights into the dynamics of the CTAB migration towards and its

structure at the water-air-interface, supplementary SFG-measurements were conducted on different solutions of CTAB with and without salt. These results will be presented in the next section.

3.3 SFG on the Water-CTAB-NaCl System

In this section results of SFG experiments conducted on CTAB solutions of three different surfactant concentrations with and without salt will be presented.

Figure 3.8 shows SFG-spectra of 0.9, 0.1 and 0.01 *mm* CTAB, with and without 5.5 *m* NaCl. As a reminder, *m* and *mm* here mean molality and millimolality, respectively. All spectra were measured with an acquisition time of 10 *min*, after equilibration of the surface. After subtracting a background signal (10 min acquisition with the IR-beam blocked) the data were normalised to the non-resonant signal of a 100 *nm* gold reference (30 s acquisition time, background corrected the same way as the sample spectra). This step is important in order to correct for the approximately gaussian-shaped frequency profile of the IR-beam. The resulting spectra are shown in figure 3.8, where the SFG-intensity is plotted against the IR-frequency in wavenumbers.

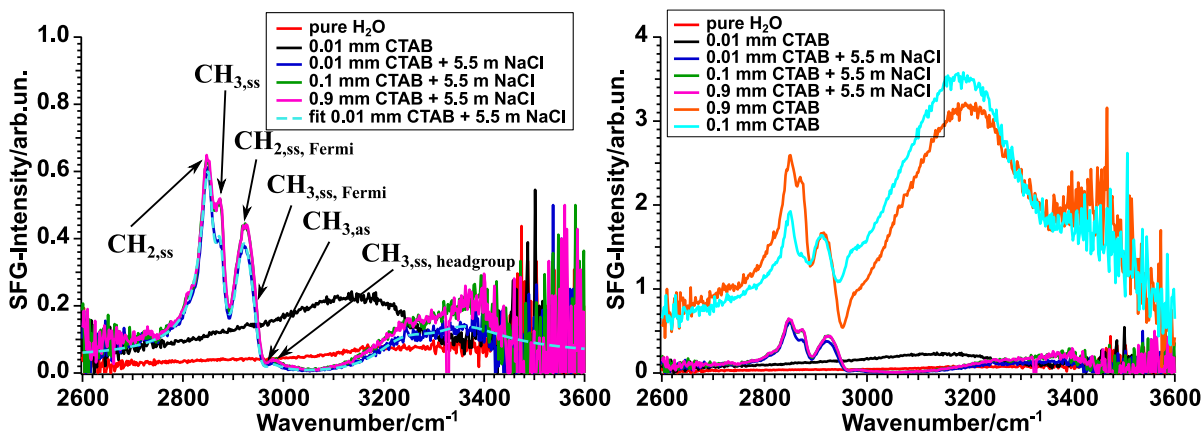


Figure 3.8: SFG-spectra of CTAB on the water-air-interface after equilibration. Left: pure H_2O (red) 0.01 *mm* CTAB with and without salt (black, blue, respectively), 0.1 and 0.9 *mm* CTAB with salt (green, pink, respectively). Right: same measurements as on the left side and additionally 0.1 and 0.9 *mm* CTAB without NaCl (turquoise, orange). The scale has changed significantly.

The left side of figure 3.8 shows the spectra for pure water, all three measured CTAB concentrations with salt added and 0.01 *mm* CTAB without salt. The signal for pure water (red) is weak compared to the CTAB solutions. No peak in the CH-vibration region can be observed. Upon adding 0.01 *mm* CTAB (black), the water signal above 3000 cm^{-1} rises significantly, though the CH-vibrations are very weak. For the same CTAB concentration with NaCl added (blue), the spectrum changes considerably. The water signal is weaker than in the pure CTAB case, but still stronger than for pure water. Additionally, the peaks of the CH-stretch vibrations are well pronounced. The main features are the symmetric vibration of methylene groups ($CH_{2,ss}$) at 2852 cm^{-1} ,

its Fermi-resonance at 2917 cm^{-1} ($\text{CH}_{ss,Fermi}$), the symmetric stretch vibration of the methyl groups at the end of the molecules hydrophobic tails at 2875 cm^{-1} ($\text{CH}_{3,ss}$), its Fermi-resonance at 2940 cm^{-1} ($\text{CH}_{3,ss,F}$) and the antisymmetric stretch of the same group ($\text{CH}_{3,as}$) at 2960 cm^{-1} . Additionally the symmetric stretch of the methyl groups connected to the hydrophilic head are vibrating at 2985 cm^{-1} ($\text{CH}_{3,ss,head}$).

The spectra of 0.1 and 0.9 *mm* CTAB with salt appear to be almost identical and are only slightly intenser than for the 0.01 *mm* CTAB-NaCl-H₂O-solution.

However, the picture changes dramatically when measuring the CTAB concentrations of 0.1 and 0.9 *mm* without salt added, which is shown in figure 3.8 on the right side. The spectra shown on the left are added on the right again in order to show the strong intensity differences. The water signals above 3000 cm^{-1} have increased significantly. Additionally, the ratio of the two water bands has changed: with salt (left), the signal higher in frequency was slightly stronger than the lower frequency peak. Without the addition of NaCl (right), the lower frequency peak is a lot stronger than the other one. Also a slight shift of the water bands towards lower frequencies can be observed. The CH-signals intensities for both concentrations seem to have increased dramatically as well, though for 0.9 *mm* CTAB they are even stronger than for 0.1 *mm*.

The strong water signal arise from the water molecules that are influenced by the electric field, caused by the surfactants head groups. This field aligns the water molecules, so that the order in the system is increased and the SFG signal rises. Upon adding salt, the electric field is screened due to ion condensation at the interface (see equation 3.2). Here the electric field does not penetrate as deep into the bulk water, so that less water molecules can be aligned.

The change in the intensity ratio of the two water signals comes from differences in the hydrogen-bonding strength. The stronger an H-bond, the lower the signal will appear in an SFG spectrum. For CTAB solutions without salt, the unscreened charge of the surfactants head group leads to stronger hydrogen-bonds within the water network. For further details see chapter 5

Fitting the data can provide deeper insight into the nature of the studied system. For example it could answer the question if without salt added the CH-signals of the CTAB alkyl chain are indeed more intense. This would hint to a higher order of the surfactant at the interface, or alternatively to a higher CTAB concentration at the surface. In this case both amplitudes, of the water- and the alkyl chains-signals obtained by the fit, should increase. On the other hand it is also possible, that the extreme increase of the water bands intensity, together with the red shift of these signals frequencies, lead to an increased interference between the OH- and the CH-stretch vibrations of the water and the CTAB molecules, respectively. In this case, only the amplitude of the OH-groups should increase, whereas the CH-intensities would not change significantly.

In order to address these questions, the data for 0.01, 0.1 and 0.9 *mm* CTAB with, and 0.1 and 0.9 *mm* without salt have been fitted. The fitting result for the low CTAB concentration with salt is shown in figure 3.8 (left) as turquoise, dashed line. For details of the fitting process see chapter 5.

By fitting SFG spectra, three parameters are obtained for every peak: the frequency, the width and the amplitude. The latter is a measure for the number of molecules

contributing to the signal, so the higher the amplitude, the higher the order in the system, or the higher the number of molecules at the interface. The width and the frequency of each peak in the CH-stretch vibrational region are the same for solutions of the same CTAB concentration with and without salt, in order to only see the change of the amplitudes. For the water signals all three parameters, the amplitude, the frequency and the width of the peak were allowed to change, since from figure 3.8 the dramatic changes in all three of them are obvious.

Fitting the data shown in figure 3.8, the amplitudes presented in table 3.1 were obtained. The signs of the amplitudes are used according to literature [64].

Table 3.1: *Amplitudes for each individual peak obtained from fitting the spectra shown in figure 3.8. The indices ss and as indicate the symmetric and antisymmetric stretch vibrations. F and h indicate the Fermi-resonance and the vibration of the head group, respectively. For the OH-stretch vibrations of water, also the width and the amplitude are added.*

Solution	0.01 mM+NaCl	0.1 mM+NaCl	0.1 mM	0.9 mM+NaCl	0.9 mM
CH_{2,ss}	3.6	2.6	2.0	2.4	2.1
CH_{3,ss}	7.1	8.7	3.9	8.8	11.0
CH_{2,ss,F}	10.9	8.9	5.9	7.1	8.4
CH_{3,ss,F}	5.3	14.5	2.1	19.1	11.4
CH_{3,as}	-3.4	-19.7	-1.6	-22.4	-6.1
CH_{3,ss,h}	2.0	13.6	2.5	14.8	1.3
OH₍₁₎	20.5	51.7	342.7	54.5	372.1
Frequ.₍₁₎	3273.3	3282.4	3198.1	3282.4	3200.0
Width₍₁₎	134.0	223.6	329.9	223.6	336.2
OH₍₂₎	22.9	9.8	40.3	10.7	44.8
Frequ.₍₂₎	3356.6	3367.7	3411.7	3367.7	3410.0
Width₍₂₎	122.3	84.4	165.9	84.4	157.5

Comparing the amplitudes for 0.1 mM with, and 0.1 mM without salt, it gets clear that upon adding NaCl the amplitudes for the CH-stretch vibrations are significantly higher than for the same CTAB concentration without salt. However, the huge spectral difference seen in figure 3.8 mainly comes from the strong water signal, as has been explained before.

Additionally, the screening of the charge leads to a closer packing of the surfactant molecules at the water air interface. This leads to two major differences in the obtained amplitudes for 0.1 mM CTAB with and without salt. First, the CH-stretch vibrations get stronger upon adding NaCl. Second, the ratio between the CH_{3,ss} and the CH_{2,ss} (first and second peak) gets bigger. This hints to the fact, that in the case of CTAB with salt less gauche defects are present in the surfactants hydrophobic tail. In a perfect all trans configuration of a surfactant, the only signals visible in SFG would be the CH₃ stretch vibrations, since the CH₂ signals cancel each other out due to their centrosymmetric alignment in the alkyl chain. The lower the amplitude ratio of CH₃/CH₂, the more space the molecules have at the interface and the more gauche defects will be present. The fact, that the ratio for CTAB with salt is higher than for CTAB without salt shows

that the presence of the electrolyte leads to a denser packing at the interface, due to the screening effect mentioned above. This finding is consistent with the drop of the CMC and the equilibrium surface tension with increasing salt concentration, as has been shown in figure 3.4.

When comparing the amplitudes obtained for 0.9 *mm* with, and 0.9 *mm* without additional electrolyte, a similar difference can be observed for the CH-stretch vibrations, though the difference is less pronounced. The major change in spectral shape for the two spectra comes from the huge increase of the water signal, as has been explained before. The fact that the signals of the surfactants hydrophobic tail change less upon adding salt, than for the 0.1 *mm* case, shows that more CTAB molecules are already present at the surface, even without salt added.

The fitting results presented in table 3.1 can be visualised by plotting the fit curves for both CTAB concentrations with and without salt, with the water signals and the non-resonant background removed, so that only the shapes of the CH-stretch vibrations are visible (for details see chapter 5). This is shown in figure 3.9.

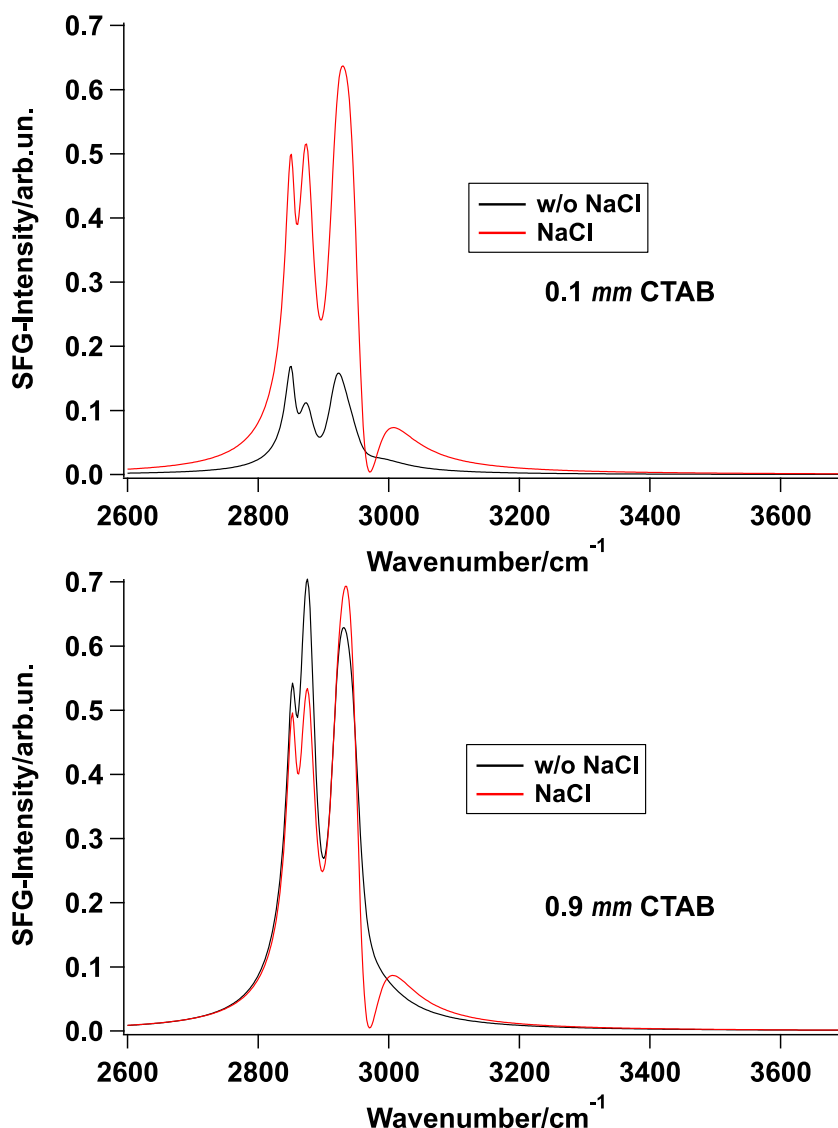


Figure 3.9: Pure CH-spectrum of 0.1 (top) and 0.9 mm CTAB (bottom) with (black) and without NaCl (red). The non-resonant signal and the water peaks have been removed.

The top graph shows the SFG-spectrum of the 0.1 mm CTAB solutions with (black) and without (red) salt added. As can be seen, the addition of electrolyte strongly increases the intensity of the CH-stretch vibration. In the bottom graph, the same is shown for the 0.9 mm CTAB solution. Here, however, only small changes can be observed. This result supports the assumption, that at the higher CTAB concentration, even without the addition of NaCl the surface is already saturated with CTAB molecules, which seems not to be the case for 0.1 mm CTAB.

The analysis of the static spectra shown in figure 3.8 can provide deep insights into the structure of water and CTAB at the water-air interface, as has been shown above. However, the measurements have been taken after the interface had equilibrated. Additionally, the integration time of 10 min is relatively long. Therefore, it is impossible to learn anything

about the dynamics of CTAB at the water-air-interface from these measurements. In order to study the time regime in which the equilibration of the surface occurs, kinetic scans of 20 spectra with one minute integration time have been taken, directly after the solution was filled into the measuring trough. The time between filling the trough and starting the measurement was between 15 and 25 s. This was the time needed to check the signal on the camera and close the lid of the sample box. Figure 3.10 shows the results for 0.01 (top), 0.1 (center) and 0.9 (bottom) mm CTAB with 5.5 m NaCl.

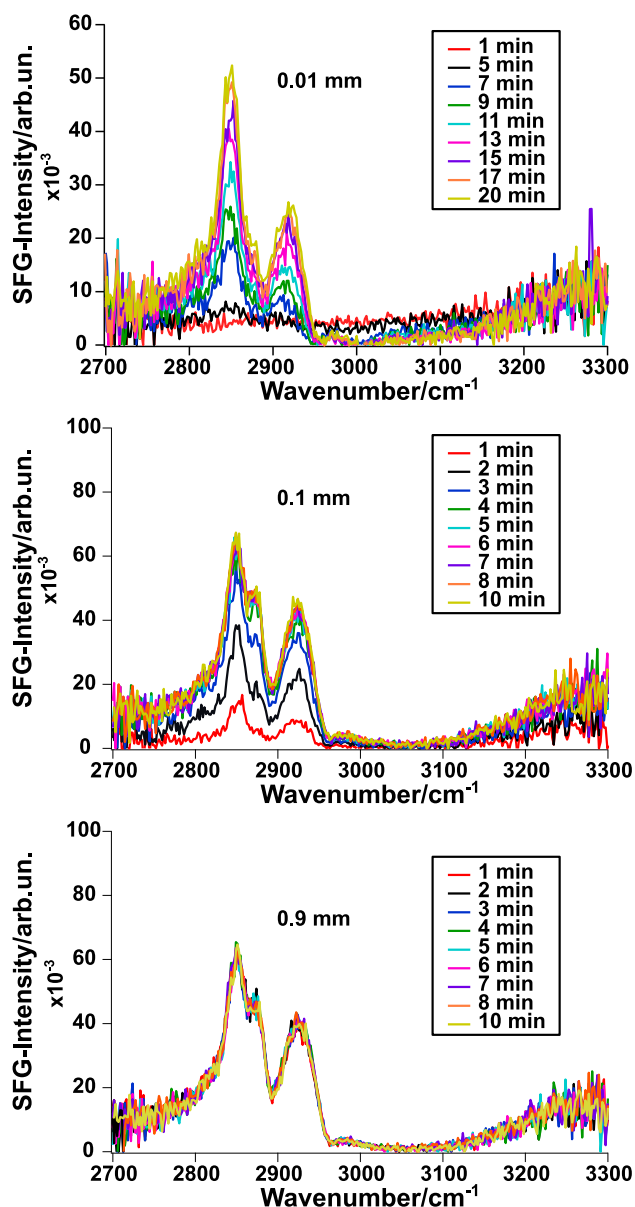


Figure 3.10: Kinetic SFG-spectra of CTAB at the water-air-interface for 0.01 (top), 0.1 (center) and 0.9 mm CTAB with 5.5 m NaCl. Each spectrum was acquired for 1 minute. Note that the top panel has a different y-scale and that the intervals are not of 1 min.

As can clearly be seen in figure 3.10, with increasing CTAB concentration the equilibration time for CTAB adsorbing at the water-air-interface decreases. For the 0.01 *mm* solution the first appearance of CH-stretch peaks can be observed after 5 minutes (black). Note that the time interval for this panels is not one minute. After about 17 minutes (orange) a state close to equilibrium has been reached, since not much difference to the 20 *min* (yellow) spectrum can be observed. In the case of 0.1 *mm* CTAB (center), significant signals of CH-stretch vibrations can be observed already after one minute (red). After four minutes (green) the signals have equilibrated. The solution of 0.9 *mm* CTAB (bottom) does not show any kinetics in the time regime investigated. All peaks have equilibrated after one minute already. These findings are in good agreement to the time dependent surface tension measurements with varying CTAB concentration as shown in figure 3.6. As mentioned before, the surface covering mechanism is based on the number of monomeric surfactant molecules in the solution. The more monomers are in the system, the quicker the surface tension drops.

In order to quantify the time needed for the equilibration of the CTAB-water-air-interface, the spectra for the 0.01 and the 0.1 *mm* CTAB solutions shown in figure 3.10 were fitted. First the latest spectrum after 20 *min* was fitted to get the starting parameters. Subsequently, the obtained parameters were used as starting parameters for the fitting of all other spectra, which then were fitted by keeping all values but the amplitudes constant. In the case of 0.01 *mm* also the non-resonant amplitude was a free parameter. The amplitudes of each individual peak plotted against time is shown in figure 3.11. The spectra obtained for 0.9 *mm* CTAB have not been analysed further, since there is no kinetic effect visible.

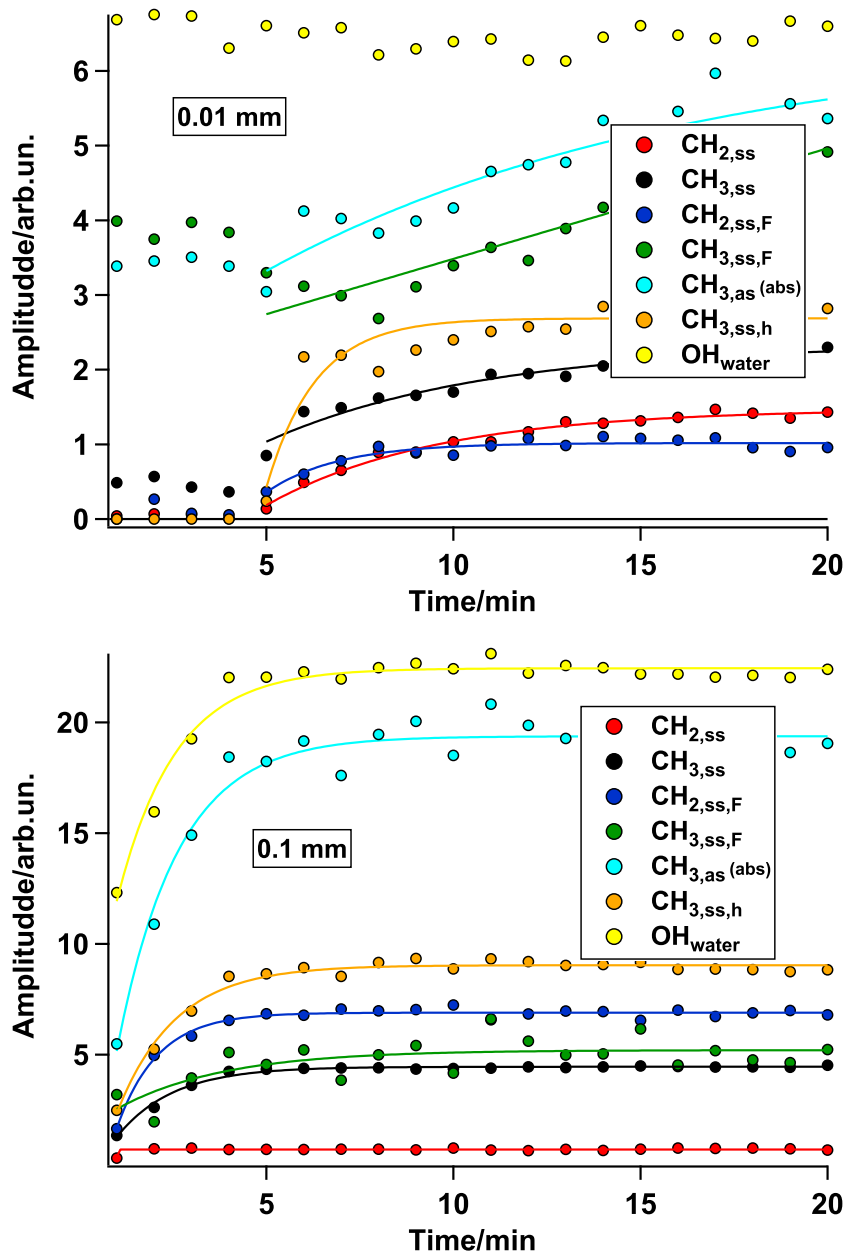


Figure 3.11: Amplitudes obtained by fitting the spectra shown in figure 3.10 for a 0.01 mm (top) and a 0.1 mm (bottom) CTAB solution. The water peaks (yellow) have been scaled by a factor of 0.4 (top) and 0.8 (bottom), due to their high amplitude. The amplitudes for the $CH_{3,as}$ are shown as absolute values, due to the negative sign. The lines are the fits to the individual time traces.

The top panel in figure 3.11 shows the amplitudes obtained from fitting the 0.01 mm CTAB solution. The water signal (yellow) does not change over time. For the $CH_{2,ss}$ (red), the $CH_{3,ss}$ (black), the $CH_{2,ss,F}$ (blue) and the $CH_{3,ss,h}$ (orange) peaks the amplitudes start at very low values. After about five minutes, the signals begin to rise relatively quickly and equilibrate after around 14 minutes. For the $CH_{3,ss,F}$ (green) and the $CH_{3,as}$

(turquoise) the amplitudes start at relatively high levels and start rising only after about eight minutes. The lines shown in figure 3.11 are fits to the time traces, using the following equation:

$$y = y_0 + A \cdot e^{\frac{x-x_0}{\tau}} \quad (3.3)$$

Here y_0 is the starting amplitude, A is a pre-factor, x_0 is the starting time of the rise and τ is the time for the signal to rise. Using a time offset of $x_0 = 5 \text{ min}$, a time constant of $\tau \approx 4 - 5 \text{ min}$ for the first two peaks and $1-2 \text{ min}$ for the third and sixth peak was obtained. For the $\text{CH}_{3,ss,h}$ a time constant of 11 min was obtained by the fit, whereas the time for the $\text{CH}_{3,as}$ peak was unrealistically high. The high initial amplitude for the minutes 1 to 4 of these peaks already shows, that these values are probably due to fitting issues.

The very long initial offset time of 5 min and the time constants of $4-5 \text{ min}$ show that the surface coverage is very slow at this CTAB concentration with salt. Apparently, even at this low concentration, the formation of micelles is a preferred way of reducing the surfactant molecules free energy, resulting in a very low concentration of monomers in the solution. This concentration, however, is decisive for the coverage of the surface. This result fits well to the dynamic surface tension measurements shown in figure 3.6.

The bottom panel of figure 3.11 shows the amplitudes obtained from fitting the 0.1 mm CTAB solution. It gets clear that the increase of the CH-stretch peaks is a lot faster, as was already shown in figure 3.10. All amplitudes have equilibrated latest after 4 minutes. Fitting these data using equation 3.3, without a time offset ($x_0 = 0 \text{ min}$) gives a time constant of about $\tau \approx 1 - 2 \text{ min}$ for all peaks, except for the $\text{CH}_{3,as}$ peak, which gives a time constant of about 3 min and the $\text{CH}_{2,ss}$ peak, that has a τ of less than one minute, which probably is a result of the very low amplitude. Here also the water signal grows in over time, which might come from the fact, that the general intensity of the spectrum is higher, so that the signal is easier to distinguish from the background.

The results of figures 3.10 and 3.11 are in good agreement with the ones shown in figure 3.6, showing that the higher the CTAB concentration, the faster the dynamics of the surface equilibration. It could be shown, that the salt hinders the formation of a monolayer at the interface, probably due to the lower concentration of monomers in the solution. The very slow ingrowth of the CH-signals at the interfacial region, hints to a very slow surface coverage. In this way it could be demonstrated how sum frequency generation spectroscopy can provide molecular insights into the interfacial region of a water-air system including a surfactant and how it can be used as a complementary method to other surface sensitive techniques. The next three chapters will contain the main work done for this thesis, consisting of the attempt to produce TiO_2 thin films, followed by static SFG-experiments on the water-titanium dioxide interface and completed by time resolved SFG-experiments on the same interface.

4 Deposition of TiO₂ Thin Films using RF-Magnetron-Sputtering

In this chapter the deposition of TiO₂ thin films using the RF-magnetron sputtering deposition technique will be discussed. It will be demonstrated how difficult it is to reproducibly coat calcium fluoride windows with thin films of titanium dioxide in the 100 *nm* range.

4.1 The Sputtering Process

Sputter deposition is a widely used technique for the formation of thin films of many different materials and has strong industrial implications for coatings for various applications [65]. It belongs to the group of physical vapor depositions (PVD). There are many different sputter-techniques with various advantages and disadvantages [66]. In general, a target, usually of the material to be deposited, is bombarded with heavy (noble gas-) ions, originating from a low pressure plasma [67,68]. Upon impact, the ions transfer their kinetic energy into the target, causing target atoms or ions to be ejected from the solid material [69]. The free atoms then deposit on a substrate that is usually situated above the target [66].

The most simple technique is the direct current (DC) sputter deposition [66], which is shown schematically in figure 4.1.

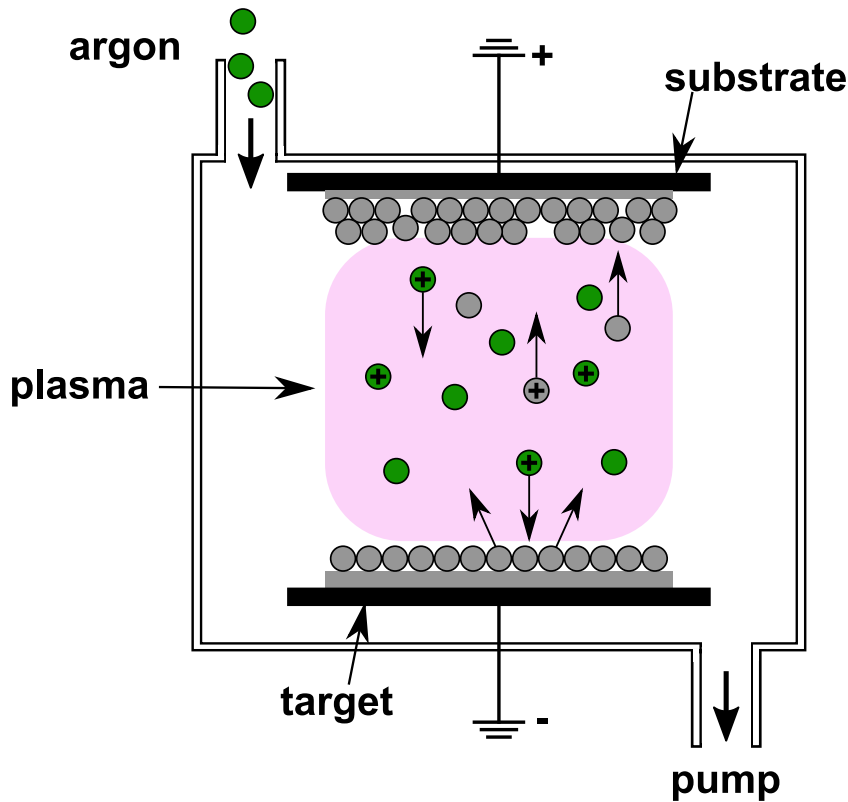


Figure 4.1: Schematic display of the sputter deposition process. The argon atoms (green) are ionised in the plasma (pink background) and accelerated towards the target. Upon impact they eject atoms and ions from the target (grey) which are deposited on the substrate.

Here a strong electric field of several hundreds to thousands of volts is applied between the negatively charged target (cathode) and the positively charged substrate (anode) [70]. Due to impact ionisation in the working gas, mostly argon, a plasma is ignited, containing argon ions and free electrons, which is also called a glow discharge. The voltage accelerates the ions in the direction of the target, where the sputtering process takes place. The advantage of this technique is its simplicity. By only applying a high enough voltage between the target and the substrate [66] the sputtering process can be run. The main disadvantage is the low plasma efficiency, due to the low impact ionisation rate. For this reason the gas pressure has to be relatively high, which has negative impact on the deposition rate and film quality. Additionally, only electrically conducting materials, such as metals can be deposited using this technique. Figure 4.1 shows this process schematically, in order to demonstrate the most fundamental aspects of the sputter deposition process.

In order to overcome the disadvantages, radio frequency (RF) sputter deposition can be used. Here, the plasma igniting electric field is a high frequency field. This field causes the electrons to oscillate with the same frequency, which leads to a higher rate of impact ionisation of argon atoms due to the long electron path [71]. Because of their higher mass, the argon ions cannot follow the field and are accelerated towards the target by an overlying offset voltage. The main advantage of this technique is the possibility

to work at lower pressures than would have been possible using the DC-sputter process, without reducing the sputter rate, due to the higher plasma-rate. Additionally, also insulating materials can be deposited. The main disadvantage is the lower uniformity of the deposited films for larger area substrates, due to irregularities in the plasma. An even more efficient process is the magnetron sputtering technique, which is shown schematically in figure 4.2.

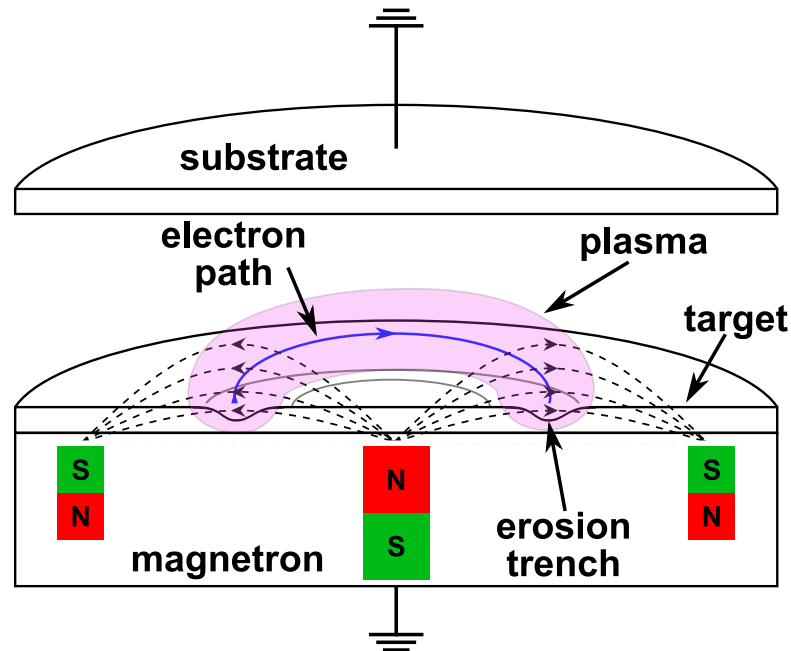


Figure 4.2: Schematic principle of the magnetron sputtering technique. The electron path is shown as blue line, the plasma as pink half torus.

Here an additional magnetic field is applied in the vicinity of the target. This field causes the electrons in the plasma to be forced on a helical path, due to the Lorentz force, shown as blue line. This long path increases the collision rate between the electrons and the argon atoms dramatically, giving a higher plasma (pink half torus) efficiency and deposition rate [72]. The plasma is the strongest where the field lines of the magnetic field are parallel to the target surface. Since the influence of the magnetic field on the ions is very small, their path is not altered and they are accelerated towards the target. The circular shape of the plasma causes a circular erosion pattern on the target, which is typical for the magnetron sputtering process [66]. The main advantage of this technique is that the process pressure can be lowered about 100 times without reducing the deposition rate. If the magnetron is combined with an alternating field it is called RF-magnetron sputtering.

If the target material is not the same as the desired film substance, it is possible to apply reactive sputtering. Here the working gas argon is mixed with a reaction gas, such as oxygen or nitrogen. Due to their ionisation, the molecules of the reaction gas are very reactive and react with the atoms ejected from the target to form a new substance. This technique is mainly used to deposit thin films of metal oxides or nitrides [73]. The mixing ratio of reactive and working gas influences on the thin films stoichiometry and the

sputter rate. However, due to their ionisation the reactive ions are accelerated towards the target, where they can react with the material and be locally implemented into the target material as impurities. This significantly decreases the sputter rate [74].

In the next section a few results of sputter deposition with a commercial reactor will be shown. It will be demonstrated how difficult it is to get reproducible results using this technique. As a result, the TiO_2 thin films used for the rest of this thesis were obtained from external collaborators.

4.2 Sputtering Results

The sputter deposition reactor used for the fabrication of the TiO_2 thin films presented in this section is a commercial BOC Edwards Auto 500, capable of performing depositions using the DC- and RF-magnetron sputtering processes. However, since TiO_2 is a semiconductor, only the RF-magnetron-process could be employed for this work (see above). In this device it was possible to control the working gas flow, the gas mixture (of argon and oxygen) and the sputter power. The latter influences the sputter rate. For a given rate, the running time of the process determines the resulting film thickness. In the chamber a quartz crystal microbalance (QCM) was mounted in order to monitor the thin film growth. The substrate was mounted on a rotating sample holder in order to achieve uniform layers on various samples.

Two different kinds of targets were available, both described as titanium dioxide according to the suppliers. One white and one dark, gray target, which looked quite metallic to the eye. If the latter really was TiO_2 is not known. The colour could hint to the compound Ti(III)-oxide, which is dark violet. Figure 4.3 shows photos of the two different targets used, mounted in the reactor.



Figure 4.3: *Photo of two different targets mounted in the reactor. Both broke after a process. One gray, metallic target is shown on the left. On the right side one white target is shown. After a few depositions this target has partially turned gray.*

Both targets broke during a process. On the left side the gray target is shown, with very deep cracks in the surface. It is possible, that during deposition material of the

underlying layers (indium glue and a copper plate) is also sputtered and deposited on the substrate. On the right side a white target is displayed. It can be seen that it partially turned gray after a few deposition processes. It is possible, that the bombardment with argon atoms preferably ejects the oxygen atoms in the target surface, leaving titanium of different oxidational states than 4+ behind. This issue could partially be overcome using a reactive sputtering process, by mixing oxygen into the working gas.

The reactor chamber was evacuated by a forepump to about 1 *mbar* and the pressure subsequently further reduced by a turbo pump to about $5 \cdot 10^{-5}$ *mbar*. In order to improve the deposition result, different pressures of rest gas have been tested, without significant systematic influence. Upon opening the working gas flow, the pressure increased to a working value of about $5 \cdot 10^{-3}$ *mbar*. The flow of the working gasses was always at 30 *sccm* (standard cubic centimeters per minute) in total. Several different ratios of Ar:O₂ have been employed, ranging from 1:0, over 1:1 up to 1:5. In general the more argon the plasma contains, the higher the sputter rate, due to the atoms higher mass. However, if reactive sputtering is desired, a higher oxygen content is beneficial. It also prevented the white target to turn gray, as explained above.

The sputter process was usually started at a RF-power of 100 *W* and then increased to the desired value. A power of 250 *W* was never exceeded, in order to prevent damage to the reactor. In the first few deposition processes conducted, the power was set to the maximum 250 *W* in order to have a high deposition rate. However, since this procedure did not give reproducible results, the power was reduced down to 100 *W* eventually, without improving the reproducibility of the thin films.

The substrates were cleaned prior to the deposition. For tests, the glass slides were usually rinsed with ethanol and dried with pressurised air. If CaF₂ substrates were used, they were put in an ultra sonic bath in ethanol for 3 *min*, dried with pressurised air and calcinated in an oven (FB1310M-33, Thermo Scientific) at 500 °C for 2 *h*. After cooling down (about 7 *h*) they were mounted in inhouse made aluminium holders (which were also cleaned in an ultra sonic EtOH bath for 3 *min*) and mounted in the vacuum chamber. The evacuation process took about 30 *min*.

The films themselves differed from process to process, without any systematic behaviour, especially in colour and reflectivity. Even in one process it was possible that two samples resulted in optically different TiO₂ layers. The samples came in the colours purple, yellow, green, gray and blueish. Also the sample thickness did not play a significant role, though a tendency could be seen that thinner films appeared to be gray. One of the most astonishing results was the deposition of a green, shiny film of particles, which is shown in figure 4.4.

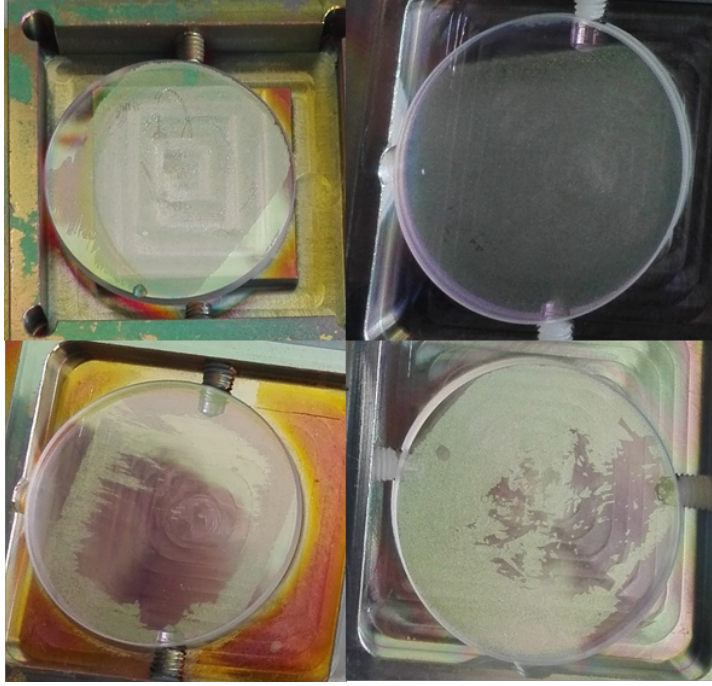


Figure 4.4: *Samples with films of particles deposited.*

The particle film could be blown and washed off using air and water. Underneath the bare CaF_2 window was recovered. However, as can be seen in figure 4.4 not the whole sample was covered with these particles, but parts of the deposition were fixed on the window. The cause for this effect is unknown.

Table 4.1 shows a few results of the investigated sputtering process, ordered by size.

Table 4.1: *Sputter deposition results ordered by film thickness. The columns show the resulting film colour, the deposition power, the working gas mixtures and the rest gas pressure before starting the process. For the first two thicknesses of 5 and 30 nm, two different samples were coloured differently. The 150 nm samples are the ones shown in figure 4.4.*

thickness/ <i>nm</i>	colour	power/ <i>W</i>	working gas/ <i>sccm</i>	restgas/ 10^{-5} <i>mbar</i>
5	purple and colourless	250	30 Ar	-
30	purple and gray	250	30 Ar	6.7
55	purple	150	25 O_2 , 5 Ar	2.7
55	gray	100	25 O_2 , 5 Ar	6.3
80	gray to purple	200	25 O_2 , 5 Ar	6.4
140	yellow to brown	150	25 O_2 , 5 Ar	7.5
150	purple, green particles	150	25 O_2 , 5 Ar	5.6
160	purple	150	25 O_2 , 5 Ar	9.6

As one could imagine, the irreproducibility in the layer colour resulted in irreproducible SFG measurements. Figure 4.5 displays a few SFG measurements on the $\text{TiO}_2\text{-H}_2\text{O}$ -interface conducted on some of the samples presented in table 4.1. Each spectrum was

acquired for 10 min. After subtracting a background signal (10 min acquisition with the IR-beam blocked) the data were normalised to the non-resonant signal of a 100 nm gold reference (60 s acquisition time, background corrected the same way as the sample spectra) that was mounted the same way as the TiO₂-coated window, but not in contact with water (for further details see chapter 5).

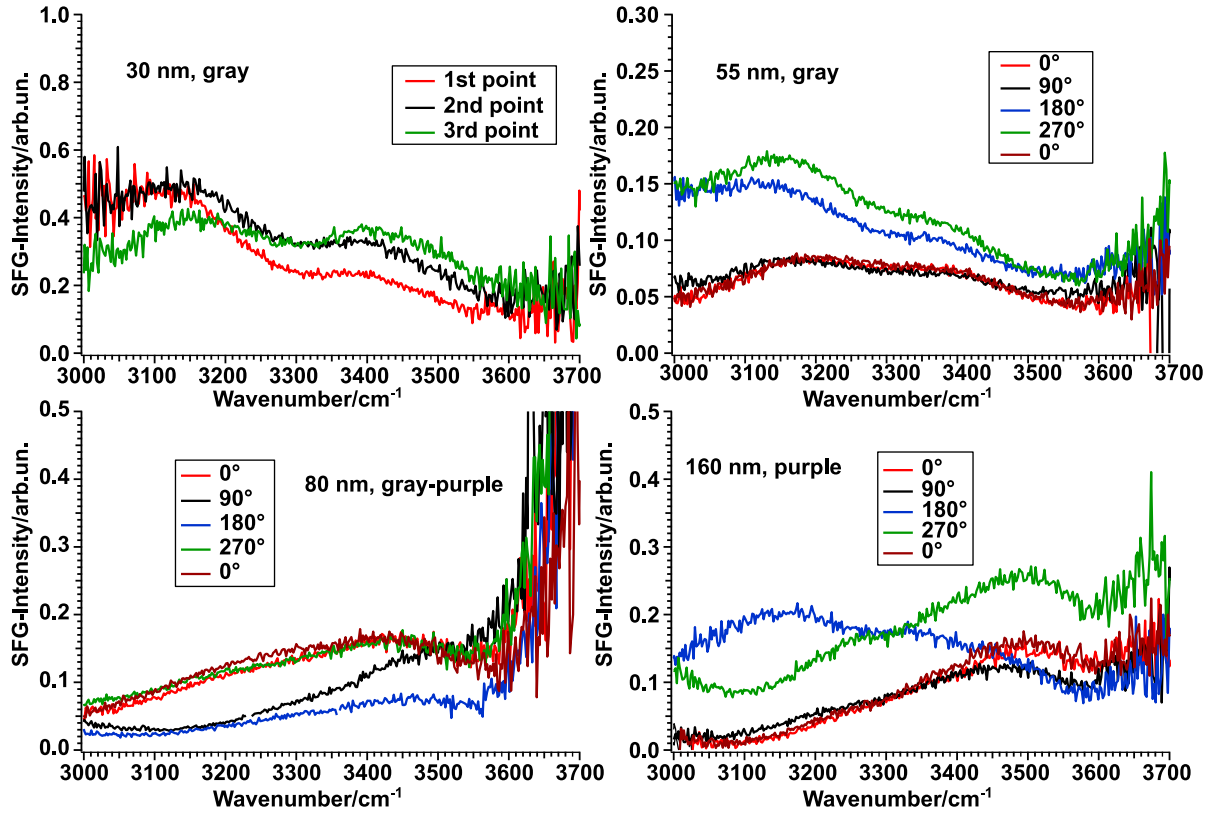


Figure 4.5: *SFG-spectra of the water-TiO₂-interface using samples obtained by sputter deposition. For the 30 nm sample (top left), different spots on the sample were measured. For all other panels the samples were rotated 90°. The 80 nm sample (bottom left) has a background problem.*

The figure shows spectra for four different samples, with the thicknesses 30, 55, 80 and 160 nm, which have been presented in table 4.1. For the 30 nm sample (top left) three different points have been measured by moving the sample stage laterally. For all other samples the sample has been rotated in 90° increments. It gets clear that the spectra show a strong rotational dependence, which might be caused by the use of the rotating substrate holder in the sputtering reactor. Some similarities can be observed, for example the red spectrum of the 30 nm sample looks relatively similar to the green trace (270°) of the 55 nm and the blue spectrum (180°) of the 160 nm sample. However, the rotational dependence of the spectra makes it impossible to learn more about the nature of the water structure at the water titanium dioxide interface, since the peak positions and the amplitude ratios are angle dependent.

4.3 Discussion of Possible Sources of Error

As discussed before, the sputter deposition reactor used for the fabrication of the TiO_2 thin films presented above was a commercial BOC Edwards Auto 500. This reactor was used for many different materials, ranging from pure metals, over alloys up to various kinds of insulators. Therefore the reaction chamber was covered with all kinds of residues. The most often deposited material was indium tin oxide (ITO). Many reactors for scientific or industrial applications are used for only one or a few materials in order to keep the chamber as clean as possible.

Additionally, these reactors possess many controls for all kinds of parameters, such as pressure, gas flow and temperature, which are chosen carefully, since they influence the film quality. With the machine used for this work, however, the only parameters that could be controlled were the gas flow and the sputter power. The pressure could only be influenced by the gas flow and was often relatively unstable during the deposition. The temperature could neither be controlled nor monitored. Also the cooling of the target was not stable, so that its temperature increased in long processes. However, also interruptions of the process for cooling purposes did not influence the sample quality. This lack of control made it very difficult to obtain reproducible results.

For good sputter depositions, the plasma stability is of significant importance. The plasma colour depends mainly on the gas used for the deposition and its pressure [75]. However, using the same deposition parameters several times could result in differently coloured plasmas. The colour ranged from red to green, blue, violet and white. Sometimes it also changed during the process. It is possible that the working gas flows were not very stable, so that the composition and the pressure of the gas changed during the process. Additionally, the colour can also change, when the gas is impure. Possible impurities might have come from particles desorbed from the chamber walls. It is also possible, that with the progress of the process the temperature in the reactor and on the target changed over time, so that more target atoms were ionised in the plasma, causing the colour to change.

The rotational dependence of the spectra, as shown in figure 4.5, is most probably a result of the rotating sample holder in the reactor. The steady rotation in one direction might give a directionality to the thin film, resulting in an angle dependent SFG-response of the water- TiO_2 interface.

In order to progress the project of investigating the water structure at the D_2O - TiO_2 interface, the RF-magnetron sputter depositions have been stopped after more than a year and samples from external collaborators have been obtained. These samples are prepared by using the plasma-enhanced atomic layer deposition (PE-ALD) technique. Taking this step significantly increased the reproducibility of the obtained SFG-spectra. The deposition technique, the results of the SFG-measurements and deeper insights into the structure of water at the water-titanium dioxide interface will be given in chapter 5.

5 pD-Dependent Water Structure at the Water-Titanium Dioxide Interface

This chapter is reproduced from reference [76] with permission from the PCCP Owner Societies.

5.1 Introduction

Since the amount of fossil fuels is finite, cheap and environmentally friendly alternatives are needed. One possible candidate is hydrogen, which can be obtained by photocatalytic splitting of water as was discovered by Honda and Fujishima in 1972 [1]. They were the first ones to observe the evolution of oxygen and hydrogen out of water brought in contact with the semiconductor titanium dioxide under irradiation with UV-light. Since then, TiO_2 has attracted additional attention as a good candidate for the removal of air and water pollutants, or as material for anti wetting coatings [30], as it is cheap, readily available and chemically and thermally inert [28]. There are four crystalline modifications of TiO_2 : rutile, anatase, brookite and riesite, where anatase shows the highest photocatalytic activity [77]. Moreover, the photocatalytic activity depends on the surface facet. For example Lazzeri *et al.* could demonstrate that the (001) facet of anatase single crystals possesses the highest surface energy, which is related to a higher photocatalytic activity [78, 79].

Unfortunately, the efficiency of TiO_2 itself in performing the photocatalytic splitting of water is relatively low. For example the bandgap of the material lies between 3.02 eV for rutile and 3.23 eV for anatase, which corresponds to the range of UV light, whereas the sun's maximum output is in the visible range. Also recombination processes and the high overpotential needed for the hydrogen evolution reaction (HER) turn out to be major obstacles for the applicability of titanium dioxide. Therefore, research on the modification of the semiconductor has been performed with great success, for example lowering the bandgap via doping [80], or building more complex devices to improve the overall performance [28, 81]. However, without understanding the fundamentals of the photocatalytic splitting mechanism, improving the photocatalyst is a time- and resource-intensive process, since it is usually achieved via a trial-and-error approach [28]. As a first step in understanding the photocatalytic splitting of water, research has been devoted to unraveling the water structure at the water- TiO_2 interface [82, 83]. Most of these studies however make use of extreme conditions, such as low temperatures or

ultra high vacuum (UHV) [6], which is far away from normal working conditions for commercially applicable devices.

Theoretical studies have shown that the behavior of water varies with different facets of TiO_2 . For the rutile (110) surface for example, water is believed to adsorb only in an undissociated manner by interacting with the terminal, fivefold coordinated titanium atoms [84, 85]. This is also the case for the anatase (101) facet, whereas for the anatase (001) facet, water adsorbs dissociatively [86]. Though these simulations can give deep insights into the water- TiO_2 interface, they rely on the assumption of a perfect single crystalline structure, which is not realistic for commercially applicable devices. Additionally, it is challenging to simulate different conditions such as varying pH-values or the presence of high amounts of salts. Studying a macroscopic amount of water in contact with TiO_2 experimentally is similarly challenging, as an experimental technique is needed, that only probes the interfacial water layer, but ignores the bulk water present in the system.

A method that fulfills this requirement is Sum-Frequency-Generation (SFG) Spectroscopy. In this technique, a narrowband visible beam of 800 nm wavelength (VIS) and a broadband infrared-beam (IR) are overlapped at the TiO_2 -water interface in space and time. The IR is in resonance with the OD-stretch vibration of the heavy water molecules in the sample used for this study. The narrowband VIS upconverts the excited molecules into a virtual state, from which a photon with the sum of the frequencies of the incoming IR and VIS beams is emitted upon relaxation. Because of its selection rules, the SFG-process is forbidden in centrosymmetric media such as bulk water, making this non-linear mechanism intrinsically surface-specific in the case of liquids [87].

Indeed, it has been shown that the water- TiO_2 interface can be studied in this way under ambient conditions. In 2004, Cremer *et al.* presented data on the TiO_2 - H_2O interface in dependence of the solution pH, for titanium dioxide films deposited on SiO_2 substrates [88]. The very thin layers (0.9 to 3.9 nm thickness) were prepared by chemical vapor deposition, followed by calcination. They have shown that for various pH-values, the SFG-spectra of the TiO_2 - H_2O -interface do not differ significantly from those of the SiO_2 - H_2O -interface.

A combined experimental and theoretical SFG study on a thick film of spin-coated anatase TiO_2 on CaF_2 resulted in the observation of the presence of both chemisorbed and physisorbed water at the titanium dioxide interface [89]. Here we use SFG to study water in contact with amorphous TiO_2 films in the 100 nm range. As the interfacial charge might be important for water splitting, we study the TiO_2 -water interface at different pH-values, introducing positive charges for low and negative charges for high pH, due to interfacial protonation and deprotonation, respectively.

5.2 Experimental Section

5.2.1 Sample

TiO₂ Thin Film Preparation

Thin films of TiO₂ were fabricated in a custom-built plasma-enhanced atomic layer deposition (PE-ALD) system (modularflow, Nümbrecht, Germany), which setup is reported elsewhere [90]. As Ti-precursor, tetrakis(dimethylamido) titanium(IV) (TDMAT) was used which was synthesized according to literature [91]. Optimized feeding sequences were adopted from earlier reported studies with the plasma burning for 200 *ms* [91]. Calcium fluoride windows of 25 *mm* diameter and 2 *mm* thickness (Crystal GmbH, Berlin, Germany) served as substrates. CaF₂ was chosen due to its high transparency for light between 0.13 and 10.5 μm wavelength. The window was cleaned for 3 *min* in an ultrasonic bath in ethanol. After drying with pressurized air, it was placed in an oven at 500 °C for 2 *h* in air. After cooling down, the sample was clamped in a home-made aluminum holder and put into the vacuum chamber of the PE-ALD reactor. The details of the process have been described elsewhere [91]. As the coatings degrade by extensive use, different samples were used in this study. Although the detailed spectral shape varies from sample to sample, the general trend is the same for all samples.

In the current study, we have not heated the deposited layers. The layers have thus an amorphous structure of stoichiometric TiO₂, which was confirmed by x-ray diffraction (XRD) and photoelectron spectroscopy (XPS) [91]. Figure 5.1 displays an AFM picture of a bare CaF₂ (top) window and a TiO₂ layer of 150 *nm* thickness (bottom) on a CaF₂ window of the same kind. Given the 150 *nm* thickness of the film, the CaF₂ is totally covered with the TiO₂ layer.

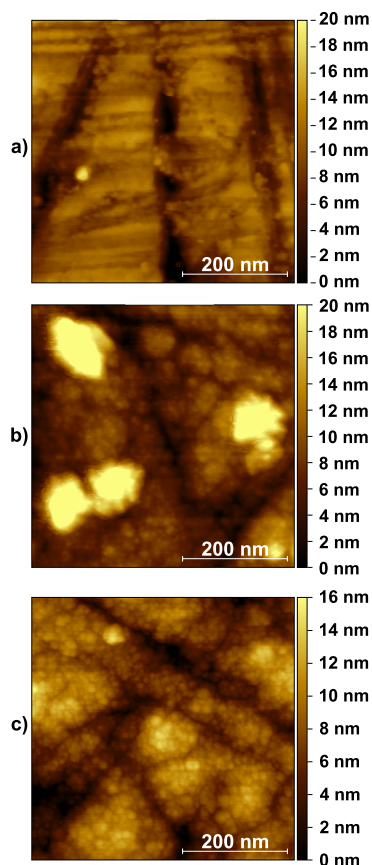


Figure 5.1: $500 \times 500 \text{ nm}^2$ AFM-pictures of a bare CaF_2 window (a) a 85 nm (b) and a 150 nm TiO_2 (c) deposited on a CaF_2 window of the same kind. The surface roughness is 2.6, 4.6 and 2.5 nm for the CaF_2 and the two TiO_2 surfaces, respectively. It can be seen, that the TiO_2 deposition slightly levels off the scratches in the window.

Solutions

To avoid measuring water trapped in the TiO_2 layer and/or at the CaF_2 - TiO_2 -interface, all SFG-experiments are performed in D_2O . This trapped water was observed in an SFG-experiment with D_2O in the cell, while measuring an SFG-signal in the OH-stretch region. Thus all measurements were performed in the OD-stretch vibrational region (ca. $2000 - 2700 \text{ cm}^{-1}$) using D_2O .

D_2O (99.90 %) was purchased from EURISO-TOP GmbH, Saarbrücken, Germany and was used as received for the pD 7 measurements. For pD 11 and 9, NaOH was dissolved (Sigma Aldrich, $\geq 98.5\%$). For pD 3 and 5, HCl was used (Sigma Aldrich, $\geq 37\% \text{ HCl}$). The pD was determined using a pH-meter (Mettler-Toledo).

5.2.2 SFG Experiments

Our SFG setup has been described in detail elsewhere [89]. Briefly, the VIS- and IR-beams are generated using a *fs* Ti-sapphire laser (Libra, Coherent) with an output power of

5 W, a wavelength of 800 nm and a repetition rate of 1 kHz. The pulse duration is about 50 fs. Part of the output beam is narrowed down to a spectral width of about 20 cm^{-1} using an etalon, to give about 30 μJ output energy to be used as the visible beam in the SFG process. The infrared is generated using an automated optical parametric amplifier (TOPAS PRIME, Light Conversion), followed by an NDFG-stage, giving an IR energy of about 8 μJ at around 2400 cm^{-1} , with a full-width-half-maximum (FWHM) of about 300 cm^{-1} .

The VIS and IR beams are focussed and spatially and temporally overlapped on the sample. The angles of incidence are, if not otherwise stated, 69° and 40°, respectively. Before each measurement, the TiO₂ sample and all parts of an in house built sample cell were rinsed with MilliQ water (Millipore Integral 3, 18.2 M Ω) and dried with nitrogen. Afterward, all pieces were treated in an UV-ozone cleaner (FHR UVOH 150 LAB) for 20 min with an oxygen flow of approximately 1 L/min. After the process, the sample was put into the cell, which was then filled with the solution in question. Once sealed, the cell was water- and air-tight.

As schematically depicted in figure 5.2, the measurements were performed by guiding the beams through the CaF₂ window and the TiO₂ layer (shown in orange), onto the D₂O-TiO₂ interface. The SFG beam, obtained in reflection mode, was dispersed using a spectrometer (Andor Shamrock 303i) and detected using a CCD chip (Newton EMCCD-Detector) working at -75 °C.

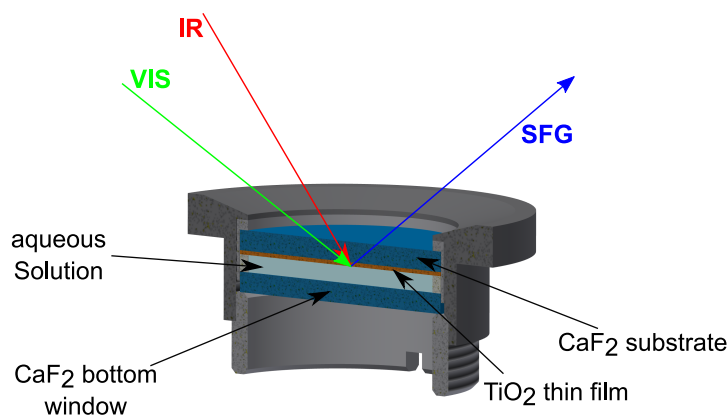


Figure 5.2: *The sample cell including all three beams. The IR and the VIS beams travel through the TiO₂ (orange) coated CaF₂ window and hit the interface of the photocatalyst and the D₂O. The SFG signal is detected in reflection mode and also passes the TiO₂ and the CaF₂ before being sent to the detector.*

Each spectrum was acquired for 10 min. The raw data were background corrected by subtracting a spectrum taken the same way but with the IR-beam blocked. Afterwards, the corrected spectra were normalised to the non-resonant SFG spectrum of a 100 nm gold film also deposited on a CaF₂ window. This step is important in order to correct for the frequency dependence of the gaussian-shaped IR-intensity profile. The gold sample was mounted the same way as the TiO₂ sample, but without water. The acquisition time was 60s. It was also background corrected before normalisation.

For phase-resolved measurements another setup has been used, described elsewhere [89].

5.3 Results and Discussion

Figure 5.3 shows the SFG spectra for D₂O at various pD-values in contact with an 85 nm (a) and a 150 nm (b) thick layer of TiO₂ measured in the OD-stretch vibration region.

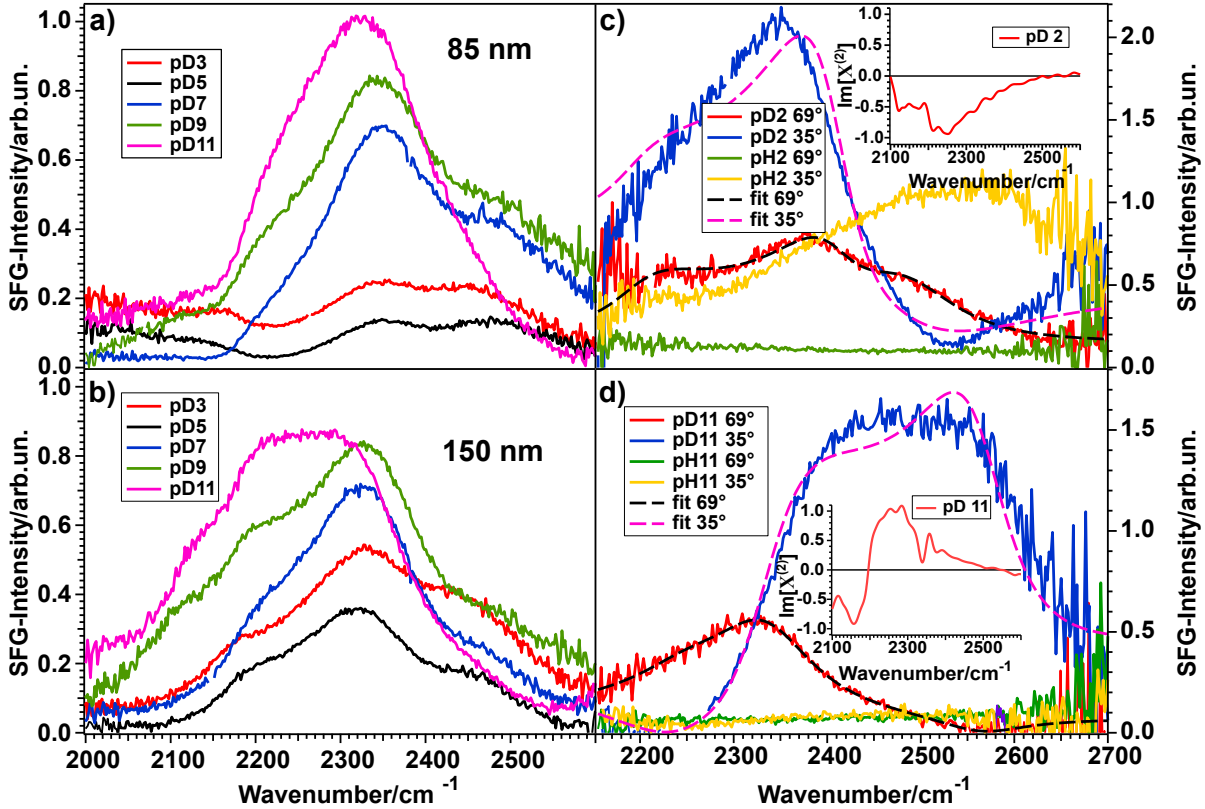


Figure 5.3: *a* and *b*: Spectra for pD 3, 5, 7, 9, and 11 in contact with an 85 nm and a 150 nm thick TiO₂ layer, respectively. *c* and *d*: SFG spectra and fits for pH/pD 2 and pH/pD 11, respectively, in contact with another 150 nm thick TiO₂ sample for two different angles of incidence of the VIS beam, illustrating the influence of the NR signal on the spectral shape. The fits assume a Lorentzian lineshape model [92]. Insets show phase-resolved spectra.

All spectra show three peaks between 2000 and 2600 cm^{-1} , originating from hydrogen-bonded OD-stretch vibrations. For both layer thicknesses, the spectral intensity varies with the pD in such a way, that a minimum at pD 5 (black) can be observed, whereas the intensities rise steadily from 5 to 3 (red) for more acidic and from 5 to 7 (blue), 9 (green) and 11 (pink) for more basic solutions.

As a first approximation, the intensity of an SFG-spectrum depends on the molecular order in the studied system. The non-linear process is only allowed in non-centrosymmetric media, which means, that the SFG-signal scales with the degree of interfacial molecular order. For the data shown in figure 5.3 a) and b), this means that for pD 5 the water molecules are aligned the least and that the order increases when the pD is varied in either direction. The quantification of this finding will be discussed below.

These results stand in contrast to previous data presented by Cremer *et al.* [88], obtained

on very thin (0.9-3.9 *nm*) TiO₂ on SiO₂ substrates. They have shown that for pH 12, 10, 8, 6, and 4, the SFG-spectrum of the TiO₂-H₂O-interface does not differ much from the SiO₂-H₂O-interface. For pH 2 they have seen a bigger signal than for the SiO₂ surface. From their data, they could also show an intensity minimum between pH 4 and 6 for the TiO₂-H₂O-interface. Indeed, the measurement at pH 2 indicates, that there is TiO₂ present at the interface. The similarities between the TiO₂-water and SiO₂-water spectra for all other pH-values measured on the other hand might hint to a major contribution of the SiO₂-H₂O-interface, which also has a strong pH-dependence in the intensity of the SFG-signal [93].

By comparing panel **a)** and **b)** it is clear that for high pD the spectral shape is largely independent of the TiO₂ sample. However, for pD 3 and 5 the spectra differ significantly for the two samples. From comparing several different 85 *nm* and 150 *nm* samples, we conclude that these differences do not originate from the layer thickness itself, since other samples with 150 *nm* layer thickness have shown the same spectral shape for pD 3 and pD 5 as the 85 *nm* sample. Therefore, we attribute the differences to a different non-resonant signal. In general, a non-resonant signal is a contribution to the total SFG-spectrum that is independent of the frequency of the incoming beams. The exact origin of this contribution is rarely known, though it is often considered to be of electronic origin. Since TiO₂ is a semiconductor it is likely that the non-resonant contribution to the signal is influenced by doping or structural defects and varies from sample to sample. That indeed the non-resonant contribution from TiO₂ has a large influence on the SFG-signal is clear from SFG experiments performed with a different angle of incidence for the visible beam. The results are shown in figure 5.3 **c)** and **d)** for pD 2 and 11, respectively. The experiments were performed on a different TiO₂-sample of 150 *nm* thickness. The red spectrum shows the signal for pD 2 and 11 for the same VIS-angle (69° from the surface normal) as for the spectra shown in panels **a)** and **b)**, but from a different sample. The green trace is the non-resonant signal, obtained by exchanging D₂O with H₂O at the same angle and pD/pH. With changing the visible angle of incidence to 35°, the spectral shape of pD 2 and 11 changes dramatically (blue). For pH 2 (**c**, yellow) also the non-resonant signal changes, whereas it is less influenced for pH 11 (**d**, yellow). The non-uniform shape of the non-resonant signal of pH 2 at 35° might arise from the proton band of the H₃O⁺ ions present in the acidic solution [94].

In order to understand the influence of the non-resonant signal on the spectral shape, it is necessary to fit the data from figure 5.3 **c)** and **d)**. In general, the SFG-intensity can be expressed as:

$$I_{\text{SFG}} \propto \left| \chi_{\text{NR}}^{(2)} + \sum_j \chi_j^{(2)} \right|^2 \cdot I_{\text{VIS}} \cdot I_{\text{IR}} \quad (5.1)$$

With I_{VIS} and I_{IR} being the intensities of the visible and the infrared beams, $\chi_j^{(2)}$ as the second-order non-linear susceptibility of the resonance j and $\chi_{\text{NR}}^{(2)}$ being the non-resonant response of the system to the incoming fields.

The details of the water-TiO₂-interaction lie in $\chi^{(2)}$. This factor can be disentangled as:

$$\begin{aligned}
\chi^{(2)} &= \chi_{\text{NR}}^{(2)} + \sum_j \chi_j^{(2)} \\
&= A_0 e^{i\varphi} + \sum_{j=1}^N \frac{A_j}{\omega_{\text{IR}} - \omega_j + i\Gamma_j}
\end{aligned}
\tag{5.2}$$

Here A_0 and φ are the amplitude and the phase of the non-resonant signal, respectively. The resonance is described by the amplitude A_j , the frequency ω_j and the width Γ_j for the j th resonance. As equation 5.2 has a Lorentzian shape, an SFG-spectrum can be described as the sum of one or more Lorentz-functions.

Using this model, the spectra of pD 2 and 11 for a visible angle of 69° shown in figure 5.3 **c)** and **d)** were fitted with three Lorentzians for the resonant part, which is shown in black dashed lines. Upon only changing the non-resonant amplitude and phase, as well as the resonances' amplitudes the spectra for 35° (blue) could be described very well (pink, dashed). These data clearly show that the NR-signal has a large effect on the overall lineshape.

By fitting both datasets we obtained the best description for pD 2 with three peaks at 2150 , 2378 and 2462 cm^{-1} , having a positive, negative and negative sign in the $\text{Im}[\chi^{(2)}]$, respectively. For pD 11 the fit result is a positive, positive and negative sign for the $\text{Im}[\chi^{(2)}]$ for the peaks positioned at 2255 , 2333 and 2564 cm^{-1} , respectively. The peak assignment is given at the end of the manuscript.

A positive sign means that the vibrating molecules' D-atom (more precisely: its transition dipole moment) is pointing towards the semiconductor. This means that for pD 2 most of the water molecules are pointing downwards (with respect to lab frame), away from the TiO_2 layer, whereas for pD 11 most of them are pointing upwards, towards the semiconductor. The insets in figure 5.3 **c)** and **d)** show phase-resolved SFG-spectra of the TiO_2 -water-interface, performed on yet another TiO_2 sample of 150 nm thickness, which confirms the general trend found by the fitting (for more details see below).

To unravel if the three peaks found in the fit originate from three different water ensembles or (partly) from intra- and/or intermolecular coupling, isotopic dilution experiments were performed. For the water-air interface it is well known that intra- and intermolecular coupling results in the splitting of a single peak into two peaks. Diluting the solution isotopically suppresses both these coupling mechanisms, so that the pure resonances are obtained [95, 96]. Figure 5.4 shows the spectra for 100 % D_2O (red) and isotopically diluted solutions (blue) of pD 2 (top) and pD 11 (bottom) in contact with the same 150 nm thick TiO_2 sample as used for the angle-dependent measurements shown in figure 5.3 **c)** and **d)**.

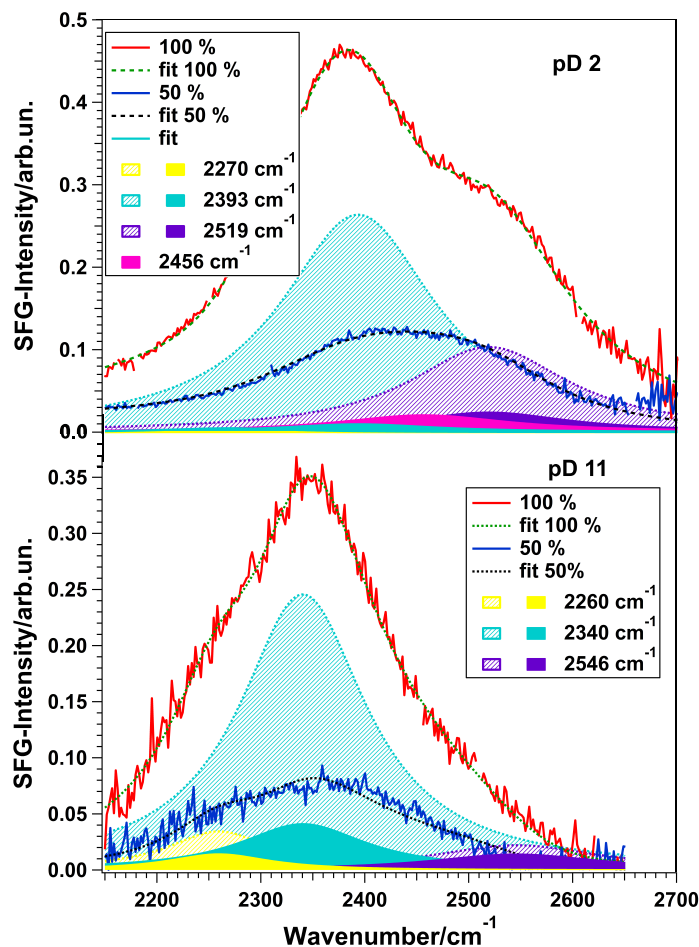


Figure 5.4: SFG-Spectra of 100 % (red) and 50 % D₂O (blue) for pD 2 (top) and pD 11 (bottom). Also shown are the respective fits in dashed green and black lines. All measurements were taken on a 150 nm thick TiO₂ layer. The yellow, turquoise, purple and pink curves show the pure intensity contribution of the corresponding peak.

For 100 % D₂O, the spectra were fitted with three peaks, using equation 5.2 and the sign combinations obtained before. Subsequently, all parameters were kept constant and only the amplitudes were let run free in order to fit the 50 % spectra. To account for possible coupling effects, a fourth peak in the center of two peaks with equal signs was added. Table 5.1 shows the fitting parameters obtained for all four spectra. The assignment of each individual peak to vibrating water species will be given below.

For the pD 11 case table 5.1 shows that the amplitudes A_j (see equation 5.2) for the 50 % D₂O spectra are approximately half the amplitudes of the 100 % D₂O spectra. For a 50:50 mixture of D₂O and H₂O this is an expected outcome if no inter- or intramolecular coupling is involved.

However, in the pD 2 case only the third peak (A_3) has half the amplitude for the 50:50 mixture, whereas the first (A_1) and the central peak (A_2) show approximately a quarter of the initial amplitude. Additionally, in order to adequately describe the data for pD 2, a fourth peak had to be introduced, with a frequency between ω_2 and ω_3 .

In general, if a signal is involved in inter- or intramolecular coupling, it is possible that it splits into two separate peaks. Upon isotopic dilution the two signals merge into one peak with a frequency between the two, which is attributed to HDO molecules [45]. Moreover, the signal amplitude decreases more than linear. For example, for the coupling of two OH-groups, upon isotopic dilution by 50 %, the peaks will decrease to a quarter of the amplitude obtained from 100 % solutions, due to the suppression of the coupling. This is only possible if the two initial signals have the same amplitude sign. In table 5.1 this effect can be seen for the central and the high-frequency peak. For the 50:50 mixture of D₂O and H₂O, the amplitude of the peak at 2393 cm^{-1} (A_2) has dropped to approximately a quarter of the initial value. Additionally, the appearance of the fourth peak at 2456 cm^{-1} , between the central and the third peak, indicates the presence of HDO-molecules.

Table 5.1: Fitting parameters for 50 % and 100 % D₂O solutions of pD 2 and 11, using equation 5.2. A_i is the amplitude of the $Im[\chi^{(2)}]$.

	pD2 100 %	pD2 50 %	pD11 100 %	pD11 50 %
A_{NR}	0.06	0.06	0.04	0.04
ϕ_{NR}	0.45	0.45	2.04	2.04
A_1	5.1	0.8	11.2	7.2
ω_1	2270	2270	2260	2260
Γ_1	150	150	121	121
A_2	-46.4	-8.8	36.9	15.1
ω_2	2393	2393	2340	2340
Γ_2	181	181	149	149
A_3	-30.0	-14.4	-14.8	-11.9
ω_3	2519	2519	2546	2546
Γ_3	187	187	200	200
A_4	-	-14.3	-	-
ω_4	-	2456	-	-
Γ_4	-	200	-	-

However, upon isotopic dilution the amplitude of the peak at 2519 cm^{-1} has dropped only to half of the value for the pure D₂O solution. Therefore it can be concluded, that still a contribution of a molecular species resonating at this frequency, overlapping with the Fermi resonance of the actual 2456 cm^{-1} peak is present. In the case of pD 11 no fourth peak appears, meaning that coupling is weak.

Using the knowledge of the correct amplitude signs and the coupling relations as determined above, equation 5.2 can be used to fit the data shown in figure 5.3 **a)** and **b)**, in order to obtain deeper insights into the nature of water at the water-TiO₂-interface in dependence of the solution pD. Figure 5.5 shows the results of the amplitude (**a, b**) and the frequency (**c, d**) obtained from the fits for the 85 nm and the 150 nm TiO₂ sample, respectively.

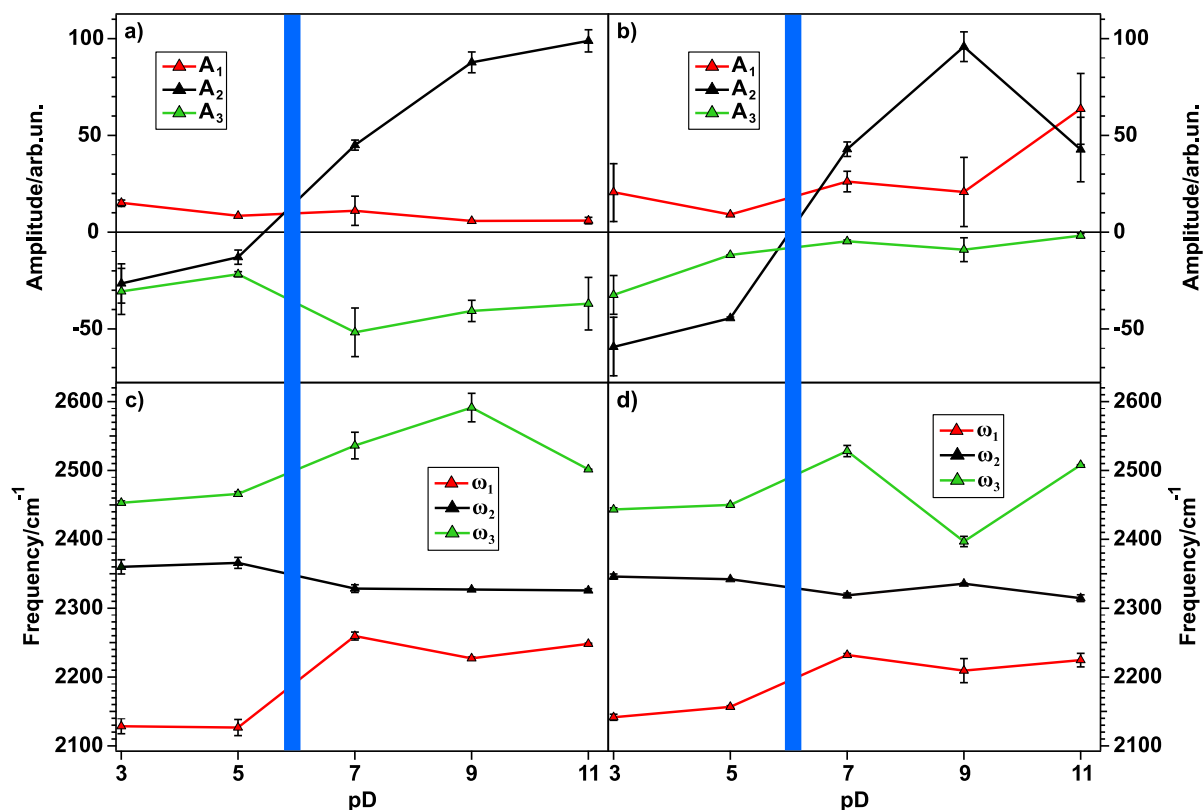


Figure 5.5: *Top: Amplitude (A_j) of each peak obtained from fitting the SFG-spectra, plotted against the pD for the 85 nm (a) and the 150 nm (b) TiO₂-sample. The central peak changes sign upon crossing the point of zero charge at approximately pD 5. Lines connect the data points. Bottom: Central frequency of each of the three peaks for c) 85 and d) 150 nm TiO₂. The blue bar marks the transition from a positively to a negatively charged surface, in order to stress the possible change of molecular species responsible for each peak. The error bars are the standard deviation of the averaged values. The lines connect the data points.*

As explained above, the signs of the amplitudes for the OD-stretch vibrations of water molecules are related to the direction of their dipole moment. A negative amplitude translates for OD to a molecular dipole moment pointing downwards (with respect to lab frame) and therefore away from the TiO₂-interface. For a positive amplitude the dipole moment is pointing upwards in the direction of the semiconductor.

From figure 5.5 it is immediately apparent, that the peak at $\sim 2350 \text{ cm}^{-1}$ changes sign when the pzc is crossed, meaning that the water molecules change their orientation from hydrogen atoms pointing downwards to pointing upwards. For the high- and the low-frequency peaks no sign change occurs, and therefore no reorientation can be observed. The origin of the peaks will be discussed below.

By taking a closer look at the two top panels of figure 5.5, showing the peak amplitudes as a function of the solution pD, an overall intensity minimum for pD 5 can be inferred. In order to better visualize this intensity trend for water at the TiO₂-water-interface for different pD-values, the fits obtained from the spectra in figure 5.3 a) and b) can be used. By setting the non-resonant contribution of the fit result to zero, the purely

resonant spectrum can be obtained. Figure 5.6 shows the square root of the intensity spectrum, integrated between 2000 and 2700 cm^{-1} .

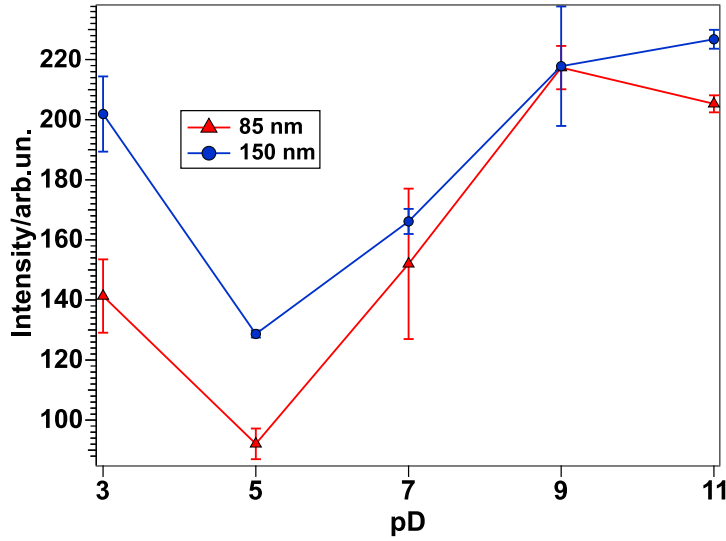


Figure 5.6: Intensities of the square root of the resonant part of the SFG-spectra plotted against the pD. Red triangles show the intensities for the 85 nm TiO_2 layer, blue circles for the 150 nm layer. The intensity shows a minimum at pD 5 for both samples. Lines connect the data points.

The results clearly show a minimum in intensity for pD 5 for both samples, whereas it rises when the solution gets more acidic or basic. Therefore it can be concluded that at pD 5 the water molecules are ordered relatively randomly. For the investigated pD-values, the highest intensity, and therefore the most ordered network, appears at around pD 11. However, in the case of strongly charged interfaces, the higher intensity could also be a result of third-order processes. The charges at the interface result in a DC field reaching into the water and being responsible for the orientation of the water molecules. If this field gets strong enough it can not be neglected and it can interact with the infrared and visible fields to give rise to a third-order response of the water molecules. Therefore, equation 5.1 will change to

$$I_{SFG} \propto \left| E_{VIS} E_{IR} \chi^{(2)} + \int_0^{+\infty} E_{VIS} E_{IR} E_{DC}(z) \chi^{(3)} dz \right|^2 \quad (5.3)$$

with E_{DC} being the strength of the DC field and $\chi^{(3)}$ the third-order susceptibility of the water molecules. This process is allowed in centrosymmetric environments and therefore can influence water molecules up to 1 μm away from the interface. This bulk effect can contribute greatly to, or even overwhelm the $\chi^{(2)}$ signal from the direct interfacial water [97].

To check whether the size of the $\chi^{(3)}$ contribution caused by the strong interfacial charge

is significant, its DC field can be screened by adding excess ions into the solution. For positively charged surfaces, negatively charged ions will be attracted towards the interface, shielding the DC field for lower water layers. The result is the suppression of the $\chi^{(3)}$ contribution to the SFG-signal and therefore a pure $\chi^{(2)}$ signal originating from the water molecules aligned by the surface charge will be obtained. For negatively charged surfaces the same effect can be observed due to the migration of positively charged ions towards the semiconductor. Figure 5.7 shows the spectra taken for yet another 150 nm thick TiO_2 sample in contact with pD 3 and 11 solutions with NaCl concentrations of 0, 10 and 100 mM. The Debye-lengths for these salt concentrations are 9.5, 3.0 and 1.0 nm, respectively [98]. Note, that for 0 mM NaCl an ion concentration of 1 mM has to be considered, due to the presence of HCl/NaOH in the acidic and basic solutions.

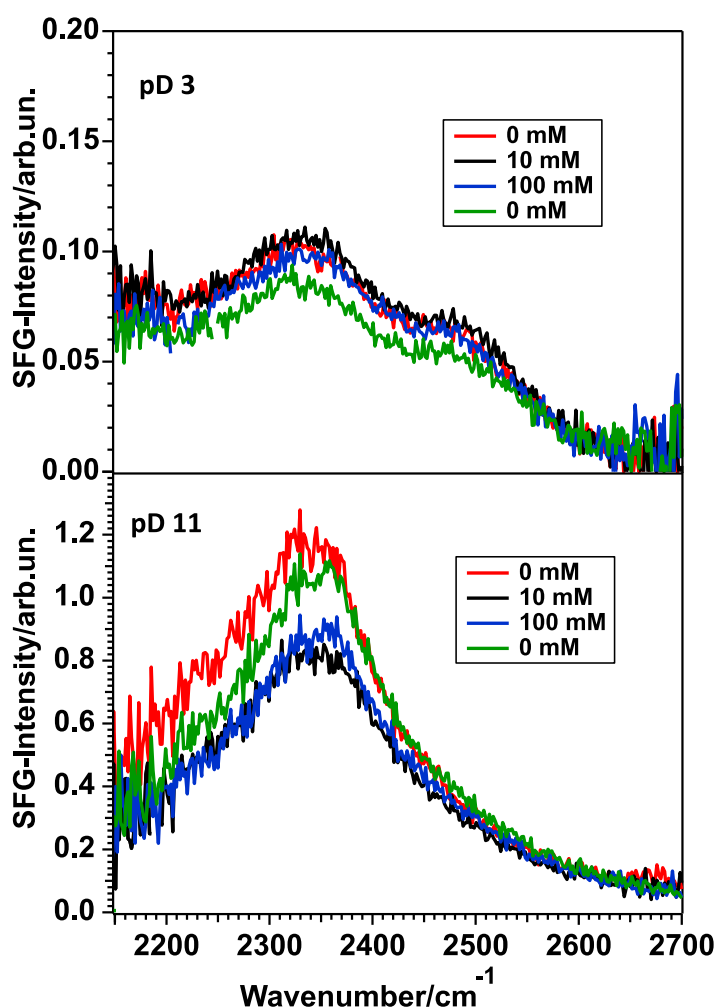


Figure 5.7: SFG-spectra for another 150 nm TiO_2 sample in contact with pD 3 (top) and 11 (bottom) solutions with various NaCl concentrations. The order of the measurements was as shown in the legends, namely 0 (red), 10 (black), 100 (blue) and again 0 mM (green) NaCl.

Figure 5.7 shows that in the case of pD 3 (top), no major change can be observed upon adding salt, demonstrating that the $\chi^{(3)}$ contribution is negligible, despite the relatively

long Debye length of 9.5 nm. For pD 11 (bottom), upon adding 10 mM NaCl, the signal drops by approximately 30 % and stays at that level for the 100 mM solution. When going back to the pD 11 solution without additional NaCl, the signal does not recover fully. We attribute this difference to experimental variations in the signal intensity.

Analysis of the data using the model of Gonella, *et al.* [98] have shown that for pD 11 the $\chi^{(3)}$ contribution at 10 mM NaCl is less than 30 % of the total SFG-signal. Thus, although the surface is charged at high and low pD, the signal originates mainly from the few interfacial layers directly in contact with TiO₂ [97].

The two bottom panels of figure 5.5 show the pD-dependence of the frequency for each peak resulting from the fit. They show that the high- (ω_3 , green) and the low- (ω_1 , red) frequency peaks tend to shift to higher frequencies, whereas the central peak (ω_2 , black) slightly shifts to lower frequencies. Taking into account that especially for the 150 nm film ω_2 has the highest amplitude, its slight shift should result in a relatively big shift of the whole spectrum. This shift clearly can be seen in figure 5.3 a) and b) for both samples.

Both the intensity trends and the spectral shift can be explained by the amphoteric nature of TiO₂. The interfacial protonation state of the semiconductor depends on the solution pD. The material's point of zero charge (pzc) lies at around pD 5. At this pD-value, the protonation and deprotonation reactions occur at the same rate, resulting in a zero net charge of the semiconductor. Therefore, the water molecules will not experience an electric field and are ordered, on average, randomly. With decreasing or increasing the solution pD, the TiO₂ surface is increasingly protonated or deprotonated, respectively. In the acidic, protonated case, the resulting positive charge causes the majority of the water molecules, represented by the peak at $\sim 2350 \text{ cm}^{-1}$, to orient with their deuterium atoms towards the bulk water. For basic solutions the semiconductor is deprotonated and the resulting negative charge orients the majority of the water molecules with the deuterium atoms pointing towards the interface. This means upon crossing the pzc the water molecules flip, as clearly demonstrated by the phase-resolved data – see insets in figure 5.3 c) and d). The higher the interfacial charge, the larger the degree of average water orientation by the resulting electric field, and the higher the intensity of the SFG-signal. The peak position in general is determined by the hydrogen bonding strength of the vibrating OH-groups. The stronger the hydrogen bond of an OH-group is, the lower its oscillation frequency will be due to the weakening of the covalent OD-bond. The observation of decreasing frequency with increasing pD for water at the TiO₂-D₂O interface therefore implies stronger hydrogen bonding for high pD values. However, also the appearance of different water species with different hydrogen bonding environments can cause variations in the spectral shape of an SFG-spectrum, due to their oscillation at different frequencies.

To summarize the findings of peak position and molecular orientation we suggest the following peak assignment: The high-frequency peak, caused by oscillators with a transition dipole moment pointing downwards, accounts for the presence of interfacial TiOD groups, which are relatively isolated, forming weak hydrogen bonds for all measured pD values [89, 99]. These deuterated hydroxyl groups are marked in green in figure 5.8, which illustrates the peak assignment for pD values below, at and above the pzc of TiO₂.

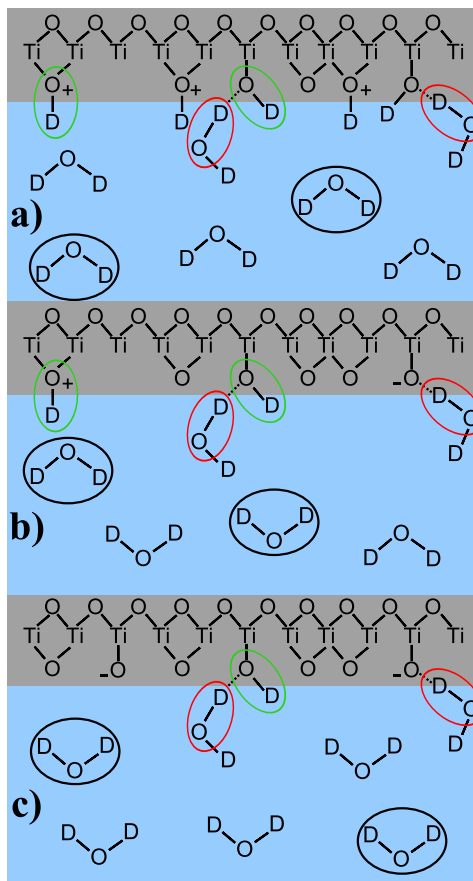


Figure 5.8: Water orientation in dependence of pD, for the acidic (a), the neutral (pzc at pD 5) (b) and the basic (c) case. Circles indicate the peak (green: high-frequency; black: middle-frequency; red: low-frequency). For simplicity the counter ions are omitted.

Considering the shift from lower to higher frequencies upon increasing the solution pD hints to their even stronger isolation when the pzc is crossed. The isotopic dilution experiments for low pD indicated that parts of this high-frequency peak originate from coupling between the OD stretch mode and the bending overtone, complicating the interpretation of this vibrational mode.

Apart from the mentioned TiOD groups, it is possible that TiOD_2^+ and bridging $\text{Ti-OD}^+\text{-Ti}$ groups also exist in the system.

The low-frequency peak originates from molecules pointing upwards, towards the TiO_2 . The low-frequency indicates that these resonators are involved in strong hydrogen bonds. We attribute this peak to water molecules forming hydrogen bonds with the oxygen atom in interfacial TiOD groups, as has been shown before [89]. At high pD, it is also possible that deprotonated TiO^- groups are involved in strong hydrogen bonding. These deuterated hydroxyl species' are marked red in figure 5.8.

The central peak changes sign upon crossing the point of zero charge. Accordingly, it is assigned to water molecules in underlying layers of D_2O very close to the surface, i.e. most likely in the first two water layers, as the $\chi^{(3)}$ contribution is very small. These molecules are strongly influenced by the surface charge and marked in black in figure 5.8.

For a protonated, positively charged interface at low pD, the molecules are pointing away from the TiO_2 . In the deprotonated case at high pD their deuterium atoms are facing towards the negatively charged semiconductor. The weak frequency shift allows the assumption that their bonding environment does not change dramatically, meaning that they most probably form hydrogen bonds to other water molecules. As for low pD, this peak is also involved in the coupling with an overtone of the D-O-D bending mode, its frequency should be considered to be slightly higher than obtained from the fit. In our previous work on anatase TiO_2 this central peak was absent, as that work was performed with water at neutral pH and no additional electrolytes. Thus, the system was close to the point of zero charge [89].

6 Dynamics of the D₂O-TiO₂-Interface

In chapter 5, the structure of water at the D₂O-TiO₂ interface has been investigated using static SFG-spectroscopic measurements. This tool is ideal for determining the orientation of water molecules and their interaction with the semiconductor, which in turn can have a significant impact on understanding the photocatalytic conversion of the sun's energy into hydrogen. However, these measurements were averaged for several minutes, only giving the mean response of the equilibrated interface. A chemical reaction, on the other hand, is a highly unequilibrated process, involving not only the transfer of atoms, functional groups or electrons, but also of energy. Additionally, the transfer of energy from one molecule to another is an extremely fast event that occurs on the order of femto- to picoseconds. Therefore static SFG spectroscopy cannot provide insights into this time window. In order to study processes occurring on the timescale of femtoseconds, such as the dissipation or transfer of vibrational energy, SFG can be extended by adding a narrowband pump pulse that excites a subset of water molecules at the interface. The fundamentals of this pump-probe SFG technique have been described in section 2.3.

In this chapter, pump-probe SFG measurements on the water-titanium dioxide interface for pD 3, 7, and 11 will be discussed. Additionally, the time-dependent SFG response of the interface with isotopically diluted solutions will be presented. Information is obtained about coupling effects and the hydrogen bonding interaction between the water molecules specifically at the TiO₂-D₂O interface and how this hydrogen bonding network is influenced by the surface charge of the semiconductor.

6.1 Introduction

Ultrafast pump-probe techniques have been widely used to get insights into dynamical processes on a broad range of systems and timescales, usually in the femto- to picosecond range. The applications range from the observation of solvation processes or reactions in photochemistry, to the investigation of charge carrier transport in semiconductors or the dissipation of energy [100]. As all these processes involve different sample systems as well as different physical and chemical phenomena, it is clear that also a wide variety of pump-probe techniques must exist. The differences usually involve different frequencies for the applied spectroscopic systems, depending on the question the experimentalists want to answer. For studying the dynamics of charge carriers in semiconductors, for example, electron-hole pairs are usually generated using a UV- or visible laser beam to excite the sample. In order to probe the migration of electrons and/or holes in the material, terahertz radiation can be used, since it is in resonance with the intraband transitions of charge carriers [101]. It is also possible to make use of visible light in order to observe the

dynamic behaviour of the light absorption of materials when they are optically excited into an excited electronic state. This so called transient absorption experiment involves processes like excited state absorption or ground state bleach [102]. Another interesting way of performing transient absorption experiments is by vibrationally exciting the system using an IR pump-pulse and probing the response with another IR- (2D-IR) or a visible probe-pulse, in order to study the absorption behaviour of vibrationally excited states [103].

What these tools have in common is the general method of measurement. The sample is first excited by a pump laser pulse, be it an electronic (UV/VIS) or a vibrational (IR/THz) excitation, in order to perturb the system, that initially is in an equilibrated state. After a defined delay time in the range of femto- to picoseconds, the probe pulse(s) interact(s) with the unequilibrated sample, giving a response that deviates from the unperturbed one. After the excitation with increasing delay time between the pump and the probe laser pulses, the disturbance induced by the pump pulse is reduced, for example, due to the relaxation of the excited molecules back to the ground state. In this way, it is not only possible to obtain information about the timescales of relaxation processes, but also about the relaxation mechanisms.

For this work, in order to study the dynamics of transfer and dissipation of vibrational energy in water at the $\text{TiO}_2\text{-D}_2\text{O}$ interface, a subset of water molecules is first excited by a narrowband IR pump pulse in the hydrogen-bonded OD-stretch vibrational region. After a time delay τ , the narrowband VIS and the broadband IR probe pulses probe the water molecules at the interface, using the SFG process. Due to the prior pump excitation, fewer water molecules can contribute to the SFG signal, which results in a reduced intensity [104]. This process is called spectral hole burning, which is shown schematically in figure 6.1.

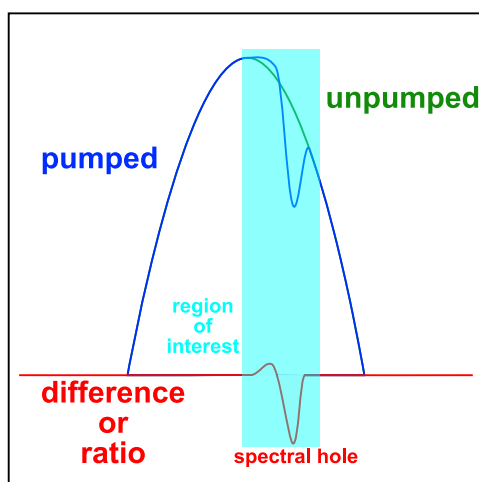


Figure 6.1: Schematic display of pump pulse induced spectral hole burning. The unpumped spectrum (green) has the shape of the normal, static SFG spectrum. The pumped spectrum (blue) is disturbed by the pump pulse, here shown as a strong reduction at higher and weak increase at lower frequencies. Calculating the difference (or ratio) of the two spectra (red) facilitates the visualization of the perturbation.

If the delay time is very large (on the order of nanoseconds), all the energy pumped into the system has been distributed between the water molecules and therefore only heat effects can be observed because the molecules are back in the unperturbed ground state. Since the time-dependent response of the system to the pump pulse can be very subtle, it is easier to detect if a pumped and an unpumped spectrum are taken directly after each other, which also compensates for long term laser fluctuations. To do so, a chopper blocks every second pump-pulse, so that pumped and unpumped spectra can be recorded in an alternating manner, with a vibrating mirror separating the two signals on the camera. To better visualize the time dependence, the difference or ratio of the spectra in presence and absence of the pump pulse are typically considered. If the interest lies in the relaxation behaviour of only a subset of molecules, a narrow region of interest is chosen (turquoise in figure 6.1). Now repeating the dividing (subtraction) process for every time step and plotting the ratio (difference) against the delay time results in a time trace, typical for IR-pump SFG-probe measurements. The technical details have been explained in section 2.4 and shown schematically in figure 2.6. Figure 6.2 shows an exemplary time trace, as can be obtained by the method explained.

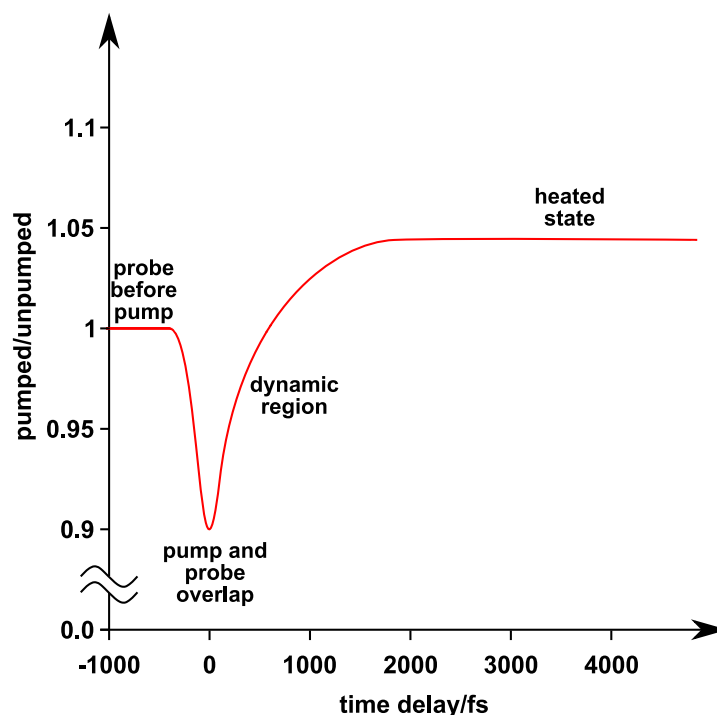


Figure 6.2: Schematic display of a time trace obtained by pump-probe-SFG.

At negative times, the probe pulses reach the sample before the pump pulse, so that the "pumped" spectrum is the same as the unpumped one. Therefore the ratio is one. As soon as the beams start to overlap in time, the intensity of the pumped spectrum is reduced, due to spectral hole burning, as has been shown in figure 6.1. At time zero the overlap of the pump- and the probe-pulses is at its maximum, leading to a local minimum in the time trace. After the overlap, the system relaxes, for example by dissipation or

transfer of the vibrational energy through coupling mechanisms. This dynamic region in the time trace contains the desired information, since the pathway also defines the relaxation dynamics.

After longer delay times on the order of picoseconds, it is possible to see a finite difference between the pumped and the unpumped spectrum, that lasts over tens of picoseconds. In this region, the pumped spectrum shows a heated state of the system as a result of the high energy input [45]. In many cases, if two spectra of water taken at different temperatures are compared, the spectrum of the warmer system shows an overall weaker intensity and a significant blue shift, due to the decrease of order in the system and the weakening of hydrogen bonds, respectively. As a result, at higher frequencies, the ratio between the heated and the unheated spectrum will be larger than one, whereas, at lower frequencies, the ratio will be below one. Therefore, in the time trace, the response of the heated state might look very different, depending on the region of interest, which is the frequency range integrated for constructing the time trace. This is shown in figure 6.1 as a turquoise, transparent bar. The region of interest is usually chosen according to the pump-frequency, so that the direct influence of the pump-pulse on the pumped water molecules can be observed. Figure 6.3 (left) shows two spectra taken at the D_2O - TiO_2 -interface with a solution of pD 11 at room temperature ($23\text{ }^\circ C$, blue) and at $40\text{ }^\circ C$ (red), as well as the ratio of the heated divided by the unheated spectrum (right).

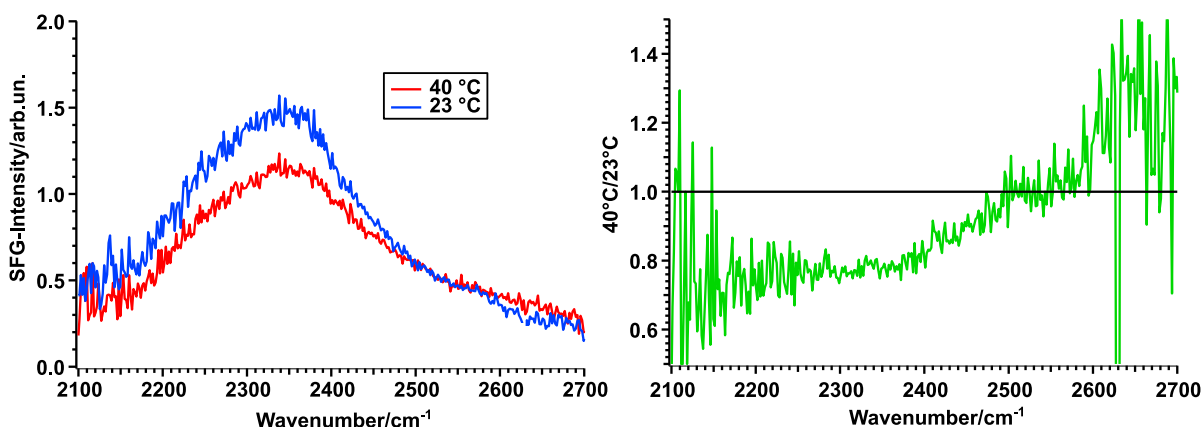


Figure 6.3: *Left: Spectra taken at room temperature (blue) and at $40\text{ }^\circ C$ (red). The heated spectrum shows lower intensity in the lower frequency region, but higher intensity in the higher frequency region. This is a sign of the weakening of the hydrogen-bonding network. Right: Ratio between the heated and the unheated spectra.*

The heat effect can already be seen in the spectra in the left panel of figure 6.3. A significant decrease in intensity can be seen for the $40\text{ }^\circ C$ spectrum in the lower frequency region, whereas it shows a higher signal at higher frequencies. If the high-temperature spectrum is divided by the low-temperature spectrum, the green plot on the right panel of figure 6.3 is obtained. This analysis clearly shows that depending on the region that is chosen for constructing the time trace, the result for longer time scales might look very different if the pumped spectrum shows a significant heat effect. As long as the

pump pulse is in resonance with any OD-stretch vibration of the water, the specific pump-frequency does not change the outcome of the heating effect.

It has been mentioned several times that, in order to properly visualise the influence of the pump-pulse on the water system, the frequency region of interest is chosen according to the pump-frequency. However, additional information can be obtained by analysing the behaviour of the cross-peak, which means pumping at a specific frequency, but plotting the time trace for a water peak that is not directly influenced by the pump. The appearance of cross-peaks is a hint for the coupling of two different vibrations. There are two possible mechanisms. First, if one vibration is excited, the vibrational energy can be transferred back and forth between the two oscillators in a Förster energy transfer-like manner. However, the energy-transfer takes time, so that a time delay between the direct and the cross peak should be observed, which is shorter for a stronger coupling. Also, a transfer from a lower to a higher frequency mode is less likely to occur since the energy mismatch would have to be collected from the surrounding environment [45]. A second possibility is that the excitation of one mode leads to a frequency shift of another one [105]. This process could happen instantaneously since the two vibrations are coupled without a direct energy transfer. In any case, the stronger the coupling between the two vibrations, the stronger the response of the cross peak to the pump-pulse. In this way, the analysis of possible cross-peaks gives further insights into the coupling of states, and therefore into further possible energy transfer mechanisms in interfacial water.

In the next section, pump-probe SFG-data of the D_2O - TiO_2 -interface will be presented for solutions with pD 3, 7 and 11. It will be shown how the time scales are obtained by using the four-level-model presented in chapter 2 and how the relaxation dynamics depend on the interfacial protonation state of the semiconductor.

6.2 Time-Resolved SFG-Spectra of the TiO₂-D₂O-Interface

6.2.1 Pump-Frequency of 2550 cm⁻¹

Figure 6.4 shows the ratio of pumped and unpumped spectra for several time delay points recorded at the interface of TiO₂ in contact with solutions of pD 3 (left), 7 (center) and 11 (right). The TiO₂ sample of 150 nm thickness shows similar static SFG-spectra as have been presented in chapter 5. The pump-frequency was centered around 2550 cm⁻¹, with a spectral width of about 100 cm⁻¹. The ionic strength for pD 3 and 11 was the same, for pD 7 no salt was added. As has been shown in chapter 5 the effects of salts on the SFG-spectra of the D₂O-TiO₂-interface are minor.

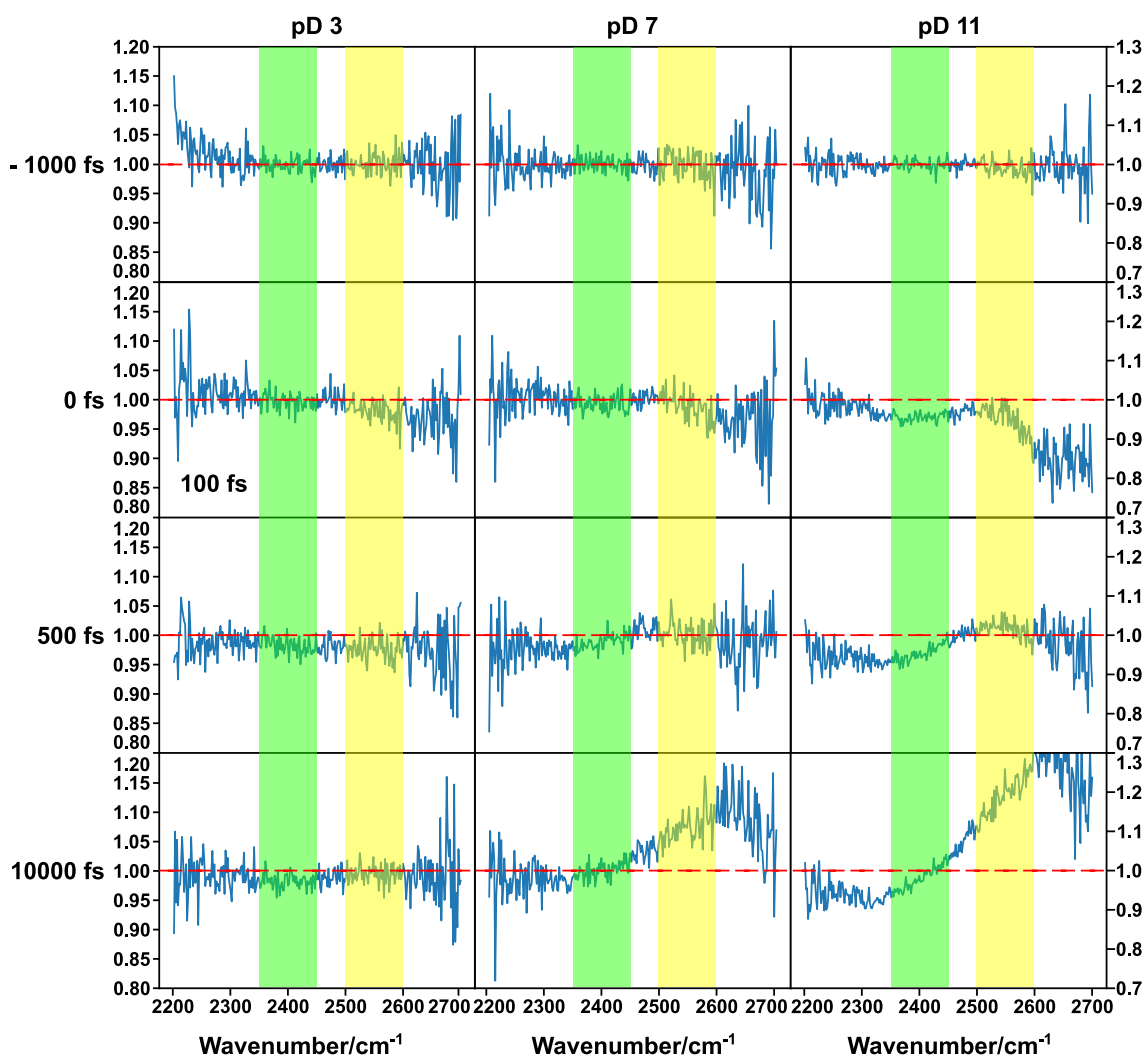


Figure 6.4: Ratio of pumped/unpumped SFG-spectra of water with pD 3 (left), 7 (center) and 11 (right) in contact with TiO₂ for -1000, 0, 500 and 10000 fs (top to bottom), pumped at 2550 cm⁻¹. For pD 3 not the ratio at 0 but at 100 fs is shown. The smaller, left axis belongs to pD3, the right axis to pD 7 and 11.

Note that the scale of pD 3 (left axis) is smaller than for pD 7 and 11 (right axis), since the effects described below are less pronounced at low pD. As indicated on the left side of figure 6.4, the time points shown are -1000, 0, 500 and 10000 *fs* from top to bottom, except for pD 3, where not 0 but 100 *fs* is shown, due to experimental uncertainties in the delay time (marked by the inset in the second row).

For all three pD values, at negative times (-1000 *fs*, top row) the ratio of the pumped divided by the unpumped SFG-spectrum lies around 1 for all frequencies (red dashed line). Since at this time point the pump pulse reaches the sample after the SFG-probe-pulses, no perturbation by the pump-pulse has occurred yet. Therefore a ratio of 1 is to be expected.

At 0 *fs* (100 *fs* for pD 3, second row) delay time, a clear drop in the ratio can be seen above 2550 cm^{-1} (yellow transparent bar) for all three pD values. The higher the pD-value, the more pronounced it appears. This effect is due to the spectral hole burning from the pump-pulse at 2550 cm^{-1} , as has been explained in section 6.1. Why this spectral hole burning effect occurs mainly at frequencies above 2550 cm^{-1} and not centered around the pump frequency will be discussed below. Additionally, for pD 11 a second drop in intensity at around 2400 cm^{-1} can be observed at 0 *fs* (green transparent bar). The origin of this effect will be discussed below as well.

After 500 *fs* delay time the drop of the pumped/unpumped ratio at 2550 cm^{-1} has disappeared for all pD values. In the case of pD 11 (right), it has changed into a small increase in the ratio above one. The drop at 2400 cm^{-1} on the other hand has decreased further and is more pronounced at this delay time. It also has appeared in the signals of pD 7 (center) but is not visible for solutions of pD 3 (left).

10000 *fs* after the arrival of the pump pulse at the sample, in the cases of pD 7 and 11 the ratio between pumped and unpumped SFG-spectra is dominated by the heat effect, as has been demonstrated in figure 6.3. At lower frequencies, the ratio is smaller than 1, whereas at higher frequencies it is clearly above 1. In the pD 3 case, no significant heat effect can be observed, so that the ratio is around 1.

In order to properly visualise and quantify the pump-pulse-induced changes in the SFG-spectrum for each time point observed, it is useful to integrate over the spectral region of the pump-pulse at 2500-2600 cm^{-1} and plot the ratio of each point against the delay-time, as has been demonstrated in section 6.1. The result for pD 3, 7 and 11 is shown in figure 6.5.

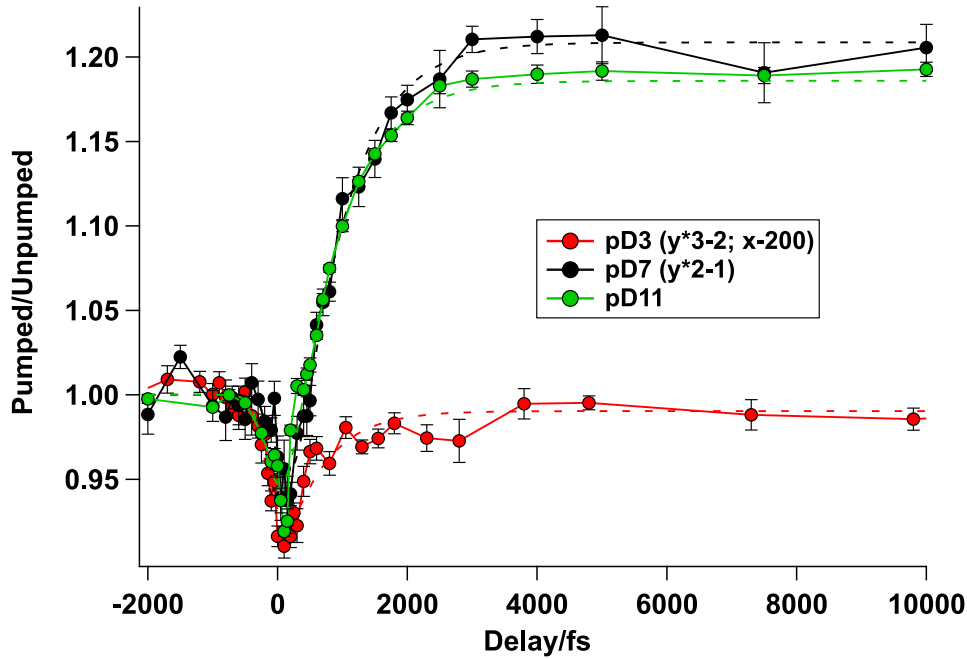


Figure 6.5: Time traces of the $\text{TiO}_2\text{-D}_2\text{O}$ -interface with pD 3 (red), 7 (black) and 11 (green), pumped at 2550 cm^{-1} , integrated between 2500 and 2600 cm^{-1} . The graphs of pD 3 and 7 have been scaled according to the notes in the legend. Dashed lines are the corresponding fits.

To compare the different traces, the time traces for pD 3 and 7 have been scaled by factors of 3 and 2, respectively. In order to have the points at negative delay times start around 1, all points also have been subtracted by 2 and 1, respectively. The trace of pD 3 additionally has been shifted on the x-axis by -200 fs , which is justified by experimental uncertainties in time zero. The measurements shown in figure 6.5 are averages of 6, 7 and 8 recorded time traces for pD 3, 7 and 11, respectively. they are highly reproducible, though for pD 3 the ratio of pumped and unpumped spectrum could be slightly more or less than 1 for long timescales. This small irreproducibility is attributed to experimental uncertainty. After the scaling, the traces for pD 7 and 11 are very similar in their details. All three time traces in figure 6.5 show the same trend of an intensity reduction of the pumped spectrum around time zero, followed by an increase of the intensity. The intensity drop is a result of the perturbation by the pump pulse, which partially depletes the ground state of the system, resulting in a lower SFG intensity in the pumped spectrum. The maximum perturbation occurs at around 0 fs , from which point on the pump pulses' influence gets weaker, and the system relaxes back into its (heated) equilibrium state, resulting in the aforementioned increase of intensity of the pumped spectrum. This spectral hole burning process results in the typical shape of the time trace, as has been demonstrated in section 6.1.

However, for pD 7 and 11, the time traces rise well above 1 for delay times longer than 1000 fs . In figure 6.4 it already has been demonstrated, that after 500 fs the ratio between pumped and unpumped has returned to around 1 (third row). After this time, the pumped spectrum is dominated by heat effects due to the energy deposited into the

system by the pump-pulse. This results in the high pumped/unpumped ratio for higher frequencies.

For pD 3, the ratio is slightly lower than 1 at long time scales. Here the heat effect seems to behave differently than for pD 7 and 11. However, other pD 3 experiments also have shown ratios at or slightly above 1 for delay times beyond 1000 *fs*. Due to the apparently relatively low influence of the pump-pulse on the water molecules in a solution of pD 3, the endpoint of the heat effect might be prone to experimental fluctuations. Heating experiments as demonstrated for pD 11 in figure 6.3 conducted using solutions of pD 3 and 7 have shown similar effects, though the experiments with pD 3 (below the pzc at pD 5, see chapter 5) show a smaller effect than the experiments with solutions above the pzc. Remember that here the data have been scaled in order to make the time traces comparable.

A possible explanation to the different heat effects for different pD-values could be, that the interfacial molecules at a pD-value above the pzc show a higher IR-absorption behaviour at 2550 cm^{-1} , resulting in a stronger heated spectrum. However, due to the fact, that the SFG-signals of water molecules at the $\text{D}_2\text{O-TiO}_2$ interface at lower pD-values generally appear at higher frequencies (see chapter 5), this effect is counter-intuitive.

Another explanation could include the generally stronger hydrogen-bonding network for higher than for lower pD values, as has also been discussed in chapter 5. As explained in section 6.1, the heating of the system leads to weaker hydrogen bonds between the water molecules, which results in a blue shift of the SFG spectrum. Due to the fact that for pD 3 the highest contribution to the SFG-signal comes from water molecules that are not in direct contact with TiO_2 and therefore form hydrogen bonds to other water molecules, it is possible that the effect of the heating of the system is less pronounced. For pD values above the pzc, at which the majority of water molecules are pointing towards the semiconductor and forming strong hydrogen bonds with it, the heat might disturb the whole D-bonding network a lot more.

A closer look at figure 6.4 reveals that the pump-pulse also has an effect on molecules that vibrate with frequencies different than 2550 cm^{-1} , as has been pointed out above. Especially for pD 11 (right) at around 2400 cm^{-1} a clear immediate (0 fs) drop of the pumped/unpumped ratio can be observed (green transparent bar). Going the same way as for figure 6.5 but integrating over the frequency range of $2350\text{-}2450\text{ cm}^{-1}$ (see green transparent bar in figure 6.4) and plotting the ratio for each time step against the delay time, the time traces for the so-called cross peaks, shown in figure 6.6, are obtained.

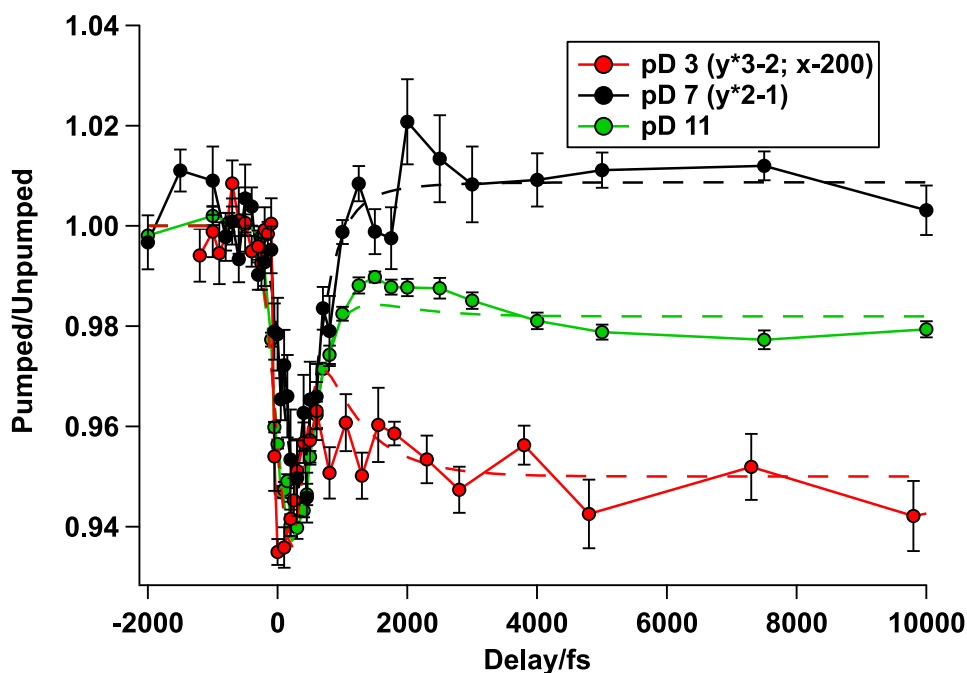


Figure 6.6: Time traces for the cross-peaks of the $\text{TiO}_2\text{-D}_2\text{O}$ -interface with pD 3 (red), 7 (black) and 11 (green), pumped at 2550 cm^{-1} , integrated between 2350 and 2450 cm^{-1} . The traces for pD 3 and 7 are scaled according to the legend. Dashed lines are the corresponding fits.

Again, the traces for pD 3 and 7 have been scaled the same way as before, as stated in the legend.

Now the picture has changed, especially considering the heat effects at late time scales beyond 1000 fs . Still, all the time traces show the typical dip in the pumped/unpumped ratio at around 0 fs , though the overall intensity-drop is less pronounced. When comparing the dips with the ones shown in figure 6.5, they seem to be slightly shifted to later times (most obvious for pD 11). However, at longer time scales, the ratio after 1000 fs stays below 1 for pD 11 (green) and especially for pD 3 (red). In the case of pD 7 (black) it rises back to slightly above 1. Considering the blue shift of the heated spectrum, this result is to be expected, as has been shown in figure 6.3. Why the effect is so small for pD 7, however, is unclear.

In order to properly compare all time scales, it is necessary to fit the time traces. This is done by using the four-level-model that has been introduced in chapter 2. Amongst the fit parameters are the lifetime of the excited state (τ_1) and the delay-time offset μ . The latter parameter shows by how much the turning point of the drop of the pumped/unpumped ratio deviates from 0 fs . Additionally, the influence of the heat and the amplitude of the intensity drop are free parameters which, however, play no major role in the following discussion. For the relaxation of the intermediate state to the heated ground state (τ_2 , see figure 2.5), a time constant of 700 fs has been assumed, as has been found by 2D-IR-measurements in bulk water [106]. The fits are included in figures 6.5 and 6.6 as dashed lines. The results of this fitting process are presented in table 6.1.

Table 6.1: Fit results of the direct and the cross peaks (indicated by \otimes), shown in figures 6.5 and 6.6. τ_1 is the relaxation time, $\Delta\mu$ is the time offset between the direct and the cross peak.

binning	2550 cm^{-1}	2400 cm^{-1} \otimes	
	τ_1/fs	τ_1/fs	$\Delta\mu/fs$
pD 3	660 \pm 120	150 \pm 70	230 \pm 20
pD 7	350 \pm 50	240 \pm 40	110 \pm 40
pD 11	370 \pm 20	310 \pm 10	140 \pm 10

In table 6.1, τ_1 is the lifetime of the excited state, so the parameter of interest obtained from the fit. $\Delta\mu$ is the delay-time difference between the direct and the cross peak ($\Delta\mu = \mu_{\text{cross}} - \mu_{\text{direct}}$).

The relaxation times τ_1 obtained by fitting the traces of the direct peak clearly indicate, that the lifetime of the excited states of water at solutions of pD 7 and 11 (above the pzc) are the same within the experimental error, namely about 360 fs. Additionally, it gets clear that, with a value of about 660 fs, the relaxation time of the water molecules at pD 3 is almost twice as long. This value is very close to the thermalisation time of the intermediate state back to the heated ground state, that is included in the fit with a time constant of 700 fs. Indeed, when setting this value to zero and letting the fit run, a relaxation time of water molecules at pD 3 of 560 fs is obtained, which is still close to the value in table 6.1. Using a model excluding the intermediate state might provide a more robust investigation of this matter. However, if the intermediate state is excluded completely, the resulting fit will not assume the very special shape of the time traces obtained by integrating at lower frequencies (compare figure 6.6). There, after an initial increase of the pumped/unpumped ratio, the heat leads to a long term ratio drop. The small local maximum can only be fitted by including an intermediate state.

These results indicate, that the stronger hydrogen bonding network of the water molecules in contact with TiO_2 for higher pD-values, presents a more efficient path for energy transfer and dissipation than the normal water-like system at pD 3. Of course, by pumping at a frequency of 2550 cm^{-1} for all pD-values, subsets of water molecules with the same hydrogen bonding strength have been excited by the pump-pulse. However, the surrounding hydrogen bonding network is very different for the molecules in these solutions, so different pathways of relaxation might be present after all.

From energy transfer theories such as the Förster resonance energy transfer (FRET) it is known that the transfer from one molecule to another increases when the donor-acceptor-distance decreases. Stronger hydrogen bonds between two water molecules indicate they are in close proximity. Therefore a strong hydrogen bonding network facilitates the transfer of energy into the bulk system due to shorter distances between the oscillators. This enables a faster signal recovery of the interfacial molecules.

As has been mentioned above, when looking at figure 6.4, the main spectral hole burning occurs at frequencies above 2550 cm^{-1} and not centered around the pump-frequency. It could be argued, that an immediate heat effect shifts the maximum response of the system to the blue side of the spectrum, so that it appears to lie above 2600 cm^{-1} . If

so, however, the effect would manifest itself as an increase of the pumped/unpumped ratio and not a dip, as can be observed in figure 6.4. Therefore, the origin of the dip above 2600 cm^{-1} remains unknown. However, by analysing and fitting the time traces for the spectral region between 2550 and 2700 cm^{-1} , the same trends of relaxation time as before could be observed (compare table 6.1): for pD 7 and 11 τ_1 was similarly short, whereas for pD 3 it was significantly longer. Therefore it can be concluded, that the effect of a blue-shifted dip has no influence on the general trends.

Table 6.1 also shows the fit results of the traces obtained by analysing the cross-peaks at 2400 cm^{-1} , marked by \otimes . For all pD-values the relaxation times τ_1 are smaller than for the direct peaks, meaning the relaxation is accelerated. Again for pD 7 and 11 the relaxation occurs at a comparable time of about 290 fs . However, for pD 3 the fitting resulted in a relaxation time of 70 fs , which is beyond the time resolution of the instrument. The value of 150 fs presented in table 6.1 is the result of the estimation of the upper limit for τ_1 , by trying out various values by hand. The error of 70 fs is the original fitting result. Additionally, the influence of the heat might be influencing the fit result. In general, the parameters obtained by the fit are not independent of each other. This was found by analysing the correlation matrix of the values. Therefore, it is important to be very careful when comparing the values for τ_1 of the direct and the cross-peaks.

In addition to the lifetimes of the excited states (τ_1), table 6.1 contains the delay offset between the direct and the cross peak. As has been explained above, μ is the offset time of the turning point in the signal drop (deviation from 0 fs). For fitting the cross peak, the same fitting equation as for the direct peak has been used (see equation 2.29). Therefore, the delay time difference between the direct- and the cross peak is defined as $\Delta\mu = \mu_{\text{cross}} - \mu_{\text{direct}}$. As can be seen, for all pD values studied, the cross-peak occurs later than the direct peak. Again the values of pD 7 and 11 are the same within the experimental error (around 120 fs), whereas for pD 3 the difference is almost twice as long (230 fs). This result indicates that the energy transfer from the direct to the cross peak takes a finite time interval for all pD values. As has been explained in section 6.1, this is a hint for coupling between the corresponding oscillators. Here the energy transfer from one vibrating group to the other takes time so that the cross peak occurs after the direct peak. The value of $\Delta\mu$ is more robust than the comparison of the relaxation times obtained by the fit, owing to the fact that the delay time difference can already be estimated by eye when comparing the time traces of the direct and the cross-peaks without x-axis scaling.

It is very well possible, that the four-level model presented in chapter 2 and used here for fitting the time traces is not the most accurate to describe the data. As was published by Livingstone et al., also a six-level model could be able to explain the relaxation behaviour [45]. This model is presented in figure 6.7.

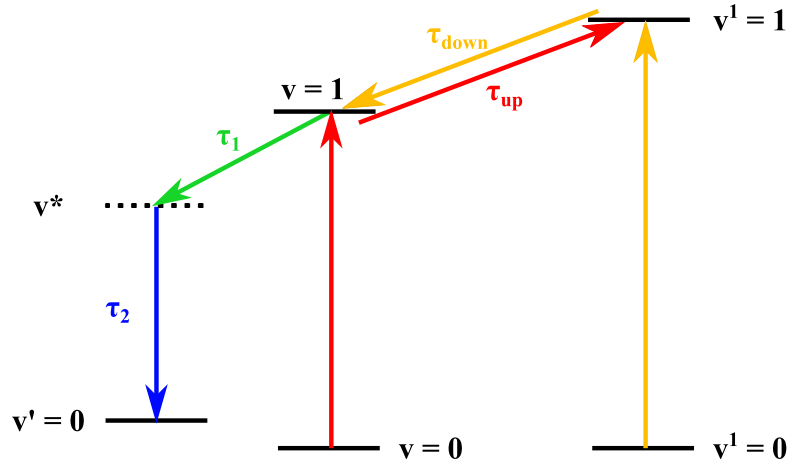


Figure 6.7: Scheme of the six-level-model used by Livingstone et al. [45]. τ_{up} and τ_{down} describe the time needed for the energy to be transferred from one state to the other.

Here τ_{up} and τ_{down} are the time needed for the up- or downhill-coupling to occur. Considering the discussion above, these values might be comparable to the value $\Delta\mu$, as can be obtained by the four-level-model. However, in contrast to figure 6.7, also the direct relaxation of the high frequency mode, via the intermediate state to the heated ground state could be possible and should be included in the model. Therefore, for simplicity, the four-level-model is used in this thesis.

Taking a second look at the right column of figure 6.4, displaying the bleached spectra of water at the TiO_2 interface for a D_2O solution of pD 11, at 500 fs (third row) a small peak around 2530 cm^{-1} can be observed. This small, but significant peak might originate from a vibrationally excited-state SFG-processes [107], possibly caused by the molecules responsible for the signal of unknown origin above 2600 cm^{-1} . Figure 6.8 shows this process schematically.

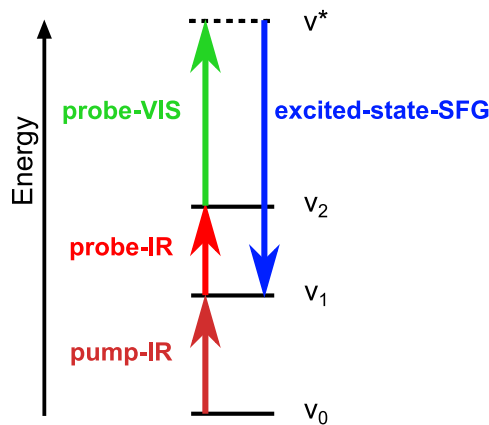


Figure 6.8: Schematic display of the vibrationally excited-state SFG-process. The SFG-process starts and ends at the first vibrationally excited state.

Here the water molecules are excited by the pump-pulse in the known 0-1 fashion of linear absorption. After that, the IR-beam induces a coherence between the first and

the second vibrationally excited state. With the visible beam now the SFG-process is induced, starting from the first excited state, to which, upon emission of an SFG-photon, the molecule relaxes back. Due to the anharmonic nature of the oscillators, the resulting photon has a slightly lower frequency than the SFG-signal involving only the first excited state [108].

In this way, due to the pump pulse, the molecule is available for an SFG-signal, which significantly increases the intensity of the pumped spectrum. Due to the fact that the described excited-state SFG signal is observed at around 500 *fs* and at a frequency of about 2530 cm^{-1} , it lies directly within the region of the spectral hole burning (between 2500 to 2600 cm^{-1}). Therefore it is not possible to obtain a time trace of this signal, since it is overwhelmed by the effects of spectral hole burning and heat. Its contribution to the SFG-signal might, however, influence the relaxation time obtained by the fitting. The next subsection will include the discussion of time-resolved SFG-experiments using a pump-pulse frequency of 2400 cm^{-1} .

6.2.2 Pump-Frequency of 2400 cm^{-1}

In order to see the behaviour of the system when pumped at lower frequencies, experiments with a pump frequency centered around 2400 cm^{-1} , with a width of about 80 cm^{-1} , have been conducted on the same TiO_2 sample of 150 nm thickness, again in contact with solutions of various pD-values. Figure 6.9 shows the bleach-spectra, so the pumped divided by the unpumped, for pD 3 (left), 7 (center) and 11 (right) for -1000 (top row), 0 , (second row), 500 (third row) and 10000 fs (bottom row).

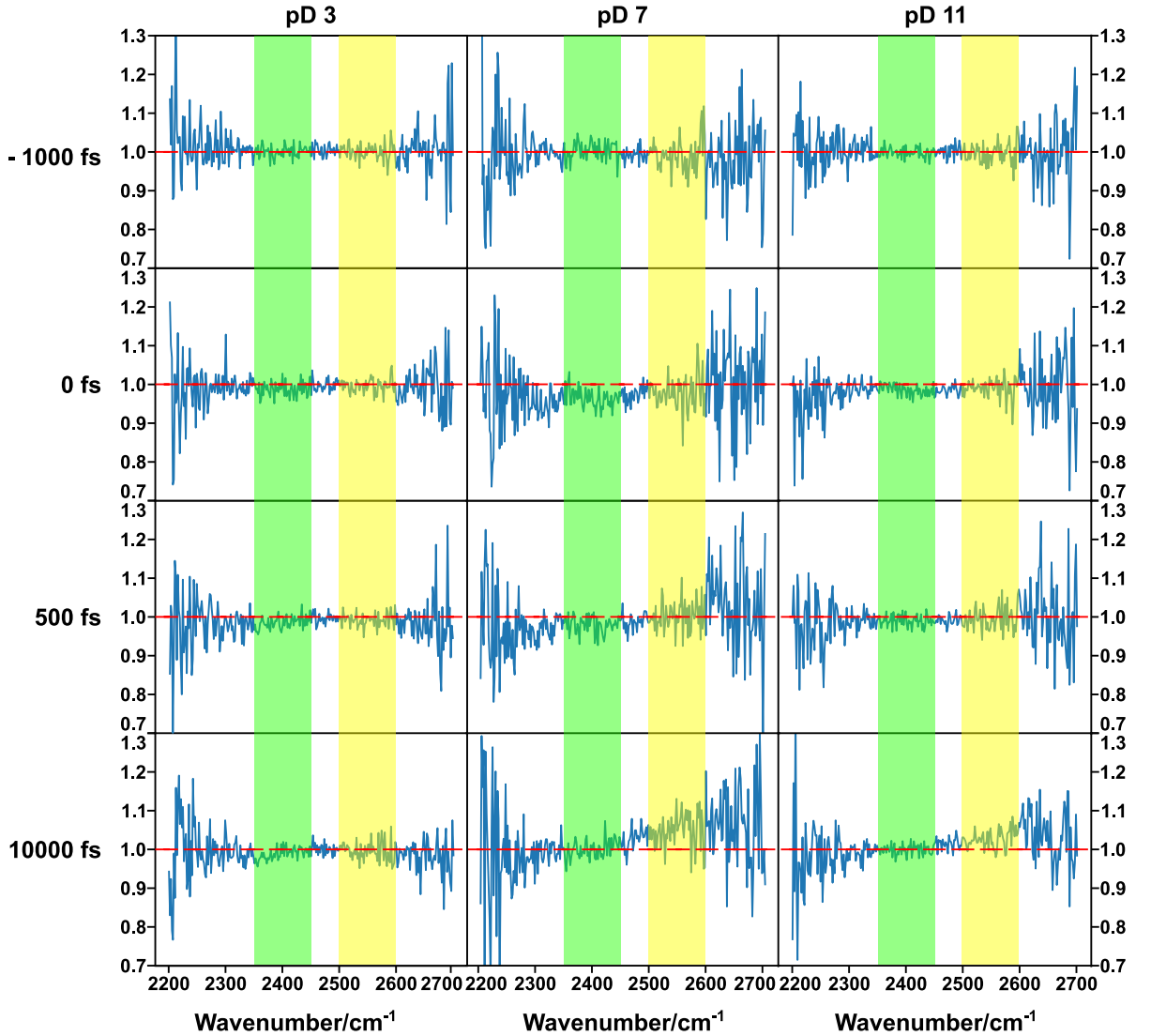


Figure 6.9: Ratio of pumped/unpumped SFG-spectra of pD 3 (left), 7 (center) and 11 (right) for -1000 (top row), 0 (second row), 500 (third row) and 10000 fs (bottom row).

Comparing the results of the ratio of the pumped divided by the unpumped spectra pumped at 2400 cm^{-1} with the ones pumped at 2550 cm^{-1} (figure 6.4) it immediately gets clear, that the influence of the latter pump-pulse is a lot stronger. This is due to the fact, that the pump-intensity at 2400 cm^{-1} is only 25% of that at 2550 cm^{-1} . For

the data presented in figure 6.9, the measurements of pD 3 and pD 11 were taken on the same day. This might explain the comparably low effect of the pump pulse on the water system for these two solutions, compared to the measurements taken for pD 7. Laser fluctuations and alignment play a crucial role in pump-probe SFG measurements, especially when working with very low laser intensities.

However, the general trend looks relatively similar to the one presented in figure 6.4. At negative times (top row), no effect of the pump-pulse can be seen, due to the fact, that it has not yet arrived at the sample. At 0 *fs* (second row), especially for pD 7 and 11, a dip in the ratio can be observed, this time, however, at around 2400 cm^{-1} , due to spectral hole burning by the pump-pulse (green transparent bar). For pD 3 this dip is barely visible. At 2550 cm^{-1} no such dip can be observed (yellow transparent bar). For longer timescales (10000 *fs*, bottom row) in the cases of pD 7 and 11 a relatively strong and long-lasting heat effect can be observed, manifesting itself as a ratio above 1 at high frequencies, but in this case not below 1 for low frequencies. For pD 3 only a dip at low frequencies can be seen.

Due to the very low impact of the pump-pulse on the spectra, here it is even more crucial to take a look at the time traces. These are presented in figure 6.10 with a spectral binning from 2350 to 2450 cm^{-1} (top). Additionally, in the bottom panel the cross-peaks, resulting from binning the response between 2500 and 2600 cm^{-1} , are included.

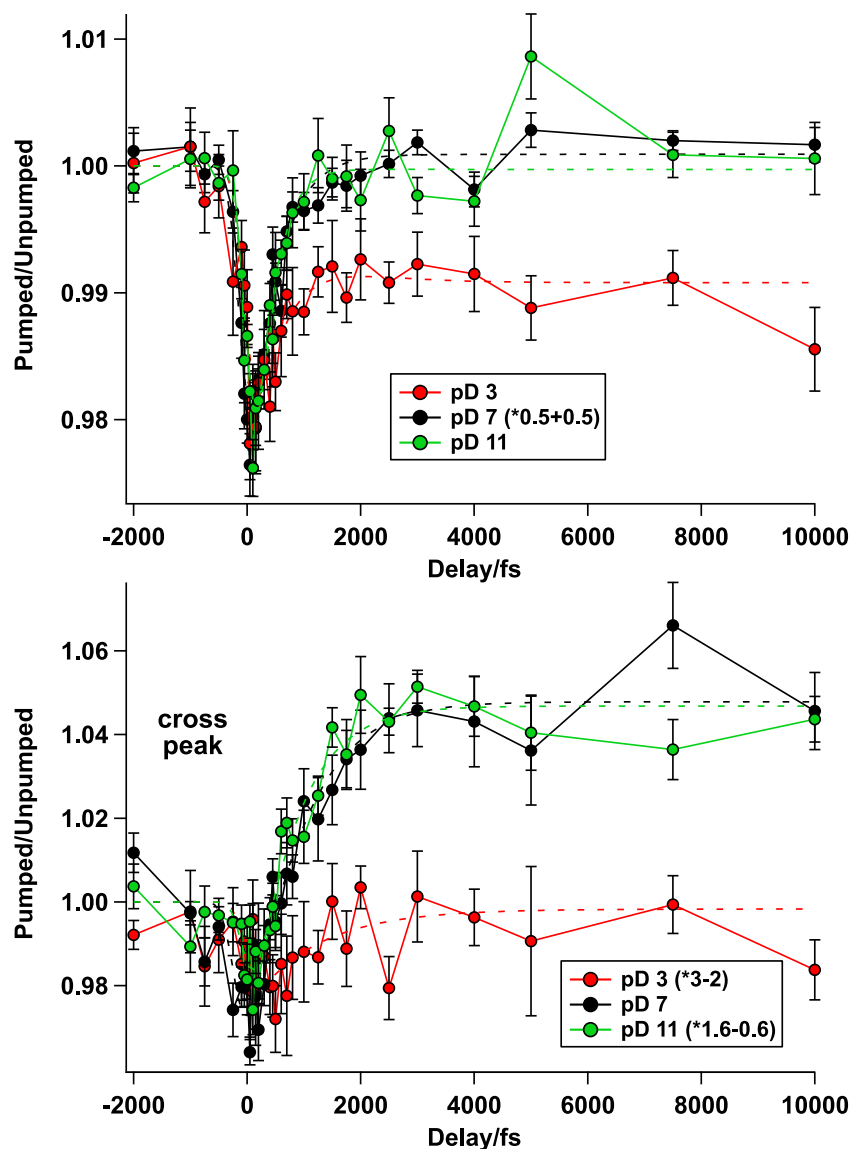


Figure 6.10: Time traces of the $\text{TiO}_2\text{-D}_2\text{O}$ -interface at pD 3 (red), 7 (black) and 11 (green) pumped at 2400 cm^{-1} . Top: binning at the pump-frequency (2350 to 2450 cm^{-1}). Bottom: binning at the cross peak (2500 to 2600 cm^{-1}). Dashed lines are the corresponding fits.

Here again, the traces have been scaled according to the notes in the legend. For all time traces binned at the pump-pulses frequency (top) the spectral hole burning results in the decrease of the signal around $t = 0$, followed by the relatively quick relaxation of the perturbed molecules. As has been explained before, the heating effect at late times (ps) is largely independent of the pump frequency, as long as it hits a resonance of molecules in the system that can absorb the energy and are in some way coupled to the rest of the molecules. Therefore, different than for the pumping with 2550 cm^{-1} , no higher intensity of the heated pumped spectrum can be observed for long time scales, as was seen in figure 6.5. On the contrary, the traces rather resemble the cross peak of the spectrum for pD 7 pumped at 2550 cm^{-1} , shown in figure 6.6, as was to

be expected for this frequency range. Of course, when comparing the top of figure 6.10 with figure 6.6, the details of the heat differ. For example, in the cases of pD 3 and 7, the time traces converge to lower relative pumped/unpumped-ratios for the 2550 cm^{-1} pump frequency, than for the 2400 cm^{-1} . In the case of pD 11 the effect is less pronounced. As mentioned above, one reason for the general differences in the behaviour of the heated spectra is the lower pump-intensity, resulting in a less elevated temperature after relaxation and thus a smaller heat effect. For a pump frequency of 2550 cm^{-1} the energy of the laser was about $20\text{ }\mu\text{J}$, whereas for 2400 cm^{-1} only about $5\text{ }\mu\text{J}$ could be gained. The low intensity at lower frequency is a result of the reduced efficiency of the LiNbO_3 crystal in this region, used to generate the pump-IR, as was described in section 2.4. As can clearly be seen in figure 6.10 the traces are relatively noisy, especially for the cross-peaks at the bottom graph. This is also an effect of the low pump-intensity. Looking at the bottom panel of figure 6.10, showing the cross-peaks binned at 2500 to 2600 cm^{-1} , strong similarities to the normal traces shown in figure 6.5 can be seen, especially in the behaviour of the heated spectra at delay times of ps . Again pD 7 (black) and 11 (green) behave very similar with a strong increase in intensity for the pumped spectrum. The trace for pD 3 (red) is very noisy so that details of the dynamics are not visible. However, at negative and long positive time delays the ratio between pumped and unpumped spectrum lies around one, just as in the 2550 cm^{-1} pump-frequency case. In order to compare the dynamics of the system in dependence of the pump frequency, the traces were fitted using the same four-level model as has been used above. Table 6.2 shows the results of the direct (2400 cm^{-1}) and the cross peak (2550 cm^{-1}). The latter is marked by \otimes .

Table 6.2: Fit results of the direct and the cross peaks (indicated by \otimes), pumped at 2400 cm^{-1} shown in figure 6.10. τ_1 is the relaxation time, $\Delta\mu$ is the time offset between the direct and the cross peak.

binning	2400 cm^{-1}	$2550\text{ cm}^{-1} \otimes$	
	τ_1/fs	τ_1/fs	$\Delta\mu/fs$
pD 3	690 ± 170	1240 ± 730	20 ± 110
pD 7	430 ± 50	630 ± 170	-110 ± 90
pD 11	300 ± 50	400 ± 100	-50 ± 60

When comparing the direct peaks given in tables 6.1 and 6.2, it can be seen that for both pump-frequencies (2550 and 2400 cm^{-1} , respectively), the lifetime of the marked oscillators are the same within the error. Additionally, for both frequencies the relaxation time at pD 3 is the longest, whereas for pD 7 and 11 they are very similar within the error. As has been explained in section 6.2.1, one reason for this effect could lie in the generally stronger hydrogen bonding network for water molecules at the $\text{D}_2\text{O-TiO}_2$ -interface at higher pD-values, that lie above the pzc. The stronger interaction between the water molecules might facilitate the energy transfer from one to the other.

By taking a closer look at the time delay shifts ($\Delta\mu$) of the fitting results presented in table 6.2, it gets clear that, within the experimental error, all values lie around 0 fs . As has been explained in section 6.1, in the case of a coupling mechanism without energy

transfer between the higher and the lower frequency oscillators, the coupling effect might be observed without time delay. The values for $\Delta\mu$ for a pump frequency of 2550 cm^{-1} , presented in table 6.1, show a different picture where a significant delay time between the occurrence of the direct and the cross peak was found. Therefore it can be concluded that, when the system is pumped at a higher frequency, the coupling is dominated by a down-hill energy transfer-mechanism. In the case of a pump frequency of 2400 cm^{-1} , there is no observable delay-time and therefore no up-hill energy transfer.

It would be possible to argue, that an up-hill process would include an energy uptake from the surrounding, so it could be unfavourable. However, the energy difference between the direct and the cross peak is just 150 cm^{-1} , which lies well in the range of $k_B T$. Therefore, up- and down-hill energy transfers should be equally possible. The fact that no up-hill energy transfer can be observed in this system and that the coupling is dominated by an instantaneous process is very surprising. However, in order to fully analyse the situation, the use of a six-level-model would be useful.

In this section it could be shown, that the data of the time-resolved SFG-experiments with a pump frequency of 2400 cm^{-1} presented in table 6.2 are difficult to interpret due to the large errors. For future works, more experiments should be conducted in order to decrease the uncertainties and to get better statistics on the results.

The next section will include the discussion of time-resolved SFG-experiments involving isotopically diluted solutions of pD 3, 7 and 11.

6.3 Time Resolved SFG-spectra of the TiO₂-D₂O-Interface using Isotopically Diluted D₂O-Solutions

In section 6.2 pump-probe SFG-experiments of the TiO₂-D₂O-interface have been presented, using solutions of pD 3, 7 and 11. However, as has been shown in chapter 5, additional insight can be gained by using isotopically diluted solutions, which means mixing D₂O with H₂O. As has been explained above, the exchange of deuterium with hydrogen leads to the formation of HDO-molecules, suppressing inter- and intramolecular coupling pathways. In a static SFG-spectrum the result will be the merging of two peaks into one and the nonlinear decrease of intensity for the two peaks with rising H₂O concentration. In pump-probe-experiments, the suppression of coupling between water molecules results in the suppression of relaxation pathways for the molecules excited by the pump-pulse. This means that the additional energy the molecule contains either finds other pathways or just remains longer at the oscillator until it finds a coupling partner. In this way, it is possible to learn more about the coupling mechanisms of the system of interest than would be possible by only conducting static SFG-experiments. Figure 6.11 shows the bleach spectra (pumped divided by unpumped) of 50:50 mixtures of D₂O and H₂O pumped at 2550 cm^{-1} with pD values of 3 (left), 7 (center) and 11 (right). The delay points are -1000 (top row), 0 (second row), 500 (third row) and 10000 fs (bottom row).

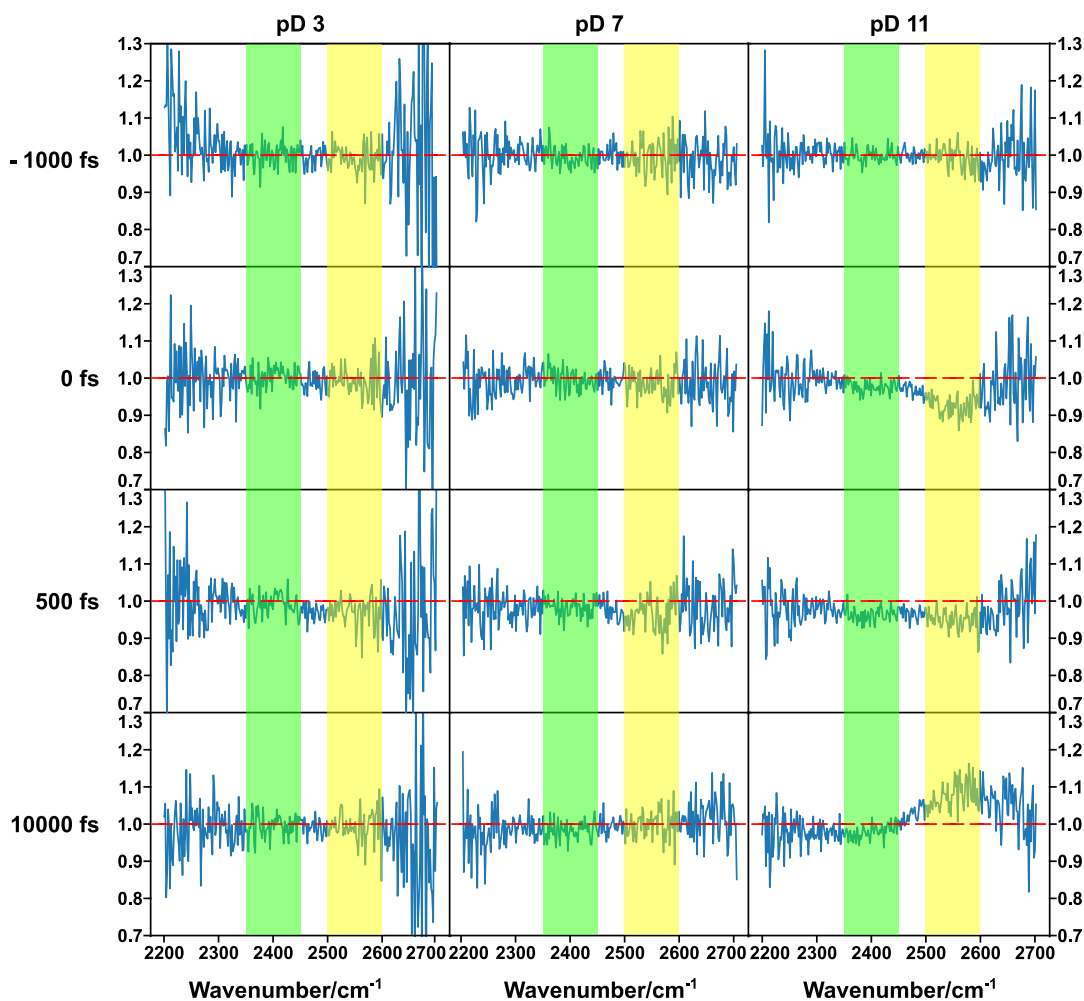


Figure 6.11: Pumped divided by unpumped spectra of isotopically diluted D_2O pumped at 2550 cm^{-1} for pD 3 (red), pD 7 (black) and pD 11 (green). The time points are -1000 (top row), 0 (second row), 500 (third row) and 10000 fs (bottom row).

It gets clear that the influence of the 2550 cm^{-1} pump-pulse on the TiO_2 - D_2O -interface in isotopically diluted solutions is very small. Considering that only half the oscillators are available for the spectra, while the other half resonates in a very different spectral window (approximately 3000 to 3700 cm^{-1}), this is an expected result. The strongest influence of the pump-pulse can be observed for pD 11, manifesting itself as the spectral hole burning at the pump frequency (0 fs), the equilibration of the excited molecules (500 fs) and the heated ground state spectra (10000 fs). Of course, due to the isotopic dilution, the absorption of the pump-energy is comparably low, resulting in a rather small heat effect. For pD 3 and 7 not much response to the pump pulse can be observed. An interesting point to note is that, in contrast to the 100 % D_2O solutions, here the spectral hole burning occurs only at around 2550 cm^{-1} and not mainly above 2600 cm^{-1} , as was observed in figure 6.4 and discussed above.

Again, in order to properly visualise and analyse the data presented in figure 6.11, it is necessary to integrate the bleach spectra between 2500 and 2600 cm^{-1} and plot the

result for every time point against the delay time. The results for pD 3, 7 and 11 are shown in figure 6.12.

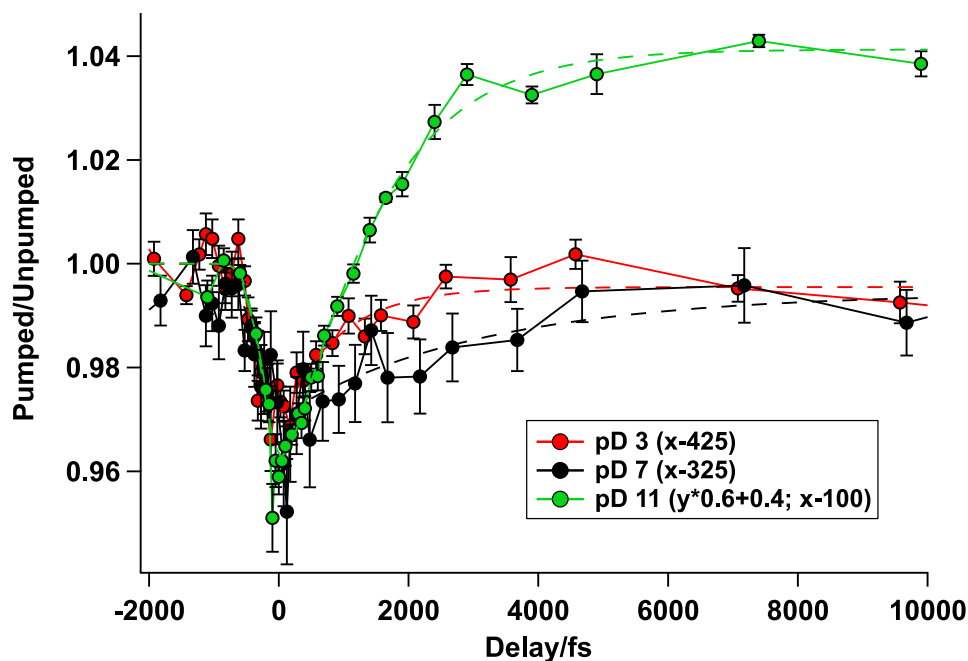


Figure 6.12: Time traces of isotopically diluted D_2O of pD 3 (red), 7 (black) and 11 (green) pumped at 2550 cm^{-1} , integrated between 2500 and 2600 cm^{-1} . The trace of pD 11 has been scaled according to the legend. The respective fit results are shown as dashed lines.

Again, the time traces have been scaled according to the legend for visualisation. If compared with the time traces from 100 % D_2O solutions, it can immediately be seen, that the dynamics are slower in the 50 % D_2O case. Interestingly, here only the trace of pD 11 shows a significantly heated pumped spectrum, whereas for pD 3 and pD 7 the signals level off at a ratio of pumped and unpumped intensity of about 1, as was to be expected if considering the bleach spectra from figure 6.11. Note that for pD 11 the trace has been scaled according to the note in the legend, in order to facilitate the comparison. Due to the lower amount of D_2O in the sample solution, the intensity of the SFG-signal is lowered, which is responsible for the noise in the traces. Fitting the data using the four-level model gave the results shown in table 6.3. For comparison, the fit results of the direct peak for 100 % D_2O (table 6.1) are included again.

Table 6.3: *Fit results for pump-probe experiments with isotopically diluted solutions of pD 3, 7 and 11. The numbers are the relaxation time τ_1 in fs. The results for the 100 % solutions from table 6.1 are included for comparability.*

	100 %	50 %
pD 3	670 \pm 120	940 \pm 160
pD 7	350 \pm 50	3170 \pm 1200
pD 11	370 \pm 20	1190 \pm 50

It can clearly be seen, that upon isotopic dilution the relaxation times of the water molecules increase significantly compared to those observed for the undiluted solutions. Astonishingly, for the D₂O-TiO₂-interface at pD 3 the system equilibrates the fastest, opposite to the trend observed for 100 % D₂O solutions. The very extreme relaxation time increase for the pD 7 case might partially be a result of the strong noise in the trace, as also evident from the large uncertainty of the inferred lifetime. However, even with the uncertainty of the fit, the increase is very large. Within the error, for pD 11 the relaxation time is now similar to that of pD 3.

As explained above in this chapter and in chapter 5, isotopic dilution suppresses intra- and intermolecular coupling. Intermolecular coupling results in an energy transfer between molecules, while intramolecular coupling is the connection between the OD-stretch vibration with an overtone of the D-O-D bending mode. When one deuterium is exchanged for a hydrogen, the vibrating OD-groups need more time to find a suitable coupling partner in their surroundings (intermolecular). Additionally, the overtone of the H-O-D bending mode vibrates in a different spectral region, so that no coupling with the OD-stretch can occur (intramolecular). Both effects can suppress relaxation pathways for the excess vibrational energy between the oscillators. When the vibrational modes are unable to transfer their excess energy, it is either transferred through a less preferred pathway or it takes longer until they find a suited acceptor group. Either effect will take more time, so that the signal relaxes more slowly than for the undiluted case.

For solutions with pD 3, the increase in relaxation time, when the solution is isotopically diluted, is not surprising, since a coupling effect has already been observed in isotope exchange experiments presented in chapter 5. There, for each pD value three peaks could be identified at the D₂O-TiO₂-interface. In the case of pD 3, the high and the central frequency mode partly originate from one common mode in their center. Therefore the result shown in table 6.3 is rather expected.

However, for pD 11 no coupling effect could be observed in the static measurements (see table 5.2). The very strong increase in relaxation time observed here is therefore rather surprising. Apparently, coupling exists in the interfacial pD 11-TiO₂ system, but only expresses itself in the energy transfer dynamics and can not be determined in the static spectrum. It might be possible, that the only coupling occurring in this system is between the water molecules and Ti-OD groups, located at the semiconductor surface itself. Due to the strong interaction of the water molecules and the semiconductor at pD 11, it could be possible that the excess energy of the D₂O is mainly transferred to the TiO₂ and then dissipated into the solid material. At high pD-values, this might be

facilitated due to the orientation of the water molecules with their deuterium atoms towards the semiconductor. If this relaxation pathway is suppressed (coupling only with Ti-OD but not with Ti-OH), the molecules need more time to find a drain for their energy. In static SFG-measurements this coupling could be invisible.

The effect of even slower dynamics for water molecules at pD 7 compared to either pD 3 or pD 11 with the isotopically diluted solution might be explained with the coupling of the system at this pD-value. Though no coupling effect could be observed for water molecules at pD 11 in static measurements, it can not be excluded, that there is no observable coupling for pD 7. However, these measurements have not been performed. Due to the very unfavourable signal-to-noise-ratio of the water molecules in 50 % D₂O solutions, the analysis of the cross-peaks around 2400 cm^{-1} is not feasible. Even more so, no pump-probe measurements with a pump frequency of 2400 cm^{-1} have been conducted, since the isotopic dilution together with the very low pump intensity in this frequency range would make the fitting of these data unfeasible.

6.4 Conclusion

In this chapter time-resolved SFG-measurements of water at the D₂O-TiO₂-interface for solutions at pD 3, 7 and 11 have been presented. It could be shown, that, pumping at a frequency of 2550 cm^{-1} , the lifetime of the excited state for pD 3 is almost twice as long (about 660 *fs*) as for pD 7 and 11 (about 360 *fs*). pD 7 and 11 show a similar relaxation time as bulk D₂O, which has a lifetime of about 350-400 *fs* [109, 110]. This finding is attributed to the fact, that the point of zero charge of TiO₂ lies around pD 5, so that at pD 3 the interface is positively, at pD 7 and 11 negatively charged, which could lead to different hydrogen-bonding networks, that offer different paths for energy transfer. Pump-probe experiments at a pump-frequency of 2400 cm^{-1} gave the same trend.

Comparing these results for TiO₂ with results of other mineral materials, astonishingly different influences on the water structure can be observed. Silica (SiO₂), for example, has a point of zero charge at around pH 2. Therefore for a wide pH-range, the interface is dominated by negative charges, as was shown by Shen et al. in 1994 [111]. Time-resolved SFG measurements on this system between pH 2 and 12 have shown, that the lifetime of the excited state of the water molecules is twice as long at the pzc (neutral surface, 570 *fs*) as for pH 12 (negatively charged surface, 255 *fs*) [112]. It was also shown, that the water signal at this interface could be influenced by the addition of salt, hinting to the fact, that bulk-like, near-interface water molecules were measured. As was shown in chapter 5, for TiO₂ this is not the case. Additionally, the fact that the pzc of silica lies at pH 2, no measurements with a positively charged interface have been performed so far. The ionic strength of such solutions would be rather high so that its influence may not be negligible.

Alumina (Al₂O₃) on the other hand, has a point of zero charge around pH 6-8. Here, depending on the solution pH, positively, neutral, or negatively charged interfaces can be studied with less extreme pH-values. In this way, time-resolved SFG-measurements of the Al₂O₃ (0001) surface in contact with water have been performed by the group

of Borguet et al. [113]. They as well could show, that close to the pzc, the vibrational relaxation of the interfacial water molecules was slower (neutral interface, 220 *fs*), than at pH 12 (negative interface, 109 *fs*). However, when going to pH 2 (positive interface), the relaxation time was the same as for pH 12, indicating that when deviating from the pzc in any direction, preferred relaxation pathways are opened. The lifetimes of the excited states show, that at more extreme pH values, the relaxation is even faster than that of bulk water. This fact, and the fact that the addition of salt does not have a significant influence on the dynamics shows that indeed interfacial water molecules are measured and near-surface water layers show no significant contribution for alumina.

However, when comparing these results with the results presented in this chapter, it should be noted, that the SFG-spectrum of the $\text{Al}_2\text{O}_3\text{-H}_2\text{O}$ -interface shows a strong peak at around 3000 cm^{-1} , which is a hint for very strongly bound water molecules [113]. The $\text{TiO}_2\text{-D}_2\text{O}$ -interface shows no peak of comparable hydrogen-bonding strength. Therefore it is not surprising, that for alumina faster dynamics can be found, even when considering the generally slower dynamics for D_2O compared with H_2O (250-400 *fs* in bulk [114]), since a stronger hydrogen bonding network can facilitate the energy transfer. Another explanation given by the group of Borguet is a possible fast proton transfer between the interfacial water molecules and the aluminol (Al-OH) groups that could dominate the vibrational relaxation. They claim, that at pH 6 (pzc), this proton transfer is minimal due to the neutral nature of the surface [113]. This explanation, however, is not applicable to the data presented in this chapter, since the relaxation time of pD 3 is significantly longer than that for pD 7 and 11, which are similarly fast.

In addition to the trend of slower relaxation of the interfacial water molecules at a lower solution pD, it could also be shown that the dominating coupling-mechanism depends on the pump-frequency. When pumping at a frequency of 2550 cm^{-1} , the coupling between the pumped modes and oscillators that vibrate at a lower frequency could be observed, which takes about 120 *fs* for pD 7 and 11, and about 200 *fs* for pD 3 to appear. This relatively long time is a hint for a down-hill energy transfer. When pumping with a laser pulse of 2400 cm^{-1} in frequency, no such time delay can be observed for the coupling between the low and the high-frequency modes. Therefore, the coupling mechanism most probably involves the instantaneous frequency shift of the indirect peak by coupling to the direct mode.

Time-resolved measurements of the $\text{TiO}_2\text{-D}_2\text{O}$ -interface with isotopically diluted solutions (50:50 $\text{D}_2\text{O}:\text{H}_2\text{O}$) of pD 3, 7 and 11 have shown that for all pD-values the lifetime of the excited oscillators is significantly increased (to about 1100 *fs*), though for pD 7 the increase is the highest (to about 1900 *fs*). This shows, that, in contrast to what has been presented in chapter 5, also for pD 11 coupling effects play a role. When half the deuterium atoms are replaced with hydrogen, coupling mechanisms are suppressed, leaving the excited water molecules hindered in transferring their vibrational energy. Similar results were shown for bulk water, where the relaxation time of the OH-stretch vibration in the HDO molecule was observed to increase to about 700 *fs* [115].

In addition to the spectral hole burning and the subsequent relaxation of the excited molecules, in the case of pD 11 after 500 *fs*, a small positive feature could be identified in the bleach-spectrum. This peak is attributed to the excited state absorption of the

unknown groups that are responsible for the intensity drop above 2600 cm^{-1} when pumping at 2550 cm^{-1} , marked by the IR-pulse. These molecules contribute to the SFG-signal by starting the SFG-process from the first excited state (v_1) instead of the ground state (v_0). The slightly lower frequency of this peak comes from the anharmonic nature of the oscillators [114]. However, due to its spectral position at about 2530 cm^{-1} , it is not possible to obtain a time trace of this signal, since it is overwhelmed by the spectral hole burning and the ingrowth of the heated signal.

7 Conclusion and Outlook

Owing to its abundance on the earth's surface and its importance for our life and our environment, water is an extensively studied material. In this thesis, two water-based systems were investigated: first, the cationic surfactant CTAB and its behaviour at the water-air-interface in the presence of high amounts of sodium chloride and second, as the main project of this work, the water structure and dynamics at the water-titanium dioxide-interface at different solution pDs.

Both projects were realised by using Sum-Frequency-Generation (SFG) spectroscopy. In this technique, a visible and an infrared laser-beam are overlapped in space and time on the interface of interest. The infrared beam is in resonance with the vibrations of specific molecular groups, such as the CH- or the OH-stretch vibrations, that serve as molecular reporters. The visible beam upconverts the vibrational polarization of the molecules at the interface to generate a polarization that oscillates at the sum of the frequencies of the incoming laser beams. This polarization serves as a source term for emitted photons at that frequency. Due to its selection rules, this process is forbidden in centrosymmetric media, such as bulk water, which makes SFG an intrinsically interface-specific method. This also means, that enhanced molecular order in the interfacial region gives rise to higher intensities in the SFG-spectrum.

7.1 CTAB at the Water-Air-Interface

Surfactants play an important role in our industrialized world, however most of the time in aqueous systems. In this work, as an introductory experimental chapter, the influence of highly concentrated NaCl solutions on the behaviour of CTAB at the water-air-interface was studied. Using surface tension measurements on this system, a collaborating group could show that high levels of NaCl decrease the critical micellar concentration (CMC) of the surfactant significantly. Additionally, dynamic surface tension measurements showed that the time needed for the surfactant to reach an equilibrium state of surface coverage is strongly decreased in the presence of salt. Questions that could not be answered by these experiments were first, what is the structure of the surfactants at the water-air-interface at different concentrations of CTAB as well as salt and second, what is the underlying mechanism of these effects.

Using SFG spectroscopy, the structure of the surfactants at the interface was studied for three concentrations of CTAB, namely 0.01, 0.1 and 0.9 *millimolar* (in the following description abbreviated as *mm*) with and without 5.5 *m* (molal) NaCl. Comparing the measurements with and without salt, it could be shown that the addition of the

electrolyte leads to a decrease in the overall intensity of the SFG-spectrum. Especially in the cases of 0.1 and 0.9 *mm* CTAB, the intensity dropped by a factor of ten. By fitting the data and analysing the amplitude of each peak, it was shown that the main reason for this huge difference in intensity comes from the water signal. For 0.01 *mm* CTAB, without salt only a small water signal was present, whereas no CH-signals could be observed. With salt, the SFG-signal was comparable to that of 0.1 or 0.9 *mm* CTAB with salt.

If no salt is present, the positive charge of the cationic surfactant at the interface orients its surrounding water molecules so that their hydrogen atoms are pointing away from the lipid headgroups towards the bulk water. As has been explained before, the higher the order of the probed molecules is, the higher the SFG-intensity will be. When salt is added to the solution, the large amount of chloride anions screens the positive charge of the surfactants head groups, so that their strong influence on the water molecules is lost, leading to a loss in order. Therefore the SFG-intensity drops.

Compared to the strong difference in amplitude for the water signal, analysis of the CH-stretch vibrations showed, that the influence of salt on the order of the surfactant molecules themselves was a lot smaller for 0.1 and 0.9 *mm* CTAB. Nevertheless, fitting and analyzing the results for 0.1 *mm* CTAB, showed yet a clear difference in amplitude of the response of the system with and without salt. In the presence of the electrolyte, the CH-stretch vibrations showed a higher order than in its absence. This leads to the conclusion, that the charge screening in the presence of salt not only changes the water structure, but also influences the packing of the surfactant itself.

With these results, eventually, both questions from above could be answered. At 0.01 *mm* CTAB without salt, the positive head groups repel each other, leading to a random order and probably also a reduced number of surfactant molecules at the interface. No CH-vibrations could be observed, but the water signal was clearly influenced by the presence of a positive charge. With salt, the packing of molecules can be denser due to charge screening of the surfactants head group. For 0.9 *mm* CTAB, the effect of salt on the surfactants surface density is a lot smaller, showing that apparently the packing is close to saturation, with or without NaCl. Also the ratio of the CH₂- and the CH₃-stretch vibrations was more in favour for the latter, which is a hint for fewer gauche-defects, caused by denser packing of the hydrophobic tails. For the intermediate CTAB concentration of 0.1 *mm*, an effect of the salt on the order of the surfactant could be observed, but was significantly smaller than for 0.01 *mm* CTAB.

Additional kinetic experiments, with a time resolution of 1 *min* confirmed the decelerated surface equilibration for high salt concentrations. For all surfactant concentrations, without the electrolyte, the interface was in equilibrium immediately and without any changes after the first spectrum. The same effect was the case for 0.9 *mm* CTAB with 5.5 *m* NaCl. For 0.1 *mm* of the surfactant, the surface was covered after about 2 *min*. In the case of the lowest concentration studied (0.01 *mm* CTAB), still after about 11 *min* changes could be observed. This confirms the results obtained by dynamic surface tension measurements.

From these experiments, in combination with the (dynamic) surface tension measurements, it could be concluded that in the presence of salt, less monomeric surfactant molecules

are present in the solution, which leads to a slower equilibration at the surface. This was shown by the decrease of the CMC in combination with the time dependence of the CH-stretch vibration. Also, the fact that the CH-vibrations for low CTAB concentrations are only seen in the presence of salts, confirms this conclusion.

In order to study the structure of CTAB on the water-air interface and how it is influenced by large amounts of salt, SFG experiments using a Langmuir-trough might be beneficial. By combining these two techniques, a more direct correlation between surface tension and SFG-intensity can be obtained, than would be possible by separate measurements. The use of other cationic surfactants could address the question whether this behaviour is coincidental or follows a general trend. Also, the use of different salts could show if the behaviour is general or special for sodium chloride. The use of multivalent ions such as magnesium could possibly show whether the ordering effect depends on the ion concentration or the overall charge.

An interesting question to answer is whether negative surfactants, for example, sodium hexadecyl sulfate, show similar behaviour in the presence of the same amount of sodium chloride. In this case, the orientation of water molecules without the salt would be the other way around, with the hydrogen atoms towards the surfactants head groups. It would be interesting to see whether stronger hydrogen bonding interaction between water and the surfactant molecules, in this case, affects the behaviour of the surfactants. In this system, not the sodium cations but the chloride anions would be screening the head groups charges. Another interesting point could be the behaviour of neutral surfactants, where no charge is present, and no screening effect can influence the surfactant molecules order at the surface or in the bulk.

7.2 Sputter Deposition of TiO_2 on CaF_2

One part of the main project of this work was to deposit thin films of titanium dioxide on calcium fluoride windows using the magnetron-RF-sputter deposition technique. In this technique, argon and/or oxygen ions are created in a plasma and accelerated towards a TiO_2 target. There, upon impact, they remove material which then deposits on the desired substrate.

It was not possible to obtain reproducible results, that could be used for the SFG measurements of the water-titanium dioxide-interface. The device used for the deposition was a commercial machine with very limited controls. Also, a wide variety of materials was used in the device so that contaminations with other materials could not be excluded. Various combinations of working gas composition were investigated, as well as different sputter rates, rest gas pressures, target materials or film thicknesses. Not only between deposition processes but also in the same process the deposited thin films differed in colour, structure and stability. Additionally, when samples were considered to be good for SFG-measurements, the results were highly irreproducible. This was partly due to the fact that the signal shape and the peak intensity of the SFG-spectrum changed with the rotation of the sample around its surface normal. This effect probably came from the rotation of the substrate in the sputter chamber, resulting in a directionality of the

thin films.

After more than one year, the attempt to make the thin films needed for the measurements was abandoned. A collaborating group was found, where the thin films were made by plasma enhanced-atomic layer deposition (PE-ALD), which eventually gave reproducible results.

It might be worth, nonetheless, to use the sputter deposition technique after all, due to the specific properties of the deposited material that can be achieved. However, it is best to do this in a custom-built machine that allows a higher degree of control over the sputter parameters, such as target and substrate temperature and gas pressure. Under these circumstances, it could be possible to obtain TiO_2 thin films of different structures like anatase and rutile, with specific surface facets exposed. In this way, the influence of specific TiO_2 structures and surface terminations on the water structure at the interface with the semiconductor might be studied.

7.3 pD-Dependent Water Structure at the D_2O - TiO_2 -Interface

One of the two main parts of this thesis is the investigation of the water-titanium dioxide-interface using static SFG-spectroscopy. The aim was to study the structure of the water molecules in direct contact with the semiconductor, in order to help understand the photocatalytic splitting mechanism of water into hydrogen and oxygen.

For this purpose, thin films of TiO_2 with a thickness in the range of 100 nm, deposited using PE-ALD, were used. They were brought in contact with D_2O solutions with pD 3, 5, 7, 9 and 11. In these experiments, it could be shown, that the SFG-spectrum consists of three identifiable peaks for each of the five pD-values studied. At pD 5, the amplitudes for all three showed a minimum, whereas when the pD deviates to either lower or higher values, the intensity of the SFG-spectrum rises.

Due to the amphoteric nature of TiO_2 , this pD-value represents the point of zero charge (pzc) of titanium dioxide, where the protonation and deprotonation of the surface occur at the same rate, leading to a net zero surface charge. At the pzc, the water molecules do not experience a net orienting electric field and are ordered randomly. Since the intensity of an SFG-spectrum depends on the order in the system, the intensity is minimal. When the pD-value is decreased or increased, the surface is protonated or deprotonated, respectively. The resulting positive or negative charge orients the water molecules with their deuterium atoms towards the semiconductor's surface (high pD) or away from it (low pD).

In order to confirm this reorientation of the water molecules when the point of zero charge is crossed, phase-resolved measurements of the interface were conducted. In this technique, the SFG-signal of the interface of interest is combined with the signal of a local oscillator, such as gold, with which it interferes in the detector. Using special analysing algorithms, the phase of the SFG-signal can be extracted from the spectral interferogram. From this phase (more exact: the imaginary part of the spectrum), the orientation of the

molecular transition dipoles can be extracted. This information is lost in conventional static SFG-measurements, due to the quadratic nature of the detected SFG-signal.

The results obtained by the phase-resolved SFG-measurements confirmed the overall orientation of the majority of water molecules at the TiO_2 - D_2O -interface, marked by a negative imaginary part of the response at a pD-value of 2, corresponding to the molecules transition dipole moments pointing away from the semiconductor. In contrast, for pD 11 a positive imaginary part of the response could be observed, corresponding to molecules pointing with their deuterium atoms towards the TiO_2 surface.

However, due to the very complex nature of the system studied, the details of each peak in the phase-resolved SFG-spectrum were difficult to interpret. Therefore, experiments with different angles of incidence for the VIS-laser beam have been conducted. In all other experiments, the visible angle was at 69° from the surface normal. For these experiments, it was set to 35° , which resulted in different behavior of the non-resonant SFG-response. Due to the interference of the resonant- and the non-resonant-signal, the resulting SFG-spectrum changed shape dramatically, though the resonances of the D_2O - TiO_2 -system at pD 2 and 11 were expected to be uninfluenced. The comparison of spectra measured at different angles was used to find a combination of positive and negative amplitudes for all three signals that could be used to fit the spectra of either angle and changing from one to the other only by changing the non-resonant amplitude and phase.

In this way, it could be shown that the three resonant contributions to the SFG-spectrum of water at the TiO_2 - D_2O -interface have positive-negative-negative amplitudes for pD 2 and positive-positive-negative amplitudes for pD 11, with rising frequency. This knowledge enabled assigning the three peaks of each spectrum to the following molecular species: The peak at highest frequency is caused by OD-groups with a transition dipole moment pointing downwards (negative amplitude), accounting for the presence of interfacial TiOD groups that are relatively isolated. They probably form weak hydrogen bonds for all measured pD values, so that they oscillate at a relatively high frequency. Also, the presence of $\text{Ti-OD}^+\text{-Ti}$, so protonated bridging oxygen atoms, and TiOD_2^+ groups could contribute to the high-frequency signal, especially at lower pD-values.

The peak lowest in frequency is assigned to molecules pointing upwards, towards the TiO_2 -surface. The spectral position at the red end of the spectrum indicates that these oscillators form strong hydrogen bonds. This peak is connected with water molecules donating hydrogen bonds to oxygen atoms of interfacial TiOD groups. For high pD-values, when the interface is negatively charged due to deprotonation, also deprotonated TiO^- groups could be involved in strong hydrogen bonding, due to the localized negative charge.

The central frequency peak between the two assigned above, flips sign when the pzc is crossed. Accordingly, it is assigned to the O-H stretch mode of water molecules in the near-surface area, but not in direct contact with the surface. These water molecules are aligned under influence of the surface charge. Their distance from the surface is limited, probably to the first few water layers. This is concluded from the fact that the $\chi^{(3)}$ contribution is quite small, as has been seen in experiments with increased ionic strength. For a positively charged interface (protonated at low pD-values), the molecules

are pointing away from the TiO_2 -surface and into the bulk water. In the deprotonated case (negatively charged surface) at pD-values above the pzc, their deuterium atoms are facing towards the semiconductor. Since they show a weak frequency shift, it can be assumed that their hydrogen-bonding surrounding does not change a lot when they flip, so that they most probably form hydrogen bonds to other water molecules. For low pD-values, coupling effects involving the central peak with an overtone of the D-O-D bending mode were observed in isotopic dilution experiments. The resulting frequency shift towards lower values should be kept in mind when determining the vibrational frequency of the oscillating groups.

In order to further investigate the nature of water molecules in direct contact with a TiO_2 -surface, it could be beneficial to conduct more phase-resolved experiments on that system. Higher phase stability could be obtained by using y-cut quartz instead of a gold mirror as the source of the local oscillator. By using this device, the orientation of the water molecules obtained by the above-described procedure might be quantified, since a higher phase accuracy could be obtained. Maybe also so far undiscovered peaks might be found if a higher frequency resolution could be obtained.

So far, the spectral window observed in the SFG-experiments on the TiO_2 - D_2O -interface was limited to the range of about 2000 to 2600 cm^{-1} . The free OD-stretch vibration, however, is expected to lie at around 2700 cm^{-1} . Preliminary experiments at higher frequencies were inconclusive, and a more thorough study of this frequency range might provide insights into the presence of weakly- or non-hydrogen bonded OD-groups in the system. If so, further experiments using phase-resolved SFG might show if they belong to Ti-OD groups or to so far undiscovered interfacial water molecules.

For this work, only amorphous thin films of TiO_2 have been used. For future studies, it should be considered to anneal these samples in order to obtain thin films that have the rutile structure. These experiments might result in even more reproducible spectra and could be interesting to be compared to experiments on single crystalline rutile of various facets.

7.4 pD-Dependent Dynamics at the TiO_2 - D_2O -Interface

The second main part of this work is the investigation of the lifetime of vibrationally excited water molecules at the TiO_2 - D_2O -interface using time-resolved SFG. For this purpose D_2O solutions of pD 3, 7 and 11 were studied. Two pump-frequencies were used in order to excite the molecules in the system, namely 2550 and 2400 cm^{-1} . In most cases the typical reaction of interfacial water molecules to a pump-pulse could be observed in the SFG spectra: a drop in intensity due to spectral hole burning at the pump frequency, followed by the relaxation of the excited molecules and finished by the equilibration into a heated state of the probed water system, due to the high energy input. The time traces were analyzed using a four-level-model, that considers the excited molecules to relax (with time constant τ_1) to an intermediate state and from there (with

time constant τ_2) to a heated ground state.

For both pump-frequencies, the lifetime of the excited state for pD 7 and 11 was the same with about 360 *fs*. For pD 3 on the other hand, it was almost twice as long (about 660 *fs*), also for both pump-frequencies. This difference was attributed to the fact, that for pD values above the pcz (at pD 5) the overall hydrogen bonding network is generally stronger than for pD values below the pcz. This is a result of the strong hydrogen bonding interaction between the water molecules and the negatively charged semiconductor surface. So when studying different pD-values, even if subsets with the same hydrogen bonding strength are marked by the pump pulse, the surrounding water network might provide very different relaxation pathways for the excess energy. This might also explain the lower heat effect in the case of pD 3.

When looking at the time delay between the direct and the cross-peaks, so the peaks that are at another frequency range than the pump pulse and have not been pumped directly, major differences could be observed between results obtained for different pump frequencies. In the case of a pump-frequency of 2550 cm^{-1} (cross peak analysis by integrating at 2400 cm^{-1}), a finite time delay between the time traces could be observed (110 *fs* for pD 7 and 11, 230 *fs* for pD 3), meaning the coupling between the high- and the low-frequency modes takes longer, depending on the solution pD. This is a hint for a coupling mechanism including a down-hill energy transfer process, in which one oscillator directly gives its energy to the other. When comparing the time traces obtained by pumping at 2400 cm^{-1} (cross peak analysis by integrating at 2550 cm^{-1}) no such delay between the direct- and the cross-peak could be observed. This fact hints to a coupling mechanism, in which the vibration in one oscillator induces a frequency shift of the other vibration. Here no direct energy transfer occurs.

In addition to the normal SFG-signal, for pD 11 a signal was observed, which was attributed to excited-state absorption. At around 500 *fs* a small, narrow peak in the transient spectrum could be observed. This signal is the result of a molecule excited by the pump-pulse being involved in the SFG-process. Here the molecule starts and ends its SFG-contribution not from the ground but from the first excited state. Due to the anharmonicity of the oscillator involved, this signal appears at around 2530 cm^{-1} , so slightly lower than the peak frequency of the pump pulse. However, no time trace of this process could be analyzed, due to the fact that it is overwhelmed by the overall pump-probe-response of the water molecules.

Additional insight into the relaxation pathways could be gained by conducting pump-probe experiments using isotopically diluted solutions of pD 3, 7 and 11, in order to suppress inter- and intramolecular coupling in the water system. Here, a pump-frequency of 2550 cm^{-1} has been used. For all three pD-values, it could be shown that the lifetime of the HOD-molecules is significantly increased compared to that of the D₂O molecules in the isotopically undiluted case. For pD 3, this result is in good agreement with the isotope-dilution measurements using static SFG spectroscopy, where coupling between the low frequency and the central peak could be observed. However, in the case of pD 11 no such coupling was observed in static measurements. This indicates that the relatively short relaxation time for pure D₂O at pD 11 compared to the response of the isotopically diluted pD 11 solutions is the result of a so far not considered coupling mechanism. Since,

in contrast to the coupling effect observed for the undiluted pD 3 solution, at pD 11 the coupling does not appear in the static SFG-measurements, it is possible, that it is of unknown nature. One possible mechanism could be the coupling between the water molecules facing towards the semiconductor and Ti-OD groups, which results in the energy dissipation into the solid material.

In order to get deeper insights into the dynamics of water molecules at the $\text{TiO}_2\text{-D}_2\text{O}$ -interface, it could be useful to fill the gap between the pump frequencies of 2400 and 2550 cm^{-1} , in order to get a complete 2D-pump-probe SFG picture. This would not only increase the statistics of the resulting data set but also enable a more differentiated analysis of single subsets of water molecules. Also, the extension to lower pump-frequencies down to about 2100 cm^{-1} could be considered. In order to achieve this goal, different mixing crystals for the pump-pulse-path should be tested.

Though it was found in static SFG-experiments that the increase in ionic strength only has a small effect on the SFG signal of water at the TiO_2 -surface, it might be beneficial to investigate the influence of salts on the dynamics of the water molecules. It is possible that in this case the influence is not limited to the probing depth of the SFG-process but that the salt ions could also change the relaxation pathways by disturbing the hydrogen bonding network itself.

One open question is whether the probed excitation and relaxation of the water molecules partly includes a reorientation of the oscillators. One technique to address this question is polarisation-resolved SFG. In this work, the only polarisation combination used for all experiments was *ssp* (*s*-polarised SFG, *s*-polarised VIS and *p*-polarised IR), also including a *p*-polarised pump-pulse. By changing only the polarisation of the pump to *s*, information about the reorientation of the molecules can be obtained. By combining these results, with the results of other combinations like *pss* or *sps*, information about the molecular orientation might be obtained. Another technique to address this question is phase-resolved pump-probe SFG, which exists, but is very complicated to apply, especially to the sample system used in this work. However, it might provide deeper insights into the nature of the relaxation processes. When applying this technique to pump-probe SFG-experiments using a UV-pump pulse, it could even increase our understanding of the steps involved in the photocatalytic splitting of water.

List of Figures

1.1	Schematic unit cells of Rutile and Anatase	3
1.2	Long-range order projection of the structure of rutile and anatase	4
1.3	The (110) terminated plane of rutile.	4
1.4	Dissociation of water at rutile (110)	6
1.5	Photocatalytic Splitting of Water	8
1.6	The water molecule	9
1.7	Molecular orbital scheme of a hydrogen-bond	11
2.1	Scheme of an SFG-experiment and its energy diagram	14
2.2	Broadband IR and narrow band VIS in time and frequency	14
2.3	Components of s- and p-polarized light	18
2.4	Scheme of the Pump-Probe-SFG process	23
2.5	Scheme of the four level model of pump-probe measurements	23
2.6	Scheme of the Vivian-setup	25
3.1	Schematic picture of surfactant types and surfactants in water	28
3.2	Sketch of a typical surface tension vs. surfactant concentration plot	29
3.3	Structure of cetyltrimethylammonium bromide (CTAB)	30
3.4	Surface tension of the CTAB for various salt concentrations	30
3.5	Dynamic surface tension for various CTAB concentrations	32
3.6	Dynamic surface tension for various CTAB concentrations with 5.5 <i>m</i> NaCl	32
3.7	Dynamic surface tension for various salt concentrations with 0.3 <i>mmolal</i> CTAB	33
3.8	SFG-spectra of pure water and CTAB on the equilibrated water-air-interface	34
3.9	Pure CH-spectrum of 0.1 and 0.9 mm CTAB with and without NaCl	38
3.10	Kinetic SFG-spectra of CTAB at the water-air-interface	39
3.11	Kinetic development of amplitudes of CTAB at the water-air-interface	41
4.1	Schematic display of a sputter deposition process	44
4.2	Schematic principle of the magnetron sputtering technique	45
4.3	Fotos of two broken targets used for TiO ₂ sputtering deposition	46
4.4	Samples made using magnetron sputter deposition with particulate film	48
4.5	SFG spectra of the TiO ₂ -H ₂ O-interface obtained form the sputtered TiO ₂ samples	49
5.1	AFM-scans of a bare CaF ₂ substrate and a TiO ₂ coated sample	54
5.2	Sample cell and beam geometry	55

5.3	pD-dependent SFG-measurements of the $\text{TiO}_2\text{-D}_2\text{O}$ -interface and influence of VIS-angle	56
5.4	Isotopic dilution of D_2O at the $\text{TiO}_2\text{-D}_2\text{O}$ interface	59
5.5	Amplitudes and frequencies for each peak obtained from fitting the pD-dependent SFG-data	61
5.6	SFG-intensity depending on the solution pD	62
5.7	Influence of excess electrolyte on the $\text{TiO}_2\text{-D}_2\text{O}$ interface	63
5.8	Molecular picture of the water- TiO_2 -interface in dependence of the solution pD	65
6.1	Schematic display of spectral hole burning	68
6.2	Schematic display of a time trace obtained by pump-probe-SFG	69
6.3	Spectra taken at two different temperatures and their ratio	70
6.4	Ratio of pumped/unpumped SFG-spectra of water with pD 3, 7 and 11 for various time points, pumped at 2550 cm^{-1}	72
6.5	Time traces of pD 3, 7 and 11, pumped at 2550 cm^{-1}	74
6.6	Time traces for the cross-peaks at around 2400 cm^{-1} of the $\text{TiO}_2\text{-D}_2\text{O}$ -interface with pD 3, 7 and 11, pumped at 2550 cm^{-1}	76
6.7	Scheme of a six-level-relaxation pathway	79
6.8	Schematic display of vibrationally excited state SFG	79
6.9	Ratio of pumped/unpumped SFG-spectra with a pump frequency of 2400 cm^{-1}	81
6.10	Time traces of the $\text{TiO}_2\text{-D}_2\text{O}$ -interface at pD 3, 7 and 11 pumped at 2400 cm^{-1}	83
6.11	Pumped/unpumped spectra of isotopically diluted D_2O pumped at 2550 cm^{-1}	86
6.12	Time traces of isotopically diluted D_2O of pD 3, 7 and 11 pumped at 2550 cm^{-1}	87

List of Tables

3.1	Amplitudes of various CTAB solutions with and without salt	36
4.1	Results of the sputtering process on CaF_2	48
5.1	Fit parameters for isotopically diluted pD2 and pD11	60
6.1	Fit results of the direct and the cross peaks of time-resolved measurements at the TiO_2 - D_2O -interface for pD3, 7 and 11	77
6.2	Fit results of the direct and the cross peaks of time-resolved measurements at the TiO_2 - D_2O -interface for pD3, 7 and 11, pumped at 2400 cm^{-1} . . .	84
6.3	Fit results for pump-probe experiments with isotopically diluted solutions of pD 3, 7 and 11	88

Bibliography

- [1] A. Fujishima; K. Honda, Electrochemical Photolysis of Water at a Semiconductor Electrode, *Nature*, 238, 37, **1972**.
- [2] US Geological Survey, *Mineral Commodity Summaries, 2009*, Government Printing Office, **2009**.
- [3] E. Riedel, *Anorganische Chemie*, Walter de Gruyter, **2011**.
- [4] A.S. Yazdi; G. Guarda; N. Riteau; S.K. Drexler; A. Tardivel; I. Couillin; J. Tschopp, Nanoparticles Activate the NLR Pyrin Domain Containing 3 (Nlrp3) Inflammasome and Cause Pulmonary Inflammation through Release of IL-1 α and IL-1 β , *Proceedings of the National Academy of Sciences*, 201008155, **2010**.
- [5] U. Hålenius; F. Hatert; M. Pasero; S.J. Mills, IMA Commission on New Minerals, Nomenclature and Classification (CNMNC) Newsletter 35, *European Journal of Mineralogy*, 29 (1), 149, **2017**.
- [6] U. Diebold, The Surface Science of Titanium Dioxide, *Surf. Sci. Rep.*, 48 (5), 53, **2003**.
- [7] T. Radhakrishnan, The Optical Properties of Titanium Dioxide, *Proceedings of the Indian Academy of Sciences-Section A*, 35 (3), 117, **1952**.
- [8] M. Grätzel; F.P. Rotzinger, The Influence of the Crystal Lattice Structure on the Conduction Band Energy of Oxides of Titanium (IV), *Chemical Physics Letters*, 118 (5), 474, **1985**.
- [9] J.R. DeVore, Refractive Indices of Rutile and Sphalerite, *Journal of the Optical Society of America*, 41 (6), 416, **1951**.
- [10] O. Tonomura; T. Sekiguchi; N. Inada; T. Hamada; H. Miki; K. Torii, Band Engineering of Ru/Rutile-TiO₂/Ru Capacitors by Doping Cobalt to Suppress Leakage Current, *Journal of the Electrochemical Society*, 159 (1), G1, **2011**.
- [11] N. Wiberg; E. Wiberg; A.F. Holleman, *Lehrbuch der anorganischen Chemie, 102. Ed*, de Gruyter, Berlin, **2007**.
- [12] Z. Wu; W. Zhang; F. Xiong; Q. Yuan; Y. Jin; J. Yang; W. Huang, Active Hydrogen Species on TiO₂ for Photocatalytic H₂ Production, *Phys. Chem. Chem. Phys.*, 16 (15), 7051, **2014**.

- [13] U. Diebold, Perspective: A Controversial Benchmark System for Water-Oxide Interfaces: H₂O/TiO₂(110), *J. Chem. Phys.*, 147 (4), 040901, **2017**.
- [14] L.-F. Liao; C.-F. Lien; D.-L. Shieh; M.-T. Chen; J.-L. Lin, FTIR Study of Adsorption and Photoassisted Oxygen Isotopic Exchange of Carbon Monoxide, Carbon Dioxide, Carbonate, and Formate on TiO₂, *J. Phys. Chem. B*, 106 (43), 11240, **2002**.
- [15] C.M. Teh; A.R. Mohamed, Roles of Titanium Dioxide and Ion-Doped Titanium Dioxide on Photocatalytic Degradation of Organic Pollutants (Phenolic Compounds and Dyes) in Aqueous Solutions: A Review, *Journal of Alloys and Compounds*, 509 (5), 1648, **2011**.
- [16] T. Fujino; M. Katayama; K. Inudzuka; T. Okuno; K. Oura; T. Hirao, Surface Hydroxyl Formation on Vacuum-Annealed TiO₂ (110), *Applied Physics Letters*, 79 (17), 2716, **2001**.
- [17] S. Eriksen; P.D. Naylor; R.G. Egdell, The Adsorption of Water on SrTiO₃ and TiO₂: a Reappraisal, *Spectrochimica Acta Part A: Molecular Spectroscopy*, 43 (12), 1535, **1987**.
- [18] M.A. Henderson, Structural Sensitivity in the Dissociation of Water on TiO₂ Single-Crystal Surfaces, *Langmuir*, 12 (21), 5093, **1996**.
- [19] A.-a. Liu; S. Liu; R. Zhang; Z. Ren, Spectral Identification of Methanol on TiO₂(110) Surfaces with Sum Frequency Generation in the C–H Stretching Region, *J. Phys. Chem. C*, 119 (41), 23486, **2015**.
- [20] K. Sun; H.-Y. Su; W.-X. Li, Structures and Stability of Adsorbed Methanol on TiO₂(110) Surface Studied by Ab Initio Thermodynamics and Kinetic Monte Carlo Simulation, *Theoretical Chemistry Accounts*, 137 (10), **2018**.
- [21] E. Roman; F.J. Bustillo; J.L. de Segovia, Adsorption of Methanol on the Low Ti⁺³ Point Defects of the TiO₂ (001) Surface at 300 K, *Vacuum*, 41 (1-3), 40, **1990**.
- [22] K.S. Kim; M.A. Barteau, Reactions of Aliphatic Alcohols on the 011-Faceted TiO₂ (001) Surface, *Journal of Molecular Catalysis*, 63 (1), 103, **1990**.
- [23] S. Suzuki; Y. Yamaguchi; H. Onishi; T. Sasaki; K.-i. Fukui; Y. Iwasawa, Study of Pyridine and its Derivatives Adsorbed on a TiO₂ (110)-(1x1) Surface by Means of STM, TDS, XPS and MD Calculation in Relation to Surface Acid-Base Interaction, *Journal of the Chemical Society, Faraday Transactions*, 94 (1), 161, **1998**.
- [24] T. Preočanin; N. Kallay, Point of Zero Charge and Surface Charge Density of TiO₂ in Aqueous Electrolyte Solution as Obtained by Potentiometric Mass Titration, *Croatica Chemica Acta*, 79 (1), 95, **2006**.

- [25] P.A. Connor; K.D. Dobson; A. J. McQuillan, Infrared Spectroscopy of the TiO₂/Aqueous Solution Interface, *Langmuir*, 15 (7), 2402, **1999**.
- [26] M. Matsuoka; M. Kitano; M. Takeuchi; K. Tsujimaru; M. Anpo; J.M. Thomas, Photocatalysis for New Energy Production, *Catalysis Today*, 122 (1-2), 51, **2007**.
- [27] M.G. Walter; E.L. Warren; J.R. McKone; S.W. Boettcher; Q. Mi; E.A. Santori; N.S. Lewis, Solar Water Splitting Cells, *Chem. Rev.*, 110 (11), 6446, **2010**.
- [28] M. Pelaez; N.T. Nolan; S.C. Pillai; M.K. Seery; P. Falaras; A.G. Kontos; P.S.M. Dunlop; J.W.J. Hamilton; J.A. Byrne; K. O'Shea; M.H. Entezari; D.D. Dionysiou, A Review on the Visible Light Active Titanium Dioxide Photocatalysts for Environmental Applications, *Applied Catalysis B: Environmental*, 125, 331, **2012**.
- [29] A.J. Bard; M.A. Fox, Artificial Photosynthesis: Solar Splitting of Water to Hydrogen and Oxygen, *Accounts of Chemical Research*, 28 (3), 141, **1995**.
- [30] X. Li; J. Yu; M. Jaroniec, Hierarchical Photocatalysts, *Chemical Society Reviews*, 45 (9), 2603, **2016**.
- [31] Z. Wang; C. Li; K. Domen, Recent Developments in Heterogeneous Photocatalysts for Solar-Driven Overall Water Splitting, *Chemical Society Reviews*, **2018**.
- [32] T. Tachikawa; M. Fujitsuka; T. Majima, Mechanistic Insight into the TiO₂ Photocatalytic Reactions: Design of New Photocatalysts, *J. Phys. Chem. C*, 111 (14), 5259, **2007**.
- [33] W. Choi; A. Termin; M.R. Hoffmann, The Role of Metal Ion Dopants in Quantum-Sized TiO₂: Correlation between Photoreactivity and Charge Carrier Recombination Dynamics, *The Journal of Physical Chemistry*, 98 (51), 13669, **1994**.
- [34] A.L. Linsebigler; G. Lu; J.T. Yates Jr, Photocatalysis on TiO₂ Surfaces: Principles, Mechanisms, and Selected Results, *Chem. Rev.*, 95 (3), 735, **1995**.
- [35] M. Tanaka; G. Girard; R. Davis; A. Peuto; N. Bignell, Recommended Table for the Density of Water between 0 °C and 40 °C Based on Recent Experimental Reports, *Metrologia*, 38 (4), 301, **2001**.
- [36] M.L. Huggins, 50 Jahre Theorie der Wasserstoffbrückenbindung, *Angewandte Chemie*, 83 (5), 163, **1971**.
- [37] P.W. Atkins; J. De Paula, *Physikalische Chemie*, John Wiley & Sons, **2013**.
- [38] C.D. Bain, Sum-Frequency Vibrational Spectroscopy of the Solid/Liquid Interface, *Journal of the Chemical Society, Faraday Transactions*, 91 (9), 1281, **1995**.
- [39] A.G. Lambert; P.B. Davies; D.J. Neivandt, Implementing the Theory of Sum Frequency Generation Vibrational Spectroscopy: A Tutorial Review, *Applied Spectroscopy Reviews*, 40 (2), 103, **2005**.

- [40] M. Buck; M. Himmelhaus, Vibrational Spectroscopy of Interfaces by Infrared–Visible Sum Frequency Generation, *Journal of Vacuum Science & Technology A: Vacuum, Surfaces, and Films*, 19 (6), 2717, **2001**.
- [41] C. Hirose; N. Akamatsu; K. Domen, Formulas for the Analysis of the Surface SFG Spectrum and Transformation Coefficients of Cartesian SFG Tensor Components, *Applied Spectroscopy*, 46 (6), 1051, **1992**.
- [42] E.H.G. Backus; N. Garcia-Araez; M. Bonn; H.J. Bakker, On the Role of Fresnel Factors in Sum-Frequency Generation Spectroscopy of Metal–Water and Metal–Oxide–Water Interfaces, *J. Phys. Chem. C*, 116 (44), 23351, **2012**.
- [43] V. Ostroverkhov; G.A. Waychunas; Y.R. Shen, New Information on Water Interfacial Structure Revealed by Phase-Sensitive Surface Spectroscopy, *Physical Review Letters*, 94 (4), 046102, **2005**.
- [44] M. Bonn; H.J. Bakker; A. Ghosh; Ss Yamamoto; M. Sovago; R. Kramer Campen, Structural Inhomogeneity of Interfacial Water at Lipid Monolayers Revealed by Surface-Specific Vibrational Pump-Probe Spectroscopy, *J. Am. Chem. Soc.*, 132 (42), 14971, **2010**.
- [45] R.A. Livingstone; Y. Nagata; M. Bonn; E.H.G. Backus, Two Types of Water at the Water-Surfactant Interface Revealed by Time-Resolved Vibrational Spectroscopy, *J. Am. Chem. Soc.*, 137 (47), 14912, **2015**.
- [46] ST van der Post; HJ Bakker, The Combined Effect of Cations and Anions on the Dynamics of Water, *Phys. Chem. Chem. Phys.*, 14 (18), 6280, **2012**.
- [47] Y.L.A. Rezus; H.J. Bakker, On the Orientational Relaxation of HDO in Liquid Water, *J. Chem. Phys.*, 123 (11), 114502, **2005**.
- [48] M. Deiseroth; M. Bonn; E.H.G. Backus, Electrolytes Change the Interfacial Water Structure but Not the Vibrational Dynamics, *J. Phys. Chem. B*, 123 (40), 8610, **2019**.
- [49] I. Schlegel; P. Renz; J. Simon; I. Lieberwirth; S. Pektor; N. Bausbacher; M. Miederer; V. Mailänder; R. Muñoz Espí; D. Crespy, Highly Loaded Semipermeable Nanocapsules for Magnetic Resonance Imaging, *Macromolecular Bioscience*, 18 (4), 1700387, **2018**.
- [50] B. Fabry, *Tenside: Eigenschaften, Rohstoffe, Produktion, Anwendungen*, volume 25 of *Chemie in unserer Zeit*, VCH Verlagsgesellschaft mbH, **1991**.
- [51] M.J. Rosen; J.T. Kunjappu, *Surfactants and Interfacial Phenomena*, John Wiley & Sons, **2012**.

- [52] K. Beyer; D. Leine; A. Blume, The Demicellization of Alkyltrimethylammonium Bromides in 0.1 M Sodium Chloride Solution Studied by Isothermal Titration Calorimetry, *Colloids and Surfaces B: Biointerfaces*, 49 (1), 31, **2006**.
- [53] X. Y. Hua; M.J. Rosen, Calculation of the Coefficient in the Gibbs-Equation for the Adsorption of Ionic Surfactants from Aqueous Binary Mixtures with Nonionic Surfactants, *Journal of Colloid and Interface Science*, 87 (2), 469, **1982**.
- [54] M.J. Qazi; J.S. Schlegel; E.H.G. Backus; M. Bonn; D. Bonn; N. Shahidzadeh, Dynamic Surface Tension of Surfactants in the Presence of High Salt Concentrations, *Submitted*.
- [55] J.M. Pollard; A.J. Shi; K.E. Göklen, Solubility and Partitioning Behavior of Surfactants and Additives Used in Bioprocesses, *Journal of Chemical & Engineering Data*, 51 (1), 230, **2006**.
- [56] M.A. Bahri; M. Hoebeke; A. Grammenos; L. Delanaye; N. Vandewalle; A. Seret, Investigation of SDS, DTAB and CTAB Micelle Microviscosities by Electron Spin Resonance, *Colloids and Surfaces A: Physicochemical and Engineering Aspects*, 290 (1-3), 206, **2006**.
- [57] J.M. Neugebauer, *Detergents: An Overview*, volume 182, 239, Elsevier, **1990**.
- [58] A.M. Tedeschi; L. Franco; M. Ruzzi; L. Paduano; C. Corvaja; G. D'Errico, Micellar Aggregation of Alkyltrimethylammonium Bromide Surfactants Studied by Electron Paramagnetic Resonance of an Anionic Nitroxide, *Phys. Chem. Chem. Phys.*, 5 (19), 4204, **2003**.
- [59] P.K. Weissenborn; R.J. Pugh, Surface Tension of Aqueous Solutions of Electrolytes: Relationship with Ion Hydration, Oxygen Solubility, and Bubble Coalescence, *Journal of Colloid and Interface Science*, 184 (2), 550, **1996**.
- [60] M. Boström; D.R.M. Williams; B.W. Ninham, Ion Specificity of Micelles Explained by Ionic Dispersion Forces, *Langmuir*, 18 (16), 6010, **2002**.
- [61] J. Eastoe; J.S. Dalton, Dynamic Surface Tension and Adsorption Mechanisms of Surfactants at the Air–Water Interface, *Advances in Colloid and Interface Science*, 85 (2-3), 103, **2000**.
- [62] B. Noziere; C. Baduel; J.-L. Jaffrezo, The Dynamic Surface Tension of Atmospheric Aerosol Surfactants Reveals New Aspects of Cloud Activation, *Nature Communications*, 5, 3335, **2014**.
- [63] H. Yunfei; S. Yazhuo; L. Honglai; L. Dominique; S. Anniina, Surfactant Adsorption onto Interfaces: Measuring the Surface Excess in Time, *Langmuir*, 28 (6), 3146, **2012**.

- [64] E. Tyrode; M.W. Rutland; C.D. Bain, Adsorption of CTAB on Hydrophilic Silica Studied by Linear and Nonlinear Optical Spectroscopy, *J. Am. Chem. Soc.*, 130 (51), 17434, **2008**.
- [65] P.J. Kelly; R.D. Arnell, Magnetron Sputtering: a Review of Recent Developments and Applications, *Vacuum*, 56 (3), 159, **2000**.
- [66] D.L. Smith, *Thin-Film Deposition: Principles and Practice*, volume 108, McGraw-Hill Inc., New York, **1995**.
- [67] D. Depla; S. Mahieu, *Reactive Sputter Deposition*, Materials Science. Springer, **2008**.
- [68] S. Kadlec; J. Musil, Low Pressure Magnetron Sputtering and Selfsputtering Discharges, *Vacuum*, 47 (3), 307, **1996**.
- [69] J.L. Vossen, Control of Film Properties by RF-Sputtering Techniques, *Journal of Vacuum Science & Technology*, 8 (5), S12, **1971**.
- [70] A.N. Banerjee; C.K. Ghosh; K.K. Chattopadhyay; H. Minoura; A. K. Sarkar; A. Akiba; A. Kamiya; T. Endo, Low-Temperature Deposition of ZnO Thin Films on PET and Glass Substrates by DC-Sputtering Technique, *Thin Solid Films*, 496 (1), 112, **2006**.
- [71] H.R. Koenig; L.I. Maissel; Development, Application of RF Discharges to Sputtering, *IBM Journal of Research*, 14 (2), 168, **1970**.
- [72] J.A. Thornton, Magnetron Sputtering: Basic Physics and Application to Cylindrical Magnetrons, *Journal of Vacuum Science & Technology*, 15 (2), 171, **1978**.
- [73] C.H. Heo; S.-B. Lee; J.-H. Boo, Deposition of TiO₂ Thin Films using RF Magnetron Sputtering Method and Study of Their Surface Characteristics, *Thin Solid Films*, 475 (1-2), 183, **2005**.
- [74] W.D. Sproul; D.J. Christie; D.C. Carter, Control of Reactive Sputtering Processes, *Thin Solid Films*, 491 (1-2), 1, **2005**.
- [75] W. Demtröder, *Experimentalphysik 2*, Springer, **2017**.
- [76] S.J. Schlegel; S. Hosseinpour; M. Gebhard; A. Devi; M. Bonn; E.H.G. Backus, How Water Flips at Charged Titanium Dioxide: an SFG-Study on the Water-TiO₂ Interface, *Phys. Chem. Chem. Phys.*, 21 (17), 8956, **2019**.
- [77] K. Zhang; Q. Liu; H. Wang; R. Zhang; C. Wu; J.R. Gong, TiO₂ Single Crystal with Four-Truncated-Bipyramid Morphology as an Efficient Photocatalyst for Hydrogen Production, *Small*, 9 (14), 2452, **2013**.
- [78] M. Lazzeri; A. Vittadini; A. Selloni, Structure and Energetics of Stoichiometric TiO₂ Anatase Surfaces, *Phys. Rev. B*, 63 (15), **2001**.

- [79] X. Han; Q. Kuang; M. Jin; Z. Xie; L. Zheng, Synthesis of Titania Nanosheets with a High Percentage of Exposed (001) Facets and Related Photocatalytic Properties, *J. Am. Chem. Soc.*, 131 (9), 3152, **2009**.
- [80] I.N. Martyanov; S. Uma; S. Rodrigues; K.J. Klabunde, Structural Defects Cause TiO₂-Based Photocatalysts to be Active in Visible Light, *Chemical Communications*, (21), 2476, **2004**.
- [81] A. Arunachalam; S. Dhanapandian; C. Manoharan; G. Sivakumar, Physical Properties of Zn Doped TiO₂ Thin Films with Spray Pyrolysis Technique and its Effects in Antibacterial Activity, *Spectrochimica Acta Part A: Molecular and Biomolecular Spectroscopy*, 138, 105, **2015**.
- [82] P. Fenter; N.C. Sturchio, Mineral–Water Interfacial Structures Revealed by Synchrotron X-Ray Scattering, *Progress in Surface Science*, 77 (5-8), 171, **2004**.
- [83] M.K. Ridley; M.L. Machesky; D.A. Palmer; D.J. Wesolowski, Potentiometric Studies of the Rutile–Water Interface: Hydrogen-Electrode Concentration-Cell versus Glass-Electrode Titrations, *Colloids and Surfaces A: Physicochemical and Engineering Aspects*, 204 (1), 295, **2002**.
- [84] J. Cheng; M. Sprik, Acidity of the Aqueous Rutile TiO₂(110) Surface from Density Functional Theory Based Molecular Dynamics, *J. Chem. Theory Comput.*, 6 (3), 880, **2010**.
- [85] L.-M. Liu; C. Zhang; G. Thornton; A. Michaelides, Structure and Dynamics of Liquid Water on Rutile TiO₂(110), *Phys. Rev. B*, 82 (16), 161415(R), **2010**.
- [86] M. Sumita; C. Hu; Y. Tateyama, Interface Water on TiO₂ Anatase (101) and (001) Surfaces: First-Principles Study with TiO₂ Slabs Dipped in Bulk Water, *J. Phys. Chem. C*, 114 (43), 18529, **2010**.
- [87] Y.R. Shen, Surface Properties Probed by Second-Harmonic and Sum-Frequency Generation, *Nature*, 337 (6207), 519, **1989**.
- [88] S. Kataoka; M.C. Gurau; F. Albertorio; M.A. Holden; S.-M. Lim; R.D. Yang; P.S. Cremer, Investigation of Water Structure at the TiO₂/Aqueous Interface, *Langmuir*, 20 (5), 1662, **2004**.
- [89] S. Hosseinpour; F. Tang; F. Wang; R.A. Livingstone; S.J. Schlegel; T. Ohto; M. Bonn; Y. Nagata; E.H.G. Backus, Chemisorbed and Physisorbed Water at the TiO₂/Water Interface, *J. Phys. Chem. Lett.*, 8 (10), 2195, **2017**.
- [90] M. Gebhard; L. Mai; L. Banko; F. Mitschker; C. Hoppe; M. Jaritz; D. Kirchheim; C. Zekorn; T. de los Arcos; D. Grochla; R. Dahlmann; G. Grundmeier; P. Awakowicz; A. Ludwig; A. Devi, PEALD of SiO₂ and Al₂O₃ Thin Films on Polypropylene: Investigations of the Film Growth at the Interface, Stress, and Gas Barrier Properties of Dyads, *ACS Applied Materials Interfaces*, 10 (8), 7422, **2018**.

- [91] M. Gebhard; F. Mitschker; M. Wiesing; I. Giner; B. Torun; T. de los Arcos; P. Awakowicz; G. Grundmeier; A. Devi, An Efficient PE-ALD Process for TiO₂ Thin Films Employing a New Ti-Precursor, *Journal of Materials Chemistry C*, 4 (5), 1057, **2016**.
- [92] M. Bonn; Y. Nagata; E.H.G. Backus, Molecular Structure and Dynamics of Water at the Water-Air Interface Studied with Surface-Specific Vibrational Spectroscopy, *Angewandte Chemie International Edition*, 54 (19), 5560, **2015**.
- [93] D. Lis; E.H.G. Backus; J. Hunger; S.H. Parekh; M. Bonn, Liquid Flow Along a Solid Surface Reversibly Alters Interfacial Chemistry, *Science*, 344 (6188), 1138, **2014**.
- [94] L.M. Levering; M.R. Sierra-Hernandez; H.C. Allen, Observation of Hydronium Ions at the Air- Aqueous Acid Interface: Vibrational Spectroscopic Studies of Aqueous HCl, HBr, and HI, *J. Phys. Chem. C*, 111 (25), 8814, **2007**.
- [95] J. Schäfer; E.H.G. Backus; Y. Nagata; M. Bonn, Both Inter- and Intramolecular Coupling of O–H Groups Determine the Vibrational Response of the Water/Air Interface, *J. Phys. Chem. Lett.*, 4591, **2016**.
- [96] M. Sovago; R. Kramer Campen; G.W. Wurfel; M. Muller; H.J. Bakker; M. Bonn, Vibrational Response of Hydrogen-Bonded Interfacial Water is Dominated by Intramolecular Coupling, *Physical Review Letters*, 100 (17), 173901, **2008**.
- [97] J. Schäfer; G. Gonella; M. Bonn; E.H.G. Backus, Surface-Specific Vibrational Spectroscopy of the Water/Silica Interface: Screening and Interference, *Phys. Chem. Chem. Phys.*, 19 (25), 16875, **2017**.
- [98] G. Gonella; C. Lütgebaucks; A.G.F. De Beer; S. Roke, Second Harmonic and Sum-Frequency Generation from Aqueous Interfaces is Modulated by Interference, *J. Phys. Chem. C*, 120 (17), 9165, **2016**.
- [99] R. Khatib; E.H.G. Backus; M. Bonn; M.-J. Perez-Haro; M.-P. Gaigeot; M. Sulpizi, Water Orientation and Hydrogen-Bond Structure at the Fluorite/Water Interface, *Sci. Rep.*, 6, 24287, **2016**.
- [100] M. Hugenschmidt, *Lasermesstechnik: Diagnostik der Kurzzeitphysik*, Springer-Verlag, **2007**.
- [101] S.A. Bretschneider; I. Ivanov; H.I. Wang; K. Miyata; X. Zhu; M. Bonn, Quantifying Polaron Formation and Charge Carrier Cooling in Lead-Iodide Perovskites, *Advanced Materials*, 30 (29), 1707312, **2018**.
- [102] C. Ruckebusch; M. Sliwa; P. de Perrot; A. De Juan; R. Tauler, Comprehensive Data Analysis of Femtosecond Transient Absorption Spectra: A Review, *Journal of Photochemistry Photobiology C: Photochemistry Reviews*, 13 (1), 1, **2012**.

- [103] P. Hamm; M. Zanni, *Concepts and Methods of 2D Infrared Spectroscopy*, Cambridge University Press, **2011**.
- [104] J.D. Cyran; E.H.G. Backus; Y. Nagata; M. Bonn, Structure from Dynamics: Vibrational Dynamics of Interfacial Water as a Probe of Aqueous Heterogeneity, *J. Phys. Chem. B*, 122 (14), 3667, **2018**.
- [105] S. Woutersen; P. Hamm, Structure Determination of Trialanine in Water Using Polarization Sensitive Two-Dimensional Vibrational Spectroscopy, *J. Phys. Chem. B*, 104 (47), 11316, **2000**.
- [106] K. Ramasesha; L. De Marco; A. Mandal; A. Tokmakoff, Water Vibrations have Strongly Mixed Intra-and Intermolecular Character, *Nature Chemistry*, 5 (11), 935, **2013**.
- [107] J. Bredenbeck; A. Ghosh; H.-K. Nienhuys; M. Bonn, Interface-Specific Ultrafast Two-Dimensional Vibrational Spectroscopy, *Accounts of Chemical Research*, 42 (9), 1332, **2009**.
- [108] C.-S. Hsieh; M. Okuno; J. Hunger; E.H.G. Backus; Y. Nagata; M. Bonn, Aqueous Heterogeneity at the Air/Water Interface Revealed by 2D-HD-SFG Spectroscopy, *Angewandte Chemie International Edition*, 53 (31), 8146, **2014**.
- [109] V. V. Volkov; D.J. Palmer; R. Righini, Heterogeneity of Water at the Phospholipid Membrane Interface, *J. Phys. Chem. B*, 111 (6), 1377, **2007**.
- [110] L. Piatkowski; K.B. Eisenthal; H.J. Bakker, Ultrafast Intermolecular Energy Transfer in Heavy Water, *Phys. Chem. Chem. Phys.*, 11 (40), 9033, **2009**.
- [111] Q. Du; E. Freysz; Y.R. Shen, Vibrational Spectra of Water Molecules at Quartz/Water Interfaces, *Physical Review Letters*, 72 (2), 238, **1994**.
- [112] A. Eftekhari-Bafrooei; E. Borguet, Effect of Surface Charge on the Vibrational Dynamics of Interfacial Water, *J. Am. Chem. Soc. Comm.*, 131 (34), 12034, **2009**.
- [113] A. Tuladhar; S.M. Piontek; E. Borguet, Insights on Interfacial Structure, Dynamics, and Proton Transfer from Ultrafast Vibrational Sum Frequency Generation Spectroscopy of the Alumina (0001)/Water Interface, *J. Phys. Chem. C*, 121 (9), 5168, **2017**.
- [114] S.T. van der Post; C.S. Hsieh; M. Okuno; Y. Nagata; H.J. Bakker; M. Bonn; J. Hunger, Strong Frequency Dependence of Vibrational Relaxation in Bulk and Surface Water Reveals Sub-Picosecond Structural Heterogeneity, *Nature Communications*, 6, 8384, **2015**.
- [115] H.-K. Nienhuys; S. Woutersen; R.A. van Santen; H. Bakker, Mechanism for Vibrational Relaxation in Water Investigated by Femtosecond Infrared Spectroscopy, *J. Chem. Phys.*, 111 (4), 1494, **1999**.

Appendix

List of Publications

Publications Covered in this Thesis

- **S.J. Schlegel**; S. Hosseinpour; M. Gebhard; A. Devi; M. Bonn; E.H.G. Backus, How Water Flips at Charged Titanium Dioxide: an SFG-Study on the Water-TiO₂ Interface, *Phys. Chem. Chem. Phys.*, 21 (17), 8956, **2019**
- S. Hosseinpour; F. Tang; F. Wang; R.A. Livingstone; **S.J. Schlegel**; T. Ohto; M. Bonn; Y. Nagata; E.H.G. Backus, Chemisorbed and Physisorbed Water at the TiO₂/Water Interface, *J. Phys. Chem. Lett.*, 8 (10), 2195, **2017**
- M.J. Qazi; **J.S. Schlegel**; E.H.G. Backus; M. Bonn; D. Bonn; N. Shahidzadeh, Dynamic Surface Tension of Surfactants in the Presence of High Salt Concentrations, *Submitted*

Other Publications by the Same Author

- M.J. Qazi; R.W. Liefferink; **S.J. Schlegel**; E.H.G. Backus; D. Bonn; N. Shahidzadeh, Influence of Surfactants on Sodium Chloride Crystallization in Confinement, *Langmuir*, 33 (17), 4260, **2017**

Conference Contributions

- **S.J. Schmitt**; S. Hosseinpour; E.H.G. Backus, Investigating the Water-Titanium Dioxide Interface using SFG Spectroscopy, *Electro Chemical Surface Science*, Bad Honnef, Germany, **2015**
- **S.J. Schmitt**; S. Hosseinpour; E.H.G. Backus, Investigating the Water-Titanium Dioxide Interface using SFG Spectroscopy, *DPG Spring Meeting*, Berlin, Germany, **2015**
- **S.J. Schmitt**; S. Hosseinpour; E.H.G. Backus; M. Gebhard; A. Devi, Investigating the Water-Titanium Dioxide Interface using SFG Spectroscopy, *DPG Spring Meeting*, Regensburg, Germany, **2016**
- **S.J. Schmitt**; S. Hosseinpour; E.H.G. Backus, Investigating the Water-Titanium Dioxide Interface using SFG Spectroscopy, *Gordon Research Seminar*, Biddeford, USA, **2016**
- **S.J. Schlegel**; S. Hosseinpour; E.H.G. Backus, Investigating the Water-Titanium Dioxide Interface using SFG Spectroscopy, *25. Lecture Conference on Photochemistry*, Jena, Germany, **2016**
- **S.J. Schlegel**; S. Hosseinpour; E.H.G. Backus; M. Gebhard; A. Devi, Investigating the Water-Titanium Dioxide Interface using SFG Spectroscopy, *Bunsentagung*, Kaiserslautern, Germany, **2017**

Curriculum Vitae

Personal details:

Name **Simon Johannes Schlegel**,
birth name **Schmitt**

Address: Zaystraße 62
76437 Rastatt
Germany

Phone: 0049 176 57632988

E-Mail: simon-schlegel@web.de

Date of birth: 05.09.1987

Place of birth: Kirchheimbolanden, Germany

Gender: M

Nationality: German

Marital status: married

Education:

Since August 2014: PhD in the group of Prof. Dr. Mischa Bonn at
the Max Planck Institute for Polymer Research,
Mainz, Germany

June 2014: Diploma in chemistry (final mark 2.2),
Johannes-Gutenberg University, Mainz, Germany

November 2013 to June 2014: Diploma thesis in the group of Prof. Dr. Stephan Borrmann
at the Max Planck Institute for Chemistry,
Mainz, Germany

April 2007: High School Graduation (Abitur) at Gymnasium Weierhof,
Bolanden, Germany

International mobility:

March to June 2012: Semester abroad in the group of Prof. Dr. Miguel de la Guardia at the University of Valencia, Valencia, Spain

January to June 2005 (School) semester abroad at Rockway Mennonite Collegiate, Kitchener-Waterloo, Canada

Linguistic Skills: German (mother tongue), English (business fluent), Spanish (basic knowledge), French (school knowledge)

Acknowledgements

The acknowledgements are not included in this version.